

**DEVELOPMENT OF A VIBRATION ENERGY HARVESTING
SYSTEM WITH AMPLITUDE MAGNIFICATION FOR WIDE
FREQUENCY INPUT**

by

Pussewela Hewage Amindu Dharmasena

A Thesis Submitted in Partial Fulfillment of the Requirements for the Degree of
Master of Engineering in Mechatronics and Machine Intelligence

Examination Committee: Prof. Manukid Parnichkun (Chairperson)
Dr. Mongkol Ekpanyapong
Dr. Raffaele Ricco

Nationality: Sri Lankan

Previous Degree: Bachelor of Science of Engineering Honours in
Mechanical Engineering in Mechatronics
Engineering
Sri Lanka Institute of Information Technology
Malabe, Sri Lanka

Scholarship Donor: AIT Scholarships

Asian Institute of Technology
School of Engineering and Technology
Thailand
May 2024

AUTHOR'S DECLARATION

I, Pussewela Hewage Amindu Dharmasena, declare that the research work carried out for this thesis was in accordance with the regulations of the Asian Institute of Technology. The work presented in it are my own and has been generated by me as the result of my own original research, and if external sources were used, such sources have been cited. It is original and has not been submitted to any other institution to obtain another degree or qualification. This is a true copy of the thesis, including final revisions.

Date: 2024.05.07

Name (in printed letters): Pussewela Hewage Amindu Dharmasena

Signature:

A. Dharmasena

ACKNOWLEDGMENTS

I would like to express my gratefulness and appreciation to my advisor Prof. Manukid Parnichkun for the valuable guidance, ideas and support extended towards the successful completion of this thesis. It would have been difficult to complete this thesis without his advice.

It was a great pleasure to have Associate Prof. Mongkol Ekpanyapong and Assistant Prof. Raffaele Ricco as examination committee members for their insightful remarks and suggestions.

I would like to extend my thanks to Mr. Hoang Hung Manh for aiding and supporting me to conduct the laboratory work required for this thesis.

I would also like to thank AIT for providing me with the scholarship that enabled me to pursue my Master's degree.

Finally, I would like to thank my parents, family and friends for their unwavering support and encouragement to fulfill my educational goals. I'm eternally grateful for having the opportunity to meet these great people in my life.

ABSTRACT

In the quest of harnessing renewable energy to power up the world, focus has been put upon vibration energy. Few harvester types are already being tested in this area. One major aspect of vibration energy is the ability to supply power harnessed sustainably to low power electronic devices. The aim of this research is to design and develop a vibration energy harvester with free-impact motion type which has amplitude magnification to increase power generation and to make the harvester function efficiently for a wider frequency range. The relevant simulations were carried out by deriving the mathematical model. The required CAD modelling, PCB design and fabrication was done to make the physical prototype. The systems designed and developed in this thesis; both numerical model and physical model has managed to achieve the expected outcomes. The advantages of having a mechanical amplifier and the free-impact motion are shown by the magnitude gain the system has achieved and it works for the wide frequency range of 0.1 Hz – 5 Hz. The overall efficiency for the whole frequency range is hovering around 60% while the efficiency is hovering around 80% for low frequency, low amplitude input vibrations.

Keywords: Electromagnetic Energy Harvester, Vibration Energy Harvester, Free-Impact motion, Mechanical Amplifier

CONTENTS

	Page
AUTHOR'S DECLARATION	ii
ACKNOWLEDGMENTS	iii
ABSTRACT	iv
LIST OF TABLES	viii
LIST OF FIGURES	ix
LIST OF ABBREVIATIONS	xiii
CHAPTER 1 INTRODUCTION	1
1.1 Background of the Study	1
1.2 Statement of the Problem	2
1.3 Objectives of the Study	3
1.4 Scope and Limitations	3
1.5 Contribution	4
1.6 Organization of the Study	4
CHAPTER 2 LITERATURE REVIEW	5
2.1 Fundamentals of Vibration Energy Harvesters	5
2.2 Vibration Energy Harvesters	10
2.2.1 Piezoelectric Vibration Energy Harvester	10
2.2.2 Electromagnetic Vibration Energy Harvester	15
2.2.3 Electrostatic Vibration Energy Harvester	23
2.2.4 Triboelectric Vibration Energy Harvester	25
2.2.5 Comparison of Transduction Mechanisms of VEHs	26
2.3 Amplification Methods	27
2.3.1 Mechanical Amplifier	28
2.3.2 Frequency Up	30
2.3.3 Resonant Tuning	30
2.3.4 Hybrid Systems	33
2.3.5 Free Impact Motion	34
2.3.6 Comparison of Amplification Methods	37
2.4 Magnetic Field Enhancement	38
2.4.1 Magnet Configuration	38

2.4.2 Magnetic Field Enhancement using Spacers	40
2.5 Power Management System	41
2.5.1 Conversion Circuits	41
2.5.2 Storage Types	42
2.6 Efficiency	44
CHAPTER 3 METHODOLOGY	47
3.1 Overview	47
3.2 Simulation Related Design	49
3.2.1 Equations	49
3.2.2 Input Vibration Platform	52
3.2.3 Mechanical Amplifier	52
3.2.4 Electromagnetic Harvester	53
3.2.5 Power Collector	53
3.3 CAD Model	55
3.3.1 Input Vibration Platform	55
3.3.2 Mechanical Amplifier	56
3.3.3 Energy Harvester	58
3.3.4 Final Assembly	61
3.4 Circuit Board	62
3.5 Fabrication	64
3.5.1 Input Vibration System	64
3.5.2 Mechanical Amplifier	65
3.5.3 Energy Harvester	65
3.5.4 Full Fabrication	67
3.5.5 Electrical System	69
CHAPTER 4 RESULTS	71
4.1 Simulation Results	71
4.1.1 Effect of Mechanical Amplifier on Input	71
4.1.2 Generated Voltage on Simulation	74
4.1.3 Generated Power on Simulation	76
4.1.4 Effect of Magnetic Moment on Output Power	79
4.1.5 Effect of Coil Length on Output Power	80
4.2 Experimental Results	81
4.2.1 Generated Voltage during Experimentation	81

4.2.2	Generated Power during Experimentation	84
4.3	Comparison between Simulation and Experimental Results	87
4.3.1	Comparison According to Amplitude	87
4.3.2	Comparison According to Frequency	89
CHAPTER 5	CONCLUSION	91
5.1	Conclusion	91
5.2	Recommendations	91
REFERENCES		93
APPENDIX: INPUT GAIN OF SIMULATION		97

LIST OF TABLES

Tables	Page
Table 2.1 Acceleration Levels and Peak Forces from Everyday Applications	9
Table 3.1 Mechanical System Parameters	70
Table 3.2 Electrical Circuit and Magnetic Parameters	70
Table 4.1 Magnification Gain Breakdown of the Mechanical Amplifier	72
Table 4.2 Simulated Voltage Gain Breakdown Based on Amplitude and Frequency	76
Table 4.3 Power Amplification Breakdown Based on Amplitude and Frequency	77
Table 4.4 Experimental Voltage Gain Breakdown Based on Amplitude and Frequency	84
Table 4.5 Experimental Power Gain Breakdown Based on Amplitude and Frequency	85

LIST OF FIGURES

Figures	Page
Figure 2.1 Single DOF VEH with Base Excitation	5
Figure 2.2 Schematic Diagram of a Piezoelectric Transducer	10
Figure 2.3 (a) Cantilever-based (b) Membrane-based Geometries	12
Figure 2.4 Fabricated Hybrid System	13
Figure 2.5 (a) Conceptual Design (b) Top View of the Hybrid System	13
Figure 2.6 Schematic of the System with Magnetic Pendulum	14
Figure 2.7 (a) Schematic Diagram (b) Tested System	15
Figure 2.8 Single DOF Electromagnetic Vibration Energy Harvester	16
Figure 2.9 Model of the Prototype	19
Figure 2.10 Schematic of Micro-Electromagnetic Generator	20
Figure 2.11 Two Different Sizes of the Prototypes (a) D9L12 with 300 Coil Turns and (b) D7L12 with 200 Coil Turns	20
Figure 2.12 Energy Harvester Developed	21
Figure 2.13 (a) Cut-view and (b) Schematic of the prototype	22
Figure 2.14 Prototype with Mechanical Amplifier	23
Figure 2.15 Electrostatic VEH (Parallel Plate Capacitor Model)	23
Figure 2.16 General Schematics of an Electrostatic VEH	24
Figure 2.17 Schematic View of a Triboelectric VEH	25
Figure 2.18 Structure of the First Triboelectric Generator	25
Figure 2.19 Different Mechanical Amplification Methods with Mechanical Gain	28
Figure 2.20 (a) Implemented System (b) Schematic View of the System	29
Figure 2.21 Schematic of Piezoelectric Windmill	29
Figure 2.22 Dual Resonating Electromagnetic Generator	30
Figure 2.23 Multimodal Array Structure	31
Figure 2.24 Design of a Compressive Axial Loader	32
Figure 2.25 Cantilever Beam with Magnetic Resonance Tuning	33
Figure 2.26 (a) Final Prototype Design (b) R-P Mechanism (c) L-GE Mechanism	34

Figure 2.27	(a) Conventional Electromagnetic VEH and (b) Free Impact Motion Electromagnetic VEH	35
Figure 2.28	Relative Displacement for Different Modes of Motion	36
Figure 2.29	Output Voltage for Different Modes of Motion	36
Figure 2.30	(a) Standard Halbach Array and (b) Normal Magnet Configuration	38
Figure 2.31	(a) Structure of and (b) Cross Section view of Triangular Halbach Array, (c) Structure of Double Halbach Array	39
Figure 2.32	(a) Harvester Architecture and (b) Magnetic Flux Derivative for Different Stacks	40
Figure 2.33	Bridge Rectifier (a) During Positive Half-cycle, (b) During Negative Half-cycle and (c) Output Waveform	41
Figure 2.34	(a) Battery Variations, (b) Flywheel, (c) Supercapacitors and (d) Capacitors	43
Figure 3.1	Overall Functionality Diagram	48
Figure 3.2	Schematic Diagram	48
Figure 3.3	Overall System Designed using MATLAB Simulink	51
Figure 3.4	Modelled Input Vibration Platform	52
Figure 3.5	Modelled Mechanical Amplifier	52
Figure 3.6	Modelled Electromagnetic Harvester	53
Figure 3.7	Signal Conversion Block	54
Figure 3.8	Modelled Full-Wave Bridge Rectifier	54
Figure 3.9	Modelled Power Collector Section	55
Figure 3.10	(a) Top view (b) Side view of the Modelled Vibration Input System	56
Figure 3.11	Mechanical Amplifier with Slider-Crank Mechanism	57
Figure 3.12	Mechanical Amplifier with Scotch-Yoke Mechanism	57
Figure 3.13	Versions of Moving Mass Holder	58
Figure 3.14	Versions of End Holders	59
Figure 3.15	(a) Steel Rod (3 mm diameter, 70 mm length) (b) End Base Holder	60
Figure 3.16	Final Energy Harvester System	60
Figure 3.17	Final CAD of the Prototype	61

Figure 3.18	Schematic Diagram of the Circuit	62
Figure 3.19	Designed PCB	63
Figure 3.20	Electrical Wiring of the Control System	63
Figure 3.21	Final Assembled Vibration System	64
Figure 3.22	Final Assembled Mechanical Amplifier	65
Figure 3.23	Energy Harvester with Assembled Moving Mass	65
Figure 3.24	Energy Harvester with Coil Windings	66
Figure 3.25	Final Assembled Energy Harvester	66
Figure 3.26	Cutting the Base using Acrylic Sheet	67
Figure 3.27	(a) Fabricated Parts, Height Alignment between (b) Mechanical Amplifier and Energy Harvester, (c) Input Vibration System and Mechanical Amplifier	67
Figure 3.28	Test Fitting Components Together	68
Figure 3.29	Final Fabricated System	68
Figure 3.30	Electrical Circuit during Fabrication	69
Figure 3.31	Fabricated Electrical Circuit	69
Figure 4.1	Mechanical Amplifier Simulation	71
Figure 4.2	Polar Representation of the Magnification Effect	72
Figure 4.3	Input Gain vs Frequency Plot	73
Figure 4.4	Generated Voltage (Top) with Amplification, and (Bottom) without Amplification	74
Figure 4.5	Voltage Magnitude Gain for Different Amplitude Ranges	75
Figure 4.6	Generated Power during Simulations	77
Figure 4.7	Power Amplification Breakdown for Amplitude Ranges	78
Figure 4.8	Power Generation with Varying Magnetic Moment	79
Figure 4.9	Power Generation with Varying Coil Length	80
Figure 4.10	(Left) During Testing and (Right) Link Connecting the Scotch-Yoke Mechanism to Amplifier being Snapped	81
Figure 4.11	Generated Voltage during Experimentation	82
Figure 4.12	Voltage Amplification Breakdown for Amplitude Ranges	83
Figure 4.13	Generated Power during Experimentation	85
Figure 4.14	Power Amplification Breakdown for Amplitude Ranges	86

Figure 4.15	(Top) Average Power, and (Bottom) Average Voltage Efficiencies with Respect to Amplitude	87
Figure 4.16	Amplitude wise Efficiency Breakdown	88
Figure 4.17	(Top) Average Power, and (Bottom) Average Voltage efficiencies with Respect to Frequency	89
Figure 4.18	Frequency wise Efficiency Breakdown	90

LIST OF ABBREVIATIONS

VEH	= Vibration Energy Harvester
DOF	= Degree Of Freedom
MEMS	= Micro Electro Mechanical Systems
MMR	= Mechanical Motion Rectifier
kmph	= kilometer per hour
NdFeB	= Neodymium Iron Boron
AC	= Alternating Current
DC	= Direct Current
PLA	= Polylactic Acid
WA	= With Amplifier
WOA	= Without Amplifier

CHAPTER 1

INTRODUCTION

1.1 Background of the Study

In recent years, there has been growing interest in finding alternative sources of energy to address the ever-increasing global energy demand and reduce our reliance on conventional power generation methods. One promising avenue is vibration energy harvesting, a technique that involves converting mechanical vibrations into usable electrical energy. This technology has gained significant attention due to its potential to harness energy from ambient vibrations present in various environments and power small-scale electronic devices, thereby offering a sustainable and environmentally friendly power solution.

Vibrations are ever-present in our daily lives, whether they are produced by vehicles on the road, machinery in industrial settings, or even the natural motion of the human body. Vibration energy harvesting aims to capture this untapped energy and convert it to electricity using different mechanisms and transduction principles. The principle behind vibration energy harvesting lies in the concept of resonance, where energy is efficiently transferred from the source of vibration to the energy harvesting system.

The design of a vibration energy harvesting system typically involves three essential components: a transducer, an energy storage element, and power management circuitry. The transducer is the heart of the system and plays a crucial role in converting mechanical vibrations into electrical energy. Various transduction mechanisms are used such as, piezoelectric, electromagnetic, electrostatic, and triboelectric, each with its own advantages and limitations. The widely used transducer are piezoelectric, which generates electric charges when subjected to mechanical stress.

The energy storage element, often a rechargeable battery or a supercapacitor, serves as a buffer to store the harvested energy for later use. This component ensures that the energy harvested from vibrations is efficiently stored and readily available to power electronic devices when needed. The power management circuitry, on the other hand,

regulates the energy flow, optimizing the energy transfer from the transducer to the storage element. It ensures that the harvested energy is appropriately conditioned, transformed, and stored, while maximizing the overall system efficiency.

One of the significant advantages of vibration energy harvesting is its ability to provide a sustainable power source for low-power electronic devices or sensors that are often found in remote or inaccessible locations. These devices, commonly referred to as wireless sensor nodes, are used in various applications, including structural health monitoring, environmental sensing, and even wearable electronics. By utilizing vibration energy harvesting, these devices can operate autonomously, eliminating the need for battery replacement or connection to the electrical grid.

Moreover, vibration energy harvesting offers the potential for energy self-sufficiency in certain scenarios. For instance, wireless sensors deployed in industrial environments can harvest energy from the surrounding machinery, allowing them to continuously monitor the condition of equipment and detect faults without requiring frequent maintenance or manual intervention. In transportation systems, vibration energy harvesting can be employed to power embedded sensors in roads or bridges, facilitating real-time monitoring and ensuring infrastructure safety.

1.2 Statement of the Problem

However, despite its promise, vibration energy harvesting still faces several challenges. One of the primary challenges lies in the wide variation in vibration sources, frequencies, and amplitudes encountered in different environments. Designing energy harvesting systems that can efficiently capture and convert energy from these diverse vibrations is a complex task. Furthermore, the power output of vibration energy harvesters is typically low, limiting their applicability to low-power devices.

The efficiency of vibration energy harvesting systems can be affected by various factors, including mismatch between the vibration source frequency and the resonant frequency of the energy harvester. For optimal energy conversion, the harvester should be tuned to resonate at the frequency of the vibration source. However, in real world

scenarios, the frequency of ambient vibrations can vary widely, leading to a mismatch and reduced energy conversion efficiency.

Another tricky aspect is the design and implementation of vibration energy harvesting systems which can be complex and require careful consideration of various factors. Selection of appropriate transduction mechanisms, materials, and structural configurations is crucial for achieving efficient energy conversion. Moreover, the integration of the energy harvesting system with the target device or system often requires custom engineering and design considerations, adding to the overall complexity and cost. These design challenges seriously hinder the scalability and practicability of vibration energy harvesting, especially for widespread and large-scale applications.

1.3 Objectives of the Study

This research is focused on designing and developing a free-impact motion type vibration energy harvesting system by amplitude magnification to increase the power output for wider operating frequency.

1. Develop a free-impact motion type vibration energy harvesting system by amplitude magnification.
2. Derive and simulate the mathematical model of the mechanism.
3. Design, fabricate and test the energy harvesting system.
4. Using an appropriate mechanism to improve the efficiency and power output of the system.

1.4 Scope and Limitations

The scope and limitations of this research are as follows.

1. The research will mainly focus on oscillatory motion.
2. This research is focused on amplitude magnification and utilizing free impact motion.
3. The system will be tested for input amplitudes from 0.1 cm up to 4 cm and frequency from 0 Hz up to 5 Hz.

4. The volume of the prototype will be less than 500 cm^3 (length x width x height will be approximately 10cm x 10cm x 5 cm).
5. The efficiency of the system will be greater than 40%.

1.5 Contribution

This research aims to incorporate the advantages of using mechanical amplifiers and free impact motion to enhance the output power density of Electromagnetic VEHs by increasing the input amplitude and harvestable frequency range which will make electromagnetic VEHs a viable option when it comes to microscale energy harvesters.

1.6 Organization of the Study

The remainder of this thesis is organized as follows. Chapter two provides details about the literature review conducted to collection information from previously conducted researchers for this topic. Chapter three shows the methodology, estimated budget and timeline for this thesis.

CHAPTER 2

LITERATURE REVIEW

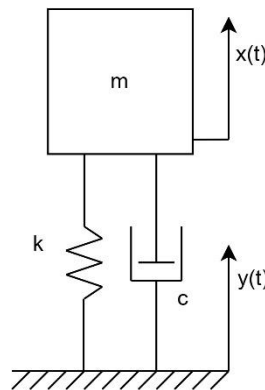
When considering Vibration Energy Harvesters (VEHs), they can be differentiated according to the transducer mechanism used, amplification techniques utilized, resonance tuning techniques implemented, the degrees of freedom (DOF) impacted and so on. This chapter will provide a brief introduction about the fundamental basics that should be considered in Vibration Energy Harvesters, about the different types of VEH and their advantages and disadvantages, different amplification techniques and their unique features. Then the focus will be shifted into Electromagnetic VEH and the impact of their magnetic configuration and methods followed to enhance the magnetic field. Finally, the power management systems that are incorporated with VEH will be discussed.

2.1 Fundamentals of Vibration Energy Harvesters

Vibration energy harvesting is based on relative displacement between two masses. In the case of VEH, as mentioned in (Hendijanizadeh et al., 2013; Yildirim et al., 2017), it is based on the relative displacement between a mass and a base excitation. A simple single DOF VEH system is shown in Figure 2.1.

Figure 2.1

Single DOF VEH with Base Excitation



From this Figure 2.1, the obtained equation of motion is:

$$m\ddot{z} + c\dot{z} + kz = -m\ddot{y} \quad (1)$$

Where,

m : Mass of the system

$z = x - y$: The relative displacement between the mass and the base

$c = c_e + c_m$: The damping coefficient with both electrical and mechanical contributions

k : Device stiffness

Equation (1) can be rewritten after dividing by mass as:

$$z + 2\zeta\omega_n z + \omega_n^2 z = -y \quad (2)$$

Where,

$$\zeta = \frac{c}{2\sqrt{mk}} \quad : \text{The total damping ratio}$$

$$\omega_n = \sqrt{\frac{k}{m}} \text{ (rad s}^{-1}\text{)} \quad : \text{The natural frequency}$$

The system transfer function (H(s)) can be obtained by taking the Laplace transform of Equation (2).

$$H(s) = \frac{Z(s)}{Y(s)} = - \frac{s^2}{s^2 + 2\zeta\omega_n s + \omega_n^2} \quad (3)$$

The response of this system for an oscillatory motion which can be mathematically depicted by a sinusoidal wave can be modelled by supplying $y(t) = Y\cos(\omega t)$. In this substitution, Y = amplitude of the system and ω = the frequency of the vibration.

Equation (1) can be rewritten as:

$$\ddot{z} + 2\zeta\omega_n(\dot{z}) + \omega_n^2(z) = \omega^2 Y \cos(\omega t) \quad (4)$$

Equation (4) can be rewritten by substituting $s = j\omega$ as:

$$H(j\omega) = \frac{Z(j\omega)}{Y} = \frac{\omega^2}{\omega_n^2 - \omega^2 + j2\zeta\omega_n\omega} \quad (5)$$

The modulus or magnitude of Equation (5) is:

$$|Z(j\omega)| = \frac{Y\omega^2}{\sqrt{(\omega_n^2 - \omega^2)^2 + (2\zeta\omega_n\omega)^2}} \quad (6)$$

The phase angle of the frequency response of Equation (5) is:

$$\phi = \tan^{-1}\left(\frac{2\zeta\omega_n\omega}{\omega^2 - \omega_n^2}\right) \quad (7)$$

The steady state solution of this system is:

$$z(t) = \frac{Y\omega^2}{\sqrt{(\omega_n^2 - \omega^2)^2 + (2\zeta\omega_n\omega)^2}} \cos(\omega t - \phi) \quad (8)$$

The power that can be harvested from this type of vibratory system is proportional to the force (F) and velocity (V). This can be depicted as:

$$P = \int_0^v F dv \quad (9)$$

Equation (9) should be equal to the product of damping force from Equation (1) and the velocity of the mass (\dot{Z}). This can be shown as:

$$|\dot{Z}| = \frac{Y\omega^3}{\sqrt{(\omega_n^2 - \omega^2)^2 + (2\zeta\omega_n\omega)^2}} \quad (10)$$

The product of damping force of the system and the velocity of the mass (Equation (10)) is shown as:

$$P = \int_0^{\dot{z}} c_e \dot{z} d\dot{z} = \frac{c_e |\dot{z}|^2}{2} \quad (11)$$

The average power that can be generated by a VEH in a dimensionless form can be obtained by substituting Equation (10) to Equation (11) and can be depicted as:

$$P_{dim} = P_{out} = \frac{m\omega^3 Y^2 \zeta_e \left(\frac{\omega}{\omega_n}\right)^3}{\left(1 - \left(\frac{\omega}{\omega_n}\right)^2\right)^2 + \left(\frac{2\zeta\omega}{\omega_n}\right)^2} \quad (12)$$

By observing the Equation (12), it can be noted that power can be increased significantly with the frequency of vibration and the amplitude of the vibration. A low damping factor (ζ) can be achieved by increasing the mass as large as possible within the available volume of the energy harvester. This will reduce the second part of the denominator and increase the numerator in Equation (12) thus increasing the power generated.

If the device can be designed in a way that its' resonant frequency matches the excitation frequency ($\frac{\omega}{\omega_n} = 1$), this will reduce the denominator of Equation (12) more significantly than the previously mentioned method thus increasing the generated power. How these designs and amplifying are done will be mentioned in the coming sections of this chapter.

Vibration Energy Harvesters are gaining a renowned attention is due to the untapped potential that is available in this sector. Oscillations that occur from everyday machines in offices and industries like Air Conditioners, Hydraulic and Pneumatic presses, Photocopy machines, Printers, everyday home appliances like fans, doors, blenders, grinders, in bridges, in railroads, in ocean waves, human motions like jogging, walking are few examples of vibration sources that can be considered for energy production. Table 2.1 shows some accelerations and peak forces from everyday applications.

Table 2.1

Acceleration Levels and Peak Forces from Everyday Applications (Cleante et al., 2019; Dong et al., 2019; Hendijanizadeh et al., 2013; Yildirim et al., 2017)

Vibration Source	Acceleration (m/s²)	Frequency (Hz)
Internal Combustion Engine	12	200
Base of three-axis machine tool	10	70
Blender casing	6.4	121
Clothes dryer	3.5	121
Vehicle instrument panel section in vehicle dashboard panels	3	13
Door frame just after door closes	3	125
Heating, Ventilation and Air Condition (HVAC) vents in office buildings	0.2-1.5	60
Window panels next to busy roads	0.7	100
Compact Disc drivers on computers and laptops	0.6	75
Second story floor of buildings	0.2	100
Vibrations on railroads by trains	Varies widely	0.03-50 (varies based on type of track, ballasts, train type)
Ocean waves	Varies widely	0.03-0.3

As stated in Table 2.1, there is a huge array of vibration sources waiting to be harnessed.

2.2 Vibration Energy Harvesters

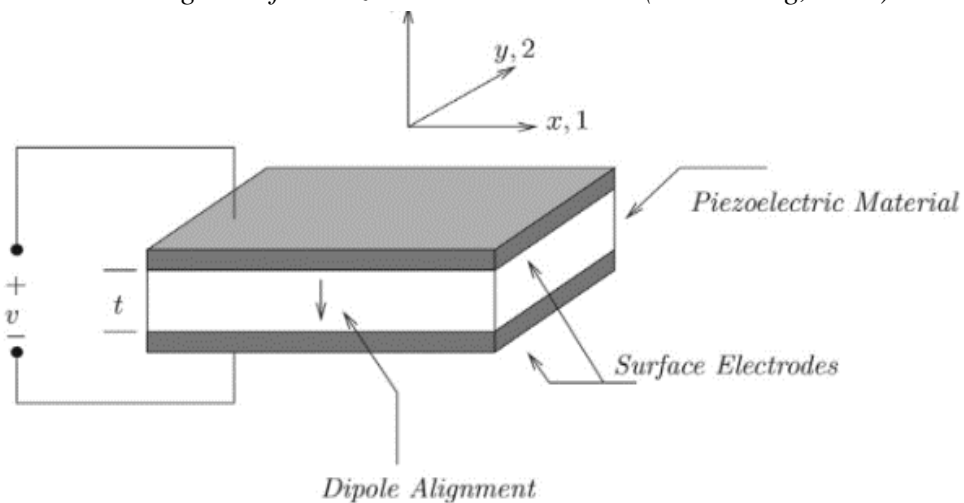
Vibration Energy Harvesters (VEHs) are mainly categorized according to their respective transduction mechanism.

2.2.1 Piezoelectric Vibration Energy Harvester

This is the most commonly available type of vibration energy harvesting mechanism due to the simple structure of this type of generator. Piezoelectric transducers have the ability to directly convert mechanical strain into electrical charge. This characteristic is called as ‘direct piezoelectric effect’. This effect is used in sensing applications. The reverse piezoelectric effect is when the material converts applied electric field into mechanical stresses. This is used for actuation purposes (Dong et al., 2019). A schematic diagram of a piezoelectric transducer is shown in Figure 2.2.

Figure 2.2

Schematic Diagram of a Piezoelectric Transducer (Wei & Jing, 2017)



The piezoelectric effects can be described in numerical form as follows.

$$\delta = \frac{\sigma}{Y} + dE \quad (13)$$

$$D = \varepsilon E + d\sigma \quad (14)$$

Where,

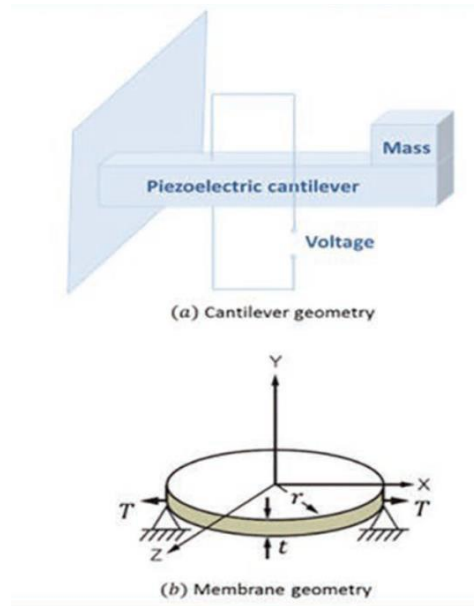
δ	: Mechanical strain
σ	: Mechanical stress
Y	: Young's Modulus
d	: Piezoelectric strain coefficient
E	: Electric field
D	: Electrical displacement (charge density)
ε	: Dielectric constant

From observing the Equations (13) and (14), it is obvious that the energy conversion of piezoelectric materials depends on external vibrations and forces.

The most common design geometry for piezoelectric VEH is based on cantilever design. It is due to the ability of cantilever beams to produce highest average strain for an applied force. A major drawback in cantilever-based designs is that they only work in a single direction (Dong et al., 2019). In other words, they are 1 DOF systems. Figure 2.3 depicts few common geometry shapes used in piezoelectric VEHs. Few researches have been already done to overcome this issue. (Fan et al., 2018; Hou et al., 2021; Iqbal & Khan, 2018) have introduced hybrid systems by incorporating piezoelectric VEH with electromagnetic VEH to improve power output while (Cho et al., 2016; He et al., 2017; Hou et al., 2021) utilize motion of other systems like pendulums to harness vibrations from multiple directions thus giving the vibration energy harvester multiple DOFs.

Figure 2.3

(a) Cantilever-based (b) Membrane-based Geometries (Dong et al., 2019)

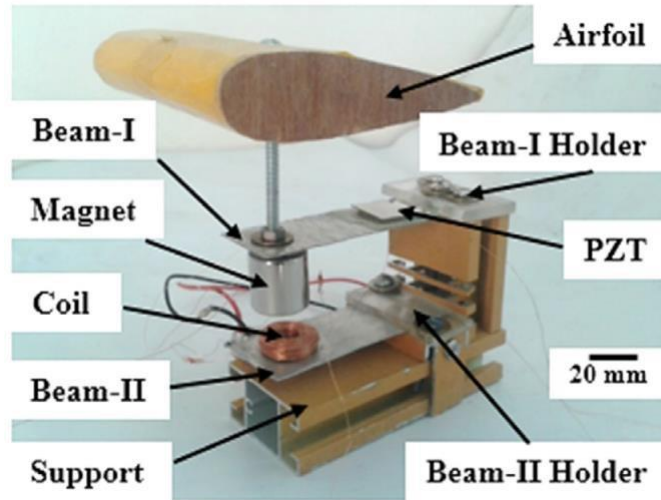


(Iqbal & Khan, 2018) have implemented a hybrid design which comprises of electromagnetic and piezoelectric components which is used to harvest ambient wind and vibrations in bridges caused by wind and other motions. The system composes of a permanent magnet and a wound coil for the electromagnetic VEH part and a piezoelectric plate, an airfoil and two cantilever beams for the piezoelectric VEH part. Figure 2.4 shows the system that was implemented. This hybrid implementation has improved the energy produced by the system considerably and widened the bandwidth range.

The system proposed by (Fan et al., 2018) is a bi-directional hybrid energy harvester made from two piezoelectric cantilever beams, a suspended magnet and a set of coils. They have managed to expand the power outputs at ultra-low frequencies (less than 10 Hz) and have increased the working frequency bandwidth as well. System implemented by (Fan et al., 2018) is shown by Figure 2.5.

Figure 2.4

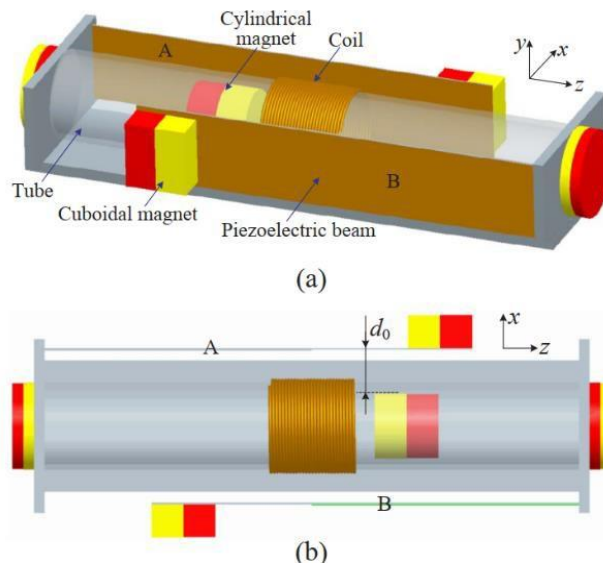
Fabricated Hybrid System (Iqbal & Khan, 2018)



The system designed by (Cho et al., 2016) utilizes a pendulum movement to increase the power harnessed by the system. This system was designed to be integrated in trains and has the ability to harness vibration energy from 2 DOFs. This harvests two types of inertial energy: from the tangential and centripetal accelerations respectively. The

Figure 2.5

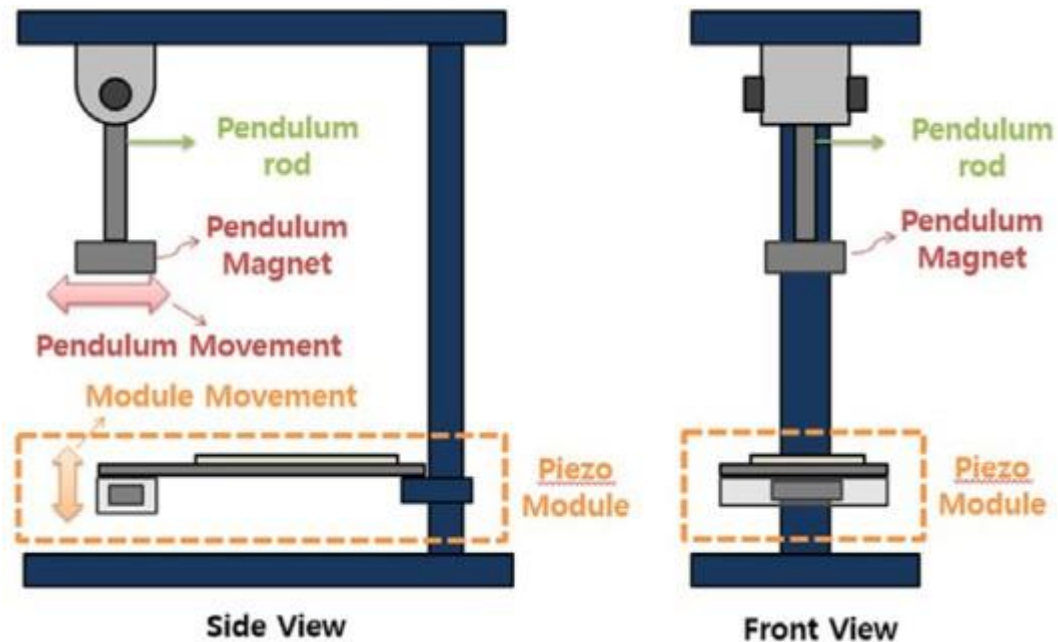
(a) Conceptual Design (b) Top View of the Hybrid System (K. Fan et al., 2018)



system is shown by Figure 2.6. This system is designed to work between 3Hz – 6Hz frequencies and have obtained a maximum average power density of 40.24 $\mu\text{W}/\text{cm}^3$. They have emphasized the ability to self-power the safety sensors of the train by using multiple modules of the proposed energy harvester.

Figure 2.6

Schematic of the System with Magnetic Pendulum (Cho et al., 2016)

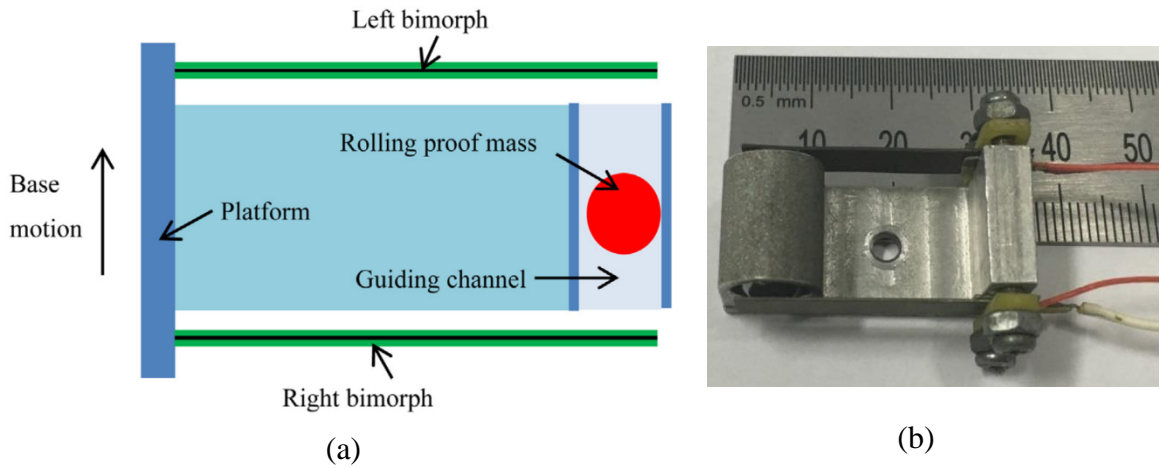


The system which is proposed by (He et al., 2017) presents an Impact based piezoelectric VEH. These are very good at harnessing the most of ambient low-level, low frequency vibrations in a wide bandwidth. Figure 2.7 shows the schematic and the test prototype of the system. The major difference in this design is that the mass is not fixed unlike other cantilever-based designs. The mass can freely roll in the guiding channel. As this mass collides with one end of cantilevered biomorphs, it bounces back and the cantilevered beam vibrations significantly than conventional cantilevered beams. This drastically improves the energy produced and this is an essential feature when it comes to low-level, low-frequency ambient vibrations. Slightly varied designs with usage of a sliding proof mass instead of a rolling mass have been already tested and even though the harvested energy is high, it's not good as using a rolling mass. This

is because rolling friction is less than sliding friction, which results in less kinetic energy being wasted via friction. The guide channel length used for testing is 15mm and the maximum power output of one biomorph is 511 μW at 18.4 Hz when the system is subjected to an acceleration of the amplitude 1g (9.8 m/s^2).

Figure 2.7

(a) Schematic Diagram (b) Tested System (He et al., 2017)



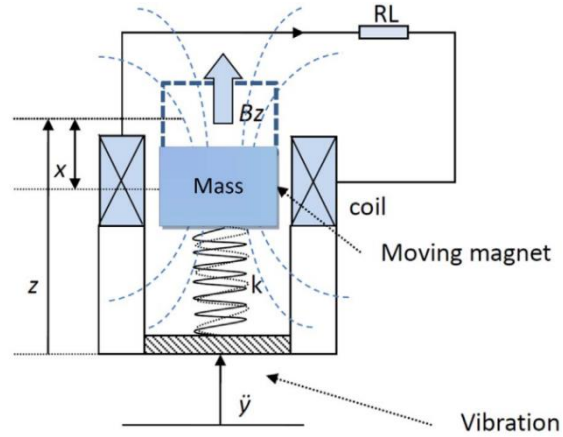
2.2.2 Electromagnetic Vibration Energy Harvester

Electromagnetic VEHS are designed based on the Faradays' Law of electromagnetic induction (Dong et al., 2019). The working principle can be simply mentioned as follows. The motion of a magnetic field relative to a conductive coil result in a current flow being induced in the coil. Figure 2.8 depicts a simple single DOF Electromagnetic VEHS. The vibrations exerted by the environment on the magnet (mass) causes the magnet to undergo a relative translational displacement with respect to the coil. This relative displacement causes a magnetic flux difference in the coil. This induces a voltage in the coil and it can be determined using Equation (15).

$$\varepsilon_v = -\frac{d\Phi_B}{dt} \quad (15)$$

Figure 2.8

Single DOF Electromagnetic Vibration Energy Harvester (Dong et al., 2019)



Where,

ε_v : Induced Voltage

Φ_B : Magnetic flux

As the magnet is allowed to move perpendicular to the coil in this 1DOF VEH, the maximum open circuit voltage across the coil is given by Equation (16)

$$V_{oc} = NBl \frac{dx}{dt} \quad (16)$$

Where,

N : Number of turns in the coil

B : Magnetic induction

l : length of a winding

x : relative distance between the magnet and the coil

By observing Equation (16) it is clear that the voltage amplitude is proportional to the speed of the moving mass (magnet) relative to the coil. Neglecting the gravitational force and the internal resistance of circuitry, the dynamics and mechanical-electrical energy conversion of the moving mass equations are depicted by Equation (17) and Equation (18).

$$m\ddot{z} + d\dot{z} + kz = -\alpha V_L - m\ddot{y} \quad (17)$$

$$\dot{V}_L + \omega_c V_L = \delta_c \omega_c \dot{z} \quad (18)$$

Where,

$$\alpha = \frac{B_z l}{R_L} \quad : \text{Electrical coupling force factor}$$

$$V_L \quad : \text{Resultant voltage across the resistive load}$$

$$d \quad : \text{Mechanical damping}$$

$$\delta_c = B_z l \quad : \text{Electromechanical Conversion factor}$$

$$\omega_c = \frac{R_L}{L_e} \quad : \text{Cutoff frequency of the equivalent high pass circuit of the converter}$$

$$L_e = \frac{\mu_0 N^2 \pi R^2}{h_b} \quad : \text{Coiling self-inductance}$$

The displacement of the mass and output voltage is obtained by implementing Laplace transformation for Equations (17) and (18).

$$Z(s) = \frac{-mY \cdot (s + \omega_c)}{ms^3 + (m\omega_c + d)s^2 + (k + \alpha\delta_c + d_2\omega_c)s + k\omega_c} \quad (19)$$

$$V(s) = \frac{-mY \cdot \delta_c \omega_c s}{ms^3 + (m\omega_c + d)s^2 + (k + \alpha\delta_c + d\omega_c)s + k\omega_c} \quad (20)$$

Equations and shows the transfer functions between displacement, voltage and input acceleration.

$$H_{ZY}(s) = \frac{Z(s)}{Y(s)} \quad (21)$$

$$H_{VY}(s) = \frac{V(s)}{Y(s)} \quad (22)$$

The power (P_e) dissipated by the load (R_L) in the frequency domain for a harmonic input $\ddot{y} = Y_0 e^{j\omega t}$ can be written by using Laplace variable $s = j\omega$ to Equation (22).

$$\begin{aligned} P_e(\omega) &= \frac{|V(j\omega)|^2}{2R_L} = \frac{|H_{VY}(j\omega)|^2 |Y(j\omega)|^2}{2R_L} \quad (23) \\ &= \frac{Y_0^2}{2R_L} \left| \frac{m\delta_c \omega_c j\omega}{(\omega_c + j\omega)(-m\omega^2 + j\omega d + k) + \alpha\delta_c \omega_c j\omega} \right|^2 \end{aligned}$$

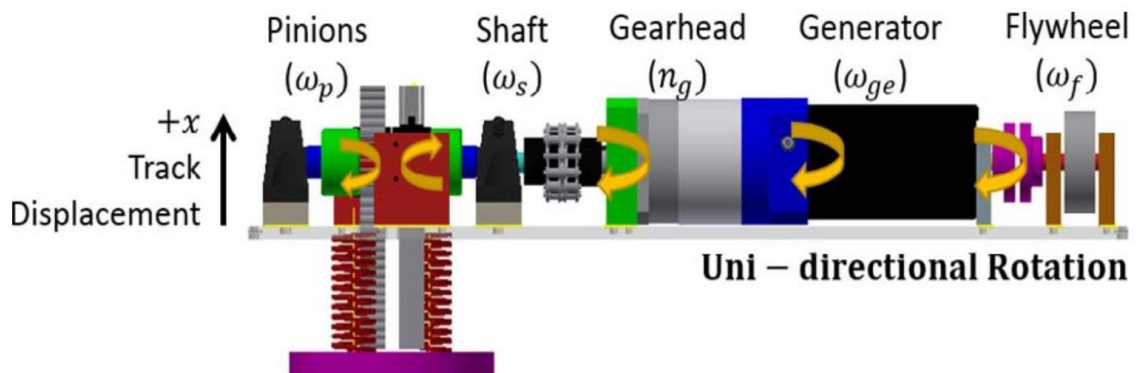
By considering the Equation (23) it can be observed that the power can be increased by either increasing the input amplitude or resonant frequency. This theory has been utilized for most of single DOF electromagnetic VEHs that are designed (Haroun et al., 2015a, 2015b; Lin, Pan, et al., 2018; Lin, Wang, et al., 2018; Shahosseini & Najafi, 2014; Shen & Lu, 2020; H. Wang et al., 2018; Z. Wang et al., 2021).

(Lin, Pan, et al., 2018) have proposed a design which is used to harness railroad vibration energy. The authors claim that the design mentioned in this paper is easy to install and increases the power capacity. The ease of installation is achieved by including a spring preload and reset mechanism which eliminates the need of anchoring the device to the railroad foundation. This drastically reduces the installation time (can be installed within 30 minutes) and this device can be easily incorporated to railroads without compromising the structural integrity of the railroad structures. Figure 2.9 shows the design of the prototype. A major section of this device is the Mechanical Motion Rectifier (MMR) mechanism. This MMR converts the vertical vibratory motion

(up and down) of the railroad into unidirectional rotational motion which is fed into gearhead and generator. This is ensured by two racks positioned in opposite direction, two pinions and one-way clutches. The flywheel is used as the storage element and the generator works with the stored momentum after it gets disengaged from the input due to lack of input acceleration. This ensures the device keeps producing energy for a considerable time even after the input is removed (train has passed the location) from the system. The tests conducted using this device has managed a 7W (average) 56W (peak) power generation from a deflection of 5.7mm for a freight train moving at 64 kmph. It is mentioned in this paper that the typical amplitude of railroad track vibration is between 1mm – 12mm and the frequency is between 1 Hz and 4 Hz.

Figure 2.9

Model of the Prototype (Lin, Pan, et al., 2018)



Two research papers published by the same group of authors in 2015 (Haroun et al., 2015b, 2015a) and (Shen & Lu, 2020) have tested a novel Electromagnetic VEH based on free/impact motion. This approach provides a non-resonant behavior where the output power is increased continuously with either input frequency or amplitude, with both. This free impact motion results in four different response types for the input amplitude and frequency ranges. These amplification mechanisms will be discussed later in this chapter.

In (Haroun et al., 2015a). the team has utilized this free impact motion to develop a micro-electromagnetic VEH. Two different experiments are conducted to check the

impact of different magnet shapes and different magnet sizes in energy harvesting. Figure 2.10 shows the design. Few prototypes with different sizes have been fabricated in this experiment. The stroke length is kept at 8mm and the prototype diameter is kept at 9mm. the length is different depending on the magnet type utilized (12 mm and 16 mm). Figure 2.11 depicts the size of the fabricated prototypes. The volume of these two

Figure 2.10

Schematic of Micro-Electromagnetic Generator (Haroun et al., 2015a)

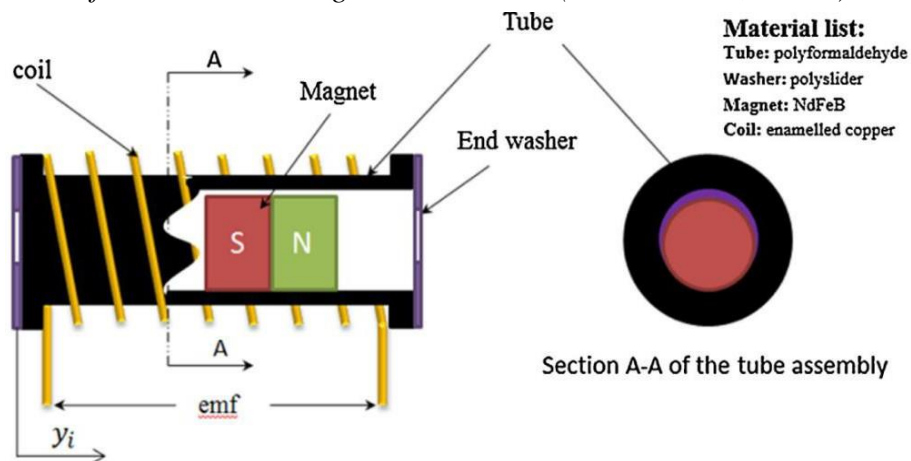
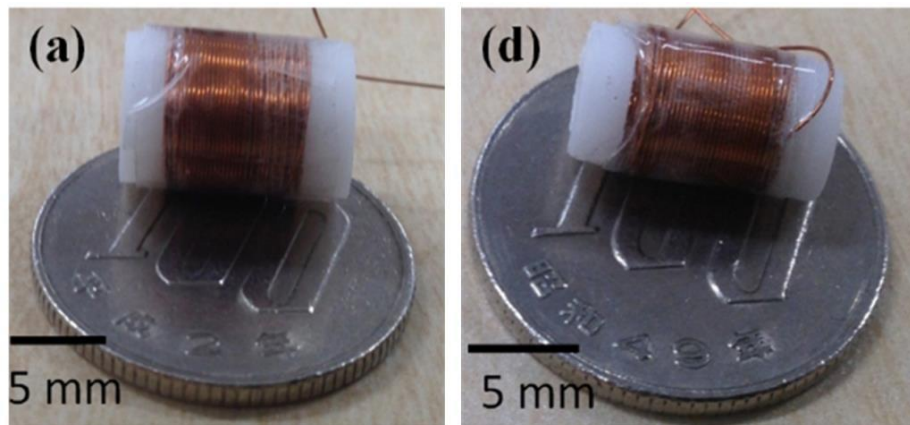


Figure 2.11

Two Different Sizes of the Prototypes (a) D9L12 with 300 Coil Turns and (b) D7L12 with 200 Coil Turns (Haroun et al., 2015a)

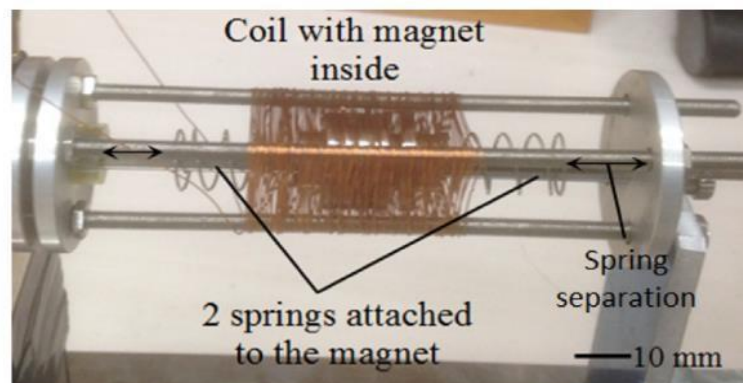


prototypes are 0.461 cm^3 and 0.763 cm^3 and they are tested at 2.5 Hz and 3.33 Hz over an amplitude range from 10mm to 40 mm. At 2.5 Hz input frequency and 9.87 ms^{-2} average acceleration, D7L12 and D9L12 generates $42.2 \mu\text{W}$ and $91.3 \mu\text{W}$ respectively. At 3.33 Hz input frequency and 9.29 ms^{-2} average acceleration, D7L12 produces $65.2 \mu\text{W}$ while D9L12 produces $81.9 \mu\text{W}$. The authors claim that the increase in power density of these prototypes is due to the utilization of free impact motion.

Another design which implements free impact motion is presented by (Haroun et al., 2015b). This prototypes' length is 100 mm, the coil length is 40 mm and the stroke length is 26 mm. The tests were done for an input amplitude of 1 mm (0.01 m) and a frequency ranging from 3 Hz to 21 Hz. The results depict that free impact design has a resonant frequency less than that of conventional electromagnetic harvesters due to the mass spring separation. This results in a higher power output at low frequencies and the power output is magnified 5 times at 14 Hz and 10 times at 10 Hz.

Figure 2.12

Energy Harvester Developed (Haroun et al., 2015b)

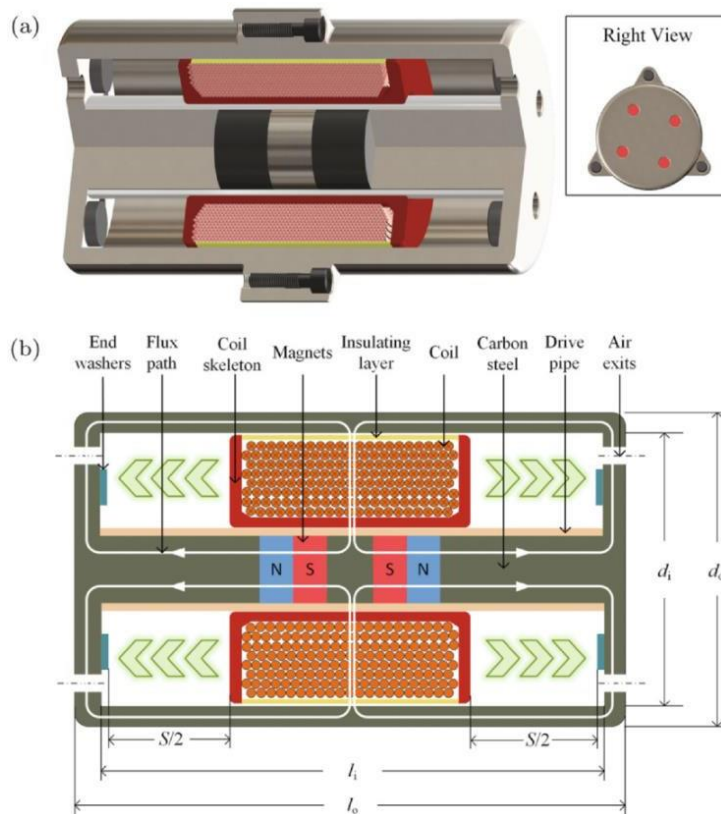


In design proposed by (Shen & Lu, 2020), apart from utilizing free impact motion, enhancement of the magnetic flux is also considered. This enhancement is done by using a steel frame which not only enhances the magnetic flux, but also protects the harvester from external magnetic interferences. The coil length utilized is 22 mm. The cylindrical frame has an outer diameter of 28 mm, an outer length of 51mm. The

material of the magnet is similar to the type used by above mentioned experiments; Neodymium (NdFeB) magnets. The magnets have a diameter of 10 mm and a thickness of 6 mm. The prototype is tested for the input frequencies 1.5 Hz – 7 Hz and amplitude range of 10 mm – 40 mm. The test results shows that the prototype has a power density of $748 \mu\text{W}/\text{cm}^3$ at an input frequency of 4.5 Hz and a 40 mm vibration amplitude which is higher than conventional electromagnetic energy harvesters.

Figure 2.13

(a) Cut-view and (b) Schematic of the Prototype (Shen & Lu, 2020)

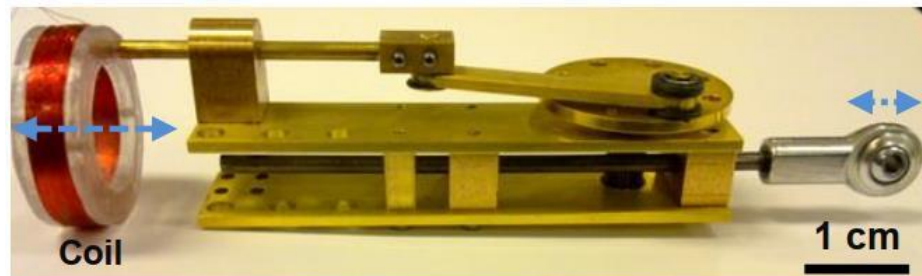


The electromagnetic VEH proposed by (Shahosseini & Najafi, 2014) consists of a mechanical amplifier. The prototype is shown by Figure 2.14. The input amplitude is mechanically amplified with the help of a rack and pinion which amplifies the input and is incorporated with a slider-crank mechanism which uses the amplified input to move the coil around the magnet. The prototype weighs 130 grams and has a volume

of 40 cm^3 . The input amplitude is amplified by 4 times which results in an output power amplification by 16 times. The power density of this device is $170 \mu\text{W}/\text{cm}^3$.

Figure 2.14

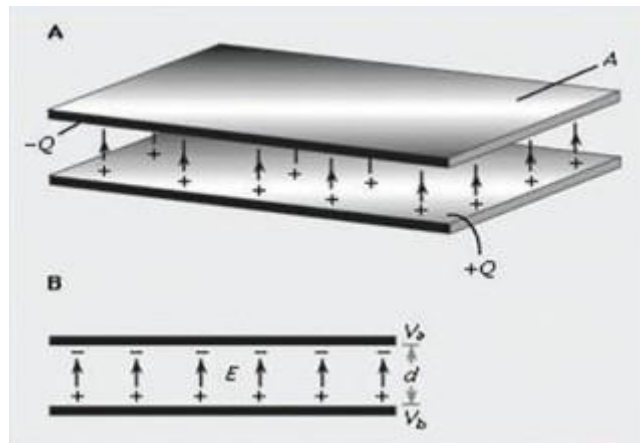
Prototype with Mechanical Amplifier (Shahosseini & Najafi, 2014)



2.2.3 Electrostatic Vibration Energy Harvester

Figure 2.15

Electrostatic VEH (Parallel Plate Capacitor Model) (Dong et al., 2019)



Electrostatic VEHs are designed based on the Coulomb's Law. These types of harvesters work by changing the capacitance between the two parallel plates. There are two configurations used in electrostatic VEHs; constant voltage and constant charge configurations. In constant voltage, the charge is increased while in constant charge mode, the voltage is changed (Dong et al., 2019; Wei & Jing, 2017). Figure 2.15 shows a general view of an electrostatic vibration energy harvester.

Figure 2.16

General Schematics of an Electrostatic VEH (Dong et al., 2019)

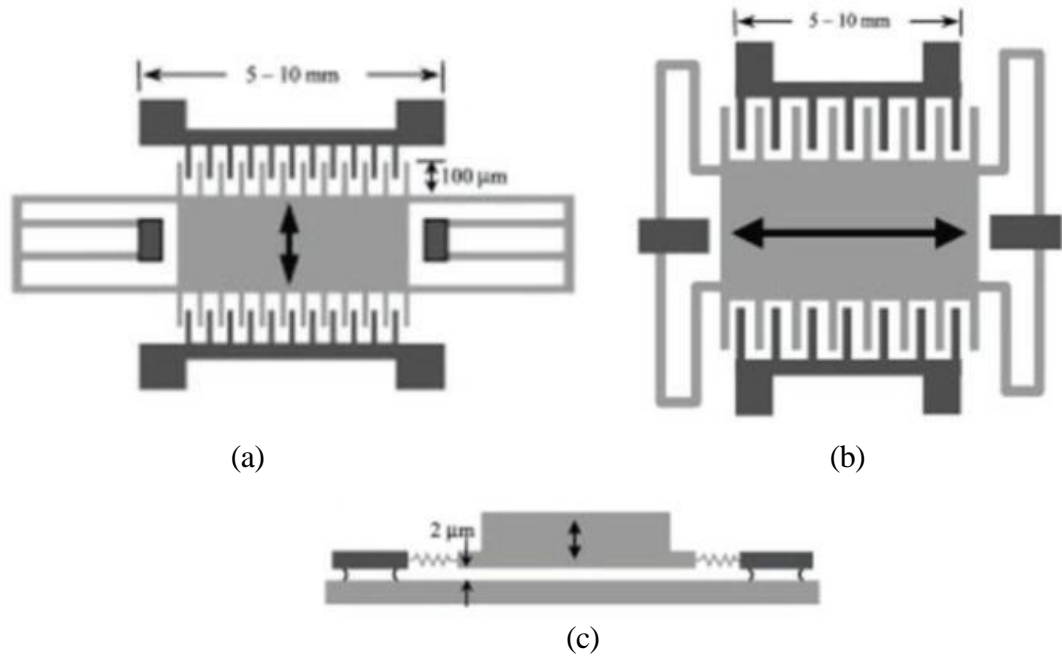
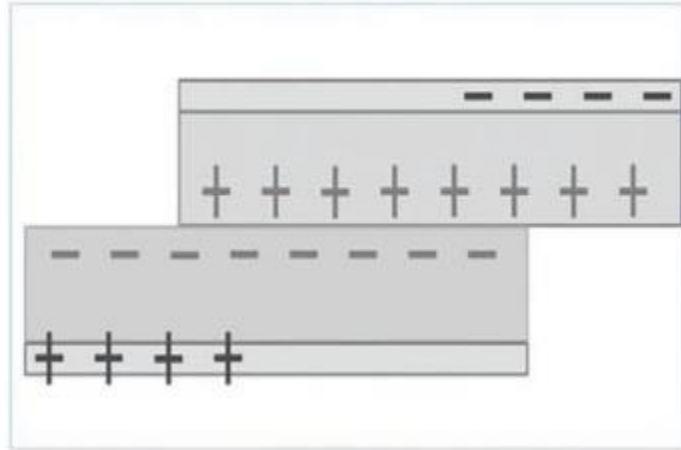


Figure 2.16 represents three most common designs used for electrostatic VEHs namely, In-plane overlap design, In-plane gap closing and Out-of-plane gap closing (Dong et al., 2019; Wei & Jing, 2017). When the system is vibrated, due to the overlaps in the teeth of the comb drive, a capacitance change occurs and this is utilized in In-plane overlap design (Figure 2.16 a). These devices are extremely vulnerable to damages because the comb devices can rotate and tilt due to vibrations. therefore, mechanical stops are used to prevent contact with each other. Functionality of In-plane gap closing design (Figure 2.16 b) is similar to In-plane overlap, but the direction of translation is perpendicular. The gap change between the comb drive teeth causes the change in capacitance. The same issues and prevention methods are applicable for In-plane gap closing design also, albeit the issues are not to the same extent as in In-plane overlap. Out-of-plane gap closing design (Figure 2.16 c) provides the largest possible maximum capacitance, but few issues like adhesion of the two plates due to surface interaction, damping and stiction hinders the power potential. Introducing a vacuum between to the system significantly increases the power generation capacity.

2.2.4 Triboelectric Vibration Energy Harvester

Figure 2.17

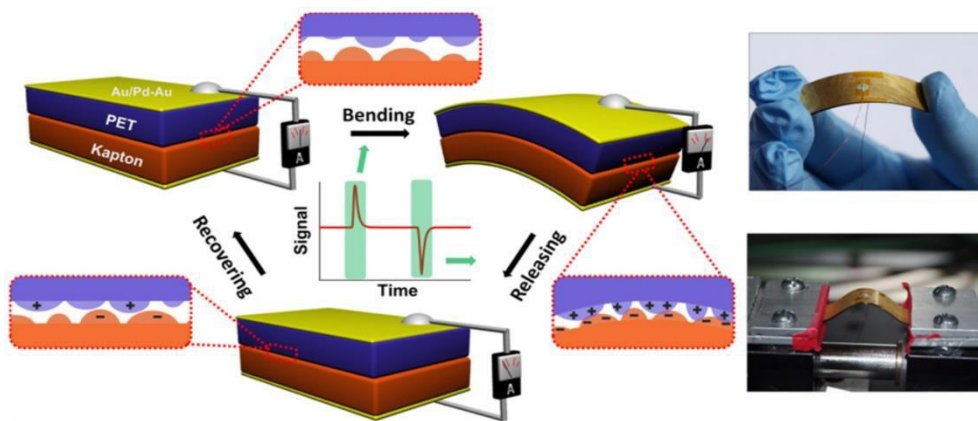
Schematic View of a Triboelectric VEH (Dong et al., 2019)



Triboelectric VEHS are designed on the theory of electrical charge migration between two materials. When two materials are in contact with each other, charges like electrons, ions, molecules transfer among the two materials to balance their relevant electrochemical potential. When two materials are parting ways increasing the distance amongst them, some atoms send extra electrons and some atoms keep them. This creates an electrical potential difference and the triboelectric charges on the material

Figure 2.18

Structure of the First Triboelectric Generator (F. R. Fan et al., 2012)



surfaces initiates a flow of current of electrons to balance the existing electrical potential difference. This is a relatively new design concept when compared with other VEH designs and tends to have a high energy conversion efficiency and are typically used in biomechanical applications (Dong et al., 2019; F. R. Fan et al., 2012).

2.2.5 Comparison of Transduction Mechanisms of VEHs

The four types of transduction mechanisms can be compared with the help of papers of (Dong et al., 2019; Wei & Jing, 2017). When it comes to ease of conversion of vibration energy to electrical energy, Piezoelectric VEHs stand out because of its simple structure and its ability to directly convert vibration energy into electrical energy. Due to the simple structure, these type of VEHs are compatible with MEMS although piezoelectric coupling gets reduced considerably when piezoelectric films are integrated in standard MEMS fabrication. This is a major limiting factor which affects the overall performance of small scale piezoelectric VEHs. The efficiency of the system depends on the material properties and the output impedance of Piezoelectric VEHs are typically higher ($> 100 \text{ k}\Omega$) which results in a low output current. But this issue is negated because the system has the ability to produce high output voltages.

Piezoelectric VEHs doesn't require an external voltage source to conduct its energy conversion process and tend to have a theoretically higher power density ($300 \mu\text{W}/\text{cm}^3$ – $400 \mu\text{W}/\text{cm}^3$) even though charge leakage is possible (Dong et al., 2019).

When Electromagnetic VEHs are considered, a major disadvantage is it being unfavorable for micro scale because the reduction of interaction between the magnet and the coils due to smaller magnet size, number of coil turns and small stroke length results in limiting the power production ability. This disadvantage is somewhat mitigated by implementing amplification mechanisms. These harvesters provide a reliable performance because the power production only depends on the relative velocity of the mass (magnet) and the magnetic flux change. So, there is no need of a separate voltage source to operate. The output tends to have a high current flow and a low voltage. Theoretically, the power density of electromagnetic VEHs is similar to

that of in piezoelectric VEHs ($300 \mu\text{W}/\text{cm}^3$ – $400 \mu\text{W}/\text{cm}^3$) (Dong et al., 2019; Wei & Jing, 2017).

A major advantage of Electrostatic VEH is the ease of integration with existing MEMS. The output is of high voltage. But a major drawback is the requirement of an external voltage source for energy conversion initiation. There are few reliability and performance concerns due to the possibility of short-circuiting of electrodes which can occur if the mechanical stops aren't performing as intended. Off axis vibrations like rotations can cause damage to the comb drives and these are single DOF harvesters. The difficulty of matching the resonant frequency at low frequency input vibrations makes these harvesters undesirable for low frequency energy harvesting. The energy density is also relatively low when compared with energy densities of piezoelectric and electromagnetic VEHs (Dong et al., 2019; Wei & Jing, 2017).

As triboelectric effect occurs between any two materials; a plethora of materials are available to be used for an optimum energy harvesting with high conversion efficiency. This is a major advantage of Triboelectric VEHs. This also ensures of low production cost and easy manufacturing processes. But, as the conductivity depends considerably on environmental factors like humidity, the stability and durability of these energy harvesting devices are also a concern. Another issue is the low current output. But as this Triboelectric VEHs are relatively new when compared with the other three transducing mechanisms, it is still unclear to decide whether these issues can be mitigated or not (Dong et al., 2019).

2.3 Amplification Methods

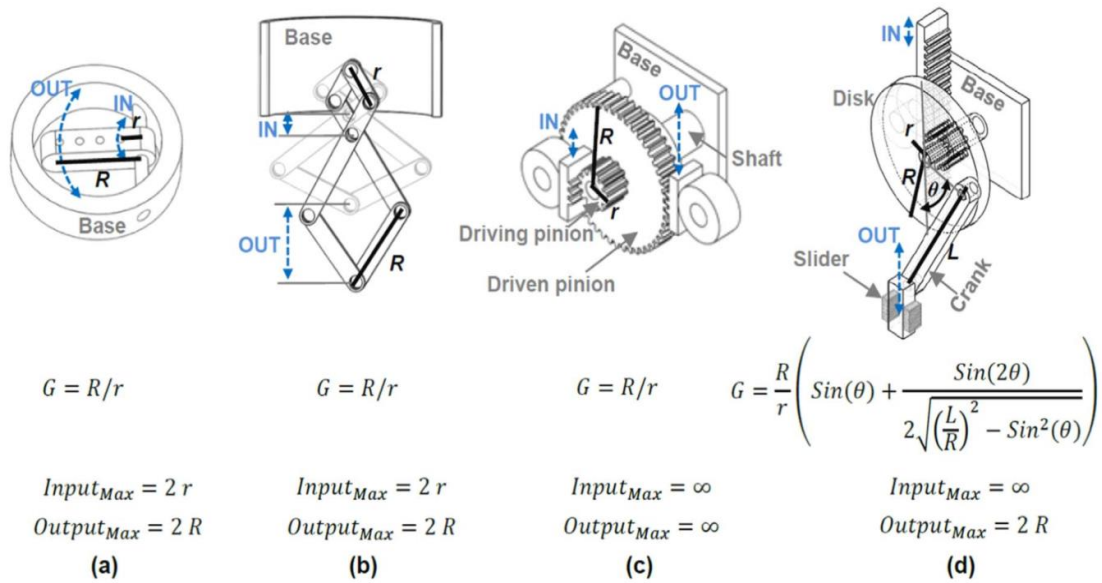
By considering Equations (12) and (23), it can be observed that the power harnessed by the energy harvester can be increased by either increasing source vibration amplitude, increasing source vibration frequency or amplifying the system frequency to match the resonant frequency of the source vibration.

2.3.1 Mechanical Amplifier

Transmission mechanism amplification is an approach that's been utilized to increase the energy harvested from the environment. Even though there is some energy loss present, the final output is still desirable than having an unamplified system. Commonly used mechanical amplification mechanisms with their respective mechanical gains are shown in Figure 2.19.

Figure 2.19

Different Mechanical Amplification Methods with Mechanical Gain (Yildirim et al., 2017; Zou et al., 2019)



In Figure 2.19, (a), (b), (c), (d) are lever mechanism, scissor mechanism, two rack and pinion mechanism, rack-pinion paired with piston motion respectively. There are differences amongst the mechanical amplifiers themselves and they should be utilized according to the specific requirement. Some amplification mechanisms have a maximum input value that can be amplified (Figure 2.19 (a), (b)) while some mechanisms can amplify all inputs regardless of their magnitude. Few mechanisms have a maximum output it can provide (Figure 2.19 (a), (b), (d)) while Figure 2.19 (c) doesn't have an output limitation.

Mechanical amplifiers are great to use specially in low frequency VEHs for amplifying the input magnitude. A drawback of this is the increase of size and volume due to the integration of the mechanical amplifier to the system. Mechanical amplifiers are used in electromagnetic VEHs to mitigate its loss of power production capacity in micro scale. (Shahosseini & Najafi, 2014) have used mechanical amplification in a low frequency application and managed to increase the output power by 16 times (Figure 2.20).

Figure 2.20

(a) Implemented System (b) Schematic View of the System (Shahosseini & Najafi, 2014)

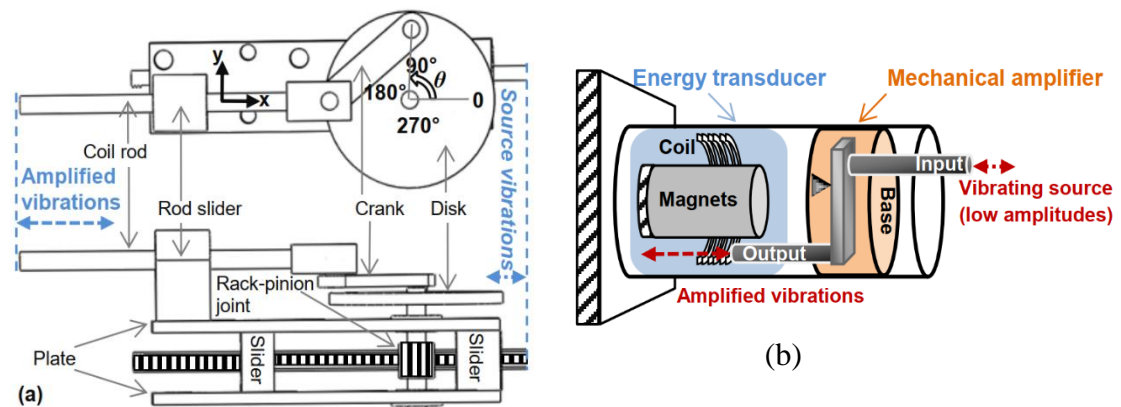
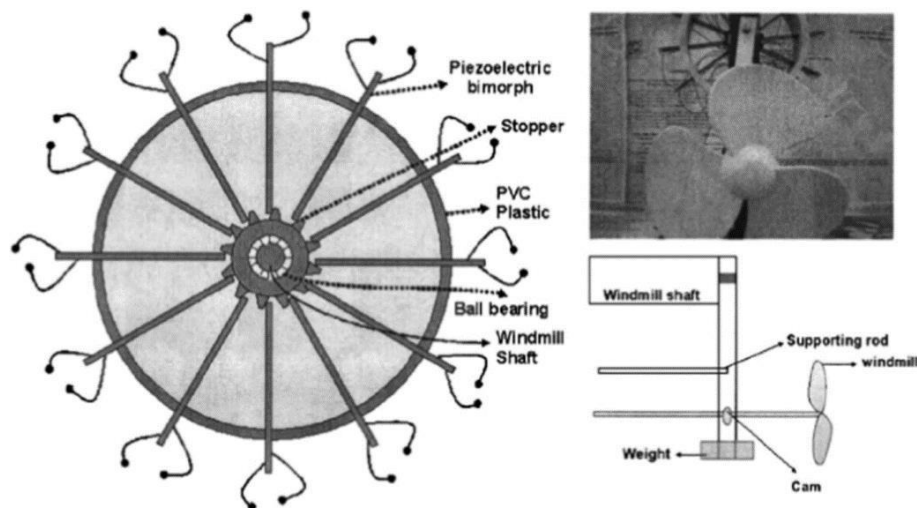


Figure 2.21

Schematic of Piezoelectric Windmill (Yildirim et al., 2017)



2.3.2 Frequency Up

Frequency up mechanisms are used to amplify the low frequency input in order to increase the power harnessed. Figure 2.21 presents a windmill prototype with ten integrated piezoelectric biomorphs. The researchers claim that they were able to obtain significant results by this frequency up implementation.

2.3.3 Resonant Tuning

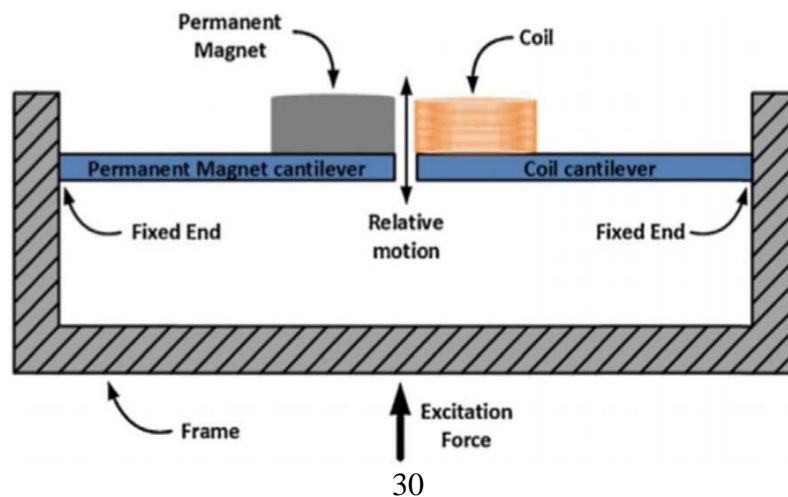
This method is changing the resonance frequency of the system to match up with a certain frequency of the system which results in a higher power output. This is achieved by either changing the effective mass by having multiple masses on a single array which will result in broadening the resonant frequency range or by changing the stiffness of the device either by preloading the system, introducing magnetic stiffness or changing load impedance in the electrical circuit (Yildirim et al., 2017).

2.3.3.1 Multiple Degree of Freedom

The operating frequency bandwidth of the system can be increased by increasing the number of masses that are utilized in the system. These masses are connected in series to increase the power harnessed by the system. Having multiple masses increases the number of resonant points of the system which increases the operating range of the device. This creation of new resonant points by increasing the number of masses is

Figure 2.22

Dual Resonating Electromagnetic Generator (Ooi & Gilbert, 2014)



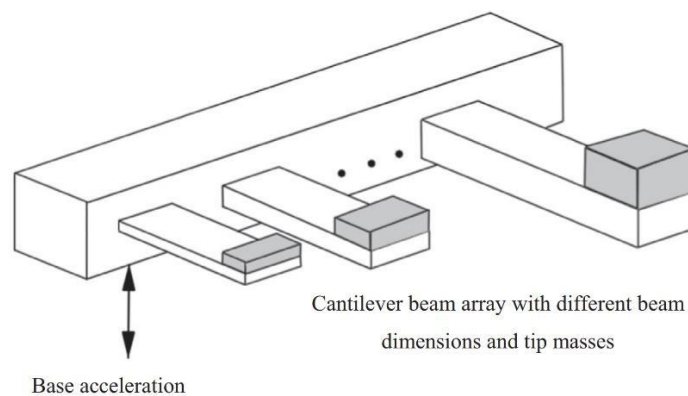
considered as increasing the degrees of freedom of the system (Yildirim et al., 2017). (Ooi & Gilbert, 2014) have presented a device with two different resonating cantilever beams made using a permanent magnet and a coil as shown by Figure 2.22. Under an acceleration of 0.8 ms^{-2} they have managed to achieve an improvement of 58.22% of the output.

2.3.3.2 Multimodal Arrays

Another design method considered to increase the operating range uses a set of different individual systems designed to resonate at different frequencies. As shown by Figure 2.23, the multimodal arrays consist of an array of cantilever beams with different tip masses and beam dimensions which results in close resonant peaks among each individual cantilever beam. This whole system increases the effective operating bandwidth of the system. (Shahruz, 2006) have used piezoelectric films as the transduction mechanism. These systems having multimodal arrays can be also called as mechanical band pass filters (Yildirim et al., 2017).

Figure 2.23

Multimodal Array Structure (Shahruz, 2006)



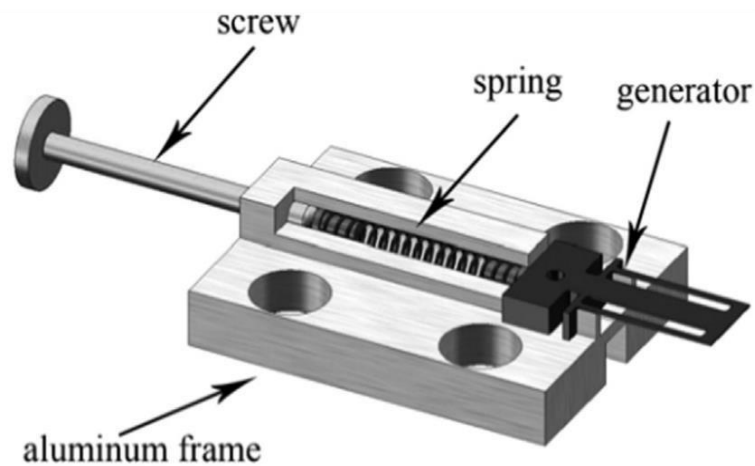
2.3.3.3 Preload

Instead of including additional masses, another method used to increase bandwidth is changing the stiffness of the system. This is achieved by applying an axial preload to

the system. Figure 2.24 shows the apparatus used by (Eichhorn et al., 2009) to apply a compressive axial preload to the tip of a cantilever beam made using piezo polymer. The natural frequency of the system is changed due to the preload imparted on the structure. By applying a compressive load, a resonant frequency shift of about 22% is achieved with a total force of 22.75 N. The operating range has increased from 315 Hz – 380 Hz to 292 Hz – 380 Hz. They have conducted another experiment by applying a tensile preload, but have only managed a resonant frequency shift of 4% (Eichhorn et al., 2009).

Figure 2.24

Design of a Compressive Axial Loader (Eichhorn et al., 2009)



2.3.3.4 Magnetic Tuning

Magnetic tuning is another method that's used to increase the resonance frequency. The natural frequency is changed by the induced magnetic force K_{mag} as it will affect the stiffness of the system. With the induced magnetic force, the stiffness of the system becomes:

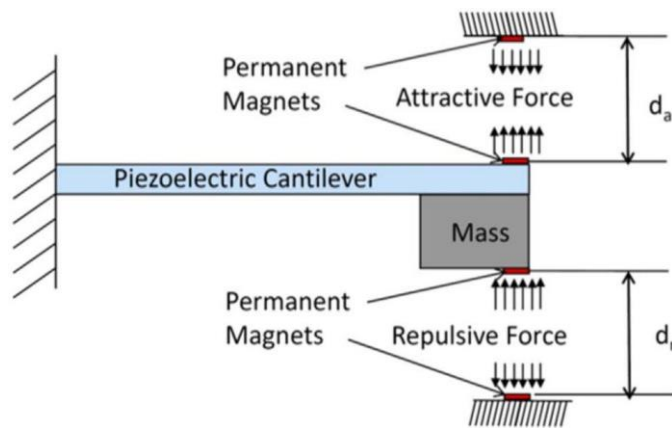
$$K_{eff} = K_{beam} + K_{mag} \quad (24)$$

Figure 2.25 depicts a piezoelectric cantilever that is incorporated with permanent magnets. The natural frequency of the system was 26 Hz. The attractive and repulsive

forces due to the permanent magnets imparts a force on the cantilever beam which results in a change of the stiffness of the beam. The volume of the device is 50 cm^3 and when the magnetic tuning was done for an acceleration amplitude of 0.8 ms^{-2} , the effective operating bandwidth increases to $22 \text{ Hz} - 32 \text{ Hz}$ and the harvested power reaches a range of $240 \text{ }\mu\text{W} - 280 \text{ }\mu\text{W}$ (Challa et al., 2008; Yildirim et al., 2017).

Figure 2.25

Cantilever Beam with Magnetic Resonance Tuning (Challa et al., 2008)



2.3.4 Hybrid Systems

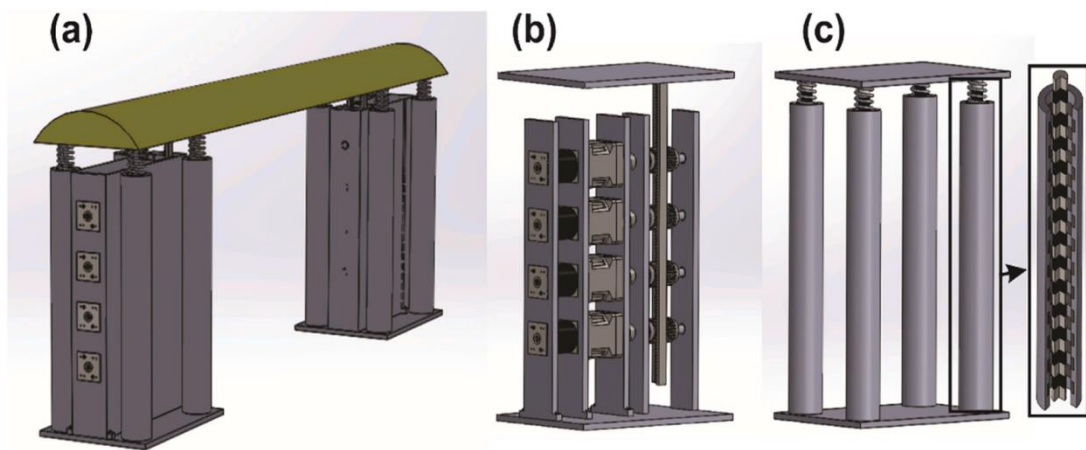
This is utilizing various types of transducing mechanisms to harness energy. Various experiments have been conducted by incorporating piezoelectric, electromagnetic and electrostatic transducing mechanisms to increase the operating frequency range of the device. (Iqbal & Khan, 2018) have combined piezoelectric and electromagnetic mechanisms to enhance the frequency bandwidth and power output. This paper was discussed earlier and Figure 2.4 shows the implemented system. (K. Fan et al., 2018) have also implemented this hybrid system to enhance the output power and to widen the operating frequency range (Figure 2.5).

(Gholikhani et al., 2021) have introduced a hybrid harvesting system which utilizes a linear generator (electromagnetic) and a rack-and-pinion to produce electric power. The prototype was made to convert energy lost from speed bumps to electricity. The maximum vertical displacement of the prototype device was limited to 90 mm. The

tests conducted shows an average power production of 1.2 W for rack and pinion-based generator and 80 mW for linear generator mechanism. The reason for the small power generation from the linear generator was because it only consisted of one electrical coil and one magnet. The prototype constructed is shown by Figure 2.26.

Figure 2.26

(a) *Final Prototype Design* (b) *R-P Mechanism* (c) *L-GE Mechanism* (Gholikhani et al., 2021)

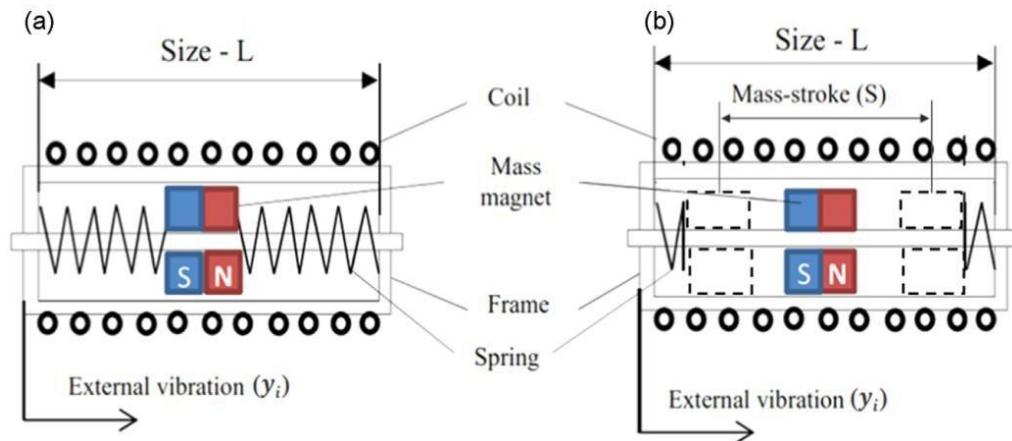


2.3.5 Free Impact Motion

Amplification using free impact motion is predominantly used in electromagnetic VEHs. The electricity generation in electromagnetic VEHs depend on the rate of change of flux that occurs in the system. The free impact motion is changing the way that the relative motion between the magnet and the coils occur in a way which increases the rate of change of flux in the harvester. The impacts that happen along the oscillation direction between the springs, magnet (mass) and the end stoppers ensure a sudden change of magnetic flux happens. This results in an increase of the induced voltage which ultimately leads to an increase of power production. This can be clarified by referring to the equations (15) and (16). Figure 2.27 shows the difference of the structure between conventional and free impact motion based electromagnetic VEHs. There are four different response types associated with free impact motion; namely

Figure 2.27

(a) Conventional Electromagnetic VEH and (b) Free Impact Motion Electromagnetic VEH (Haroun et al., 2015b)



sticking mode, free mode, impact mode and multi-impact mode (Haroun et al., 2015a, 2015b; Shen & Lu, 2020).

“Sticking mode” is the instance in which the inertia force cannot overcome the tube-magnet friction force. This happens at very low input acceleration and both the tube and the magnet moves together. No relative motion appears which results in no energy being harvested.

“Free mode” is where the inertia force overcomes the frictional force. This happens when the input acceleration is increased and a relative displacement between the tube and the magnet is available albeit the amplitude of it is not large enough to allow the magnet to reach both ends of the device periodically. Magnet freely vibrates inside the device and it may collide/impact with one end of the device.

By increasing the input acceleration further, the amplitude of the relative displacement can be increased and the system reaches “Impact Mode” when the magnet gains the ability to reach both stoppers periodically. The relative displacement takes an amplitude value of half the magnet stroke and frequency is equal to the frequency of the input vibration.

Figure 2.28

Relative Displacement for Different Modes of Motion (Haroun et al., 2015a)

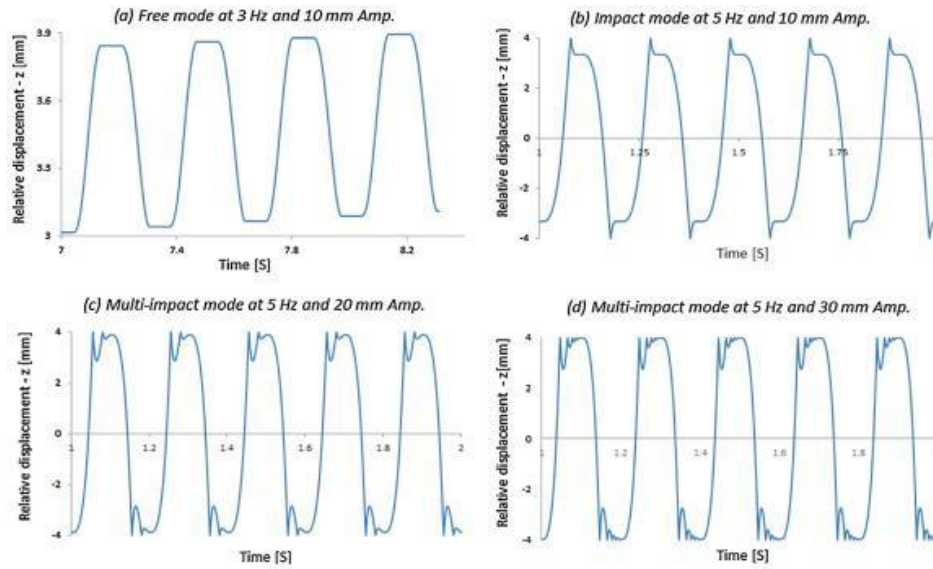
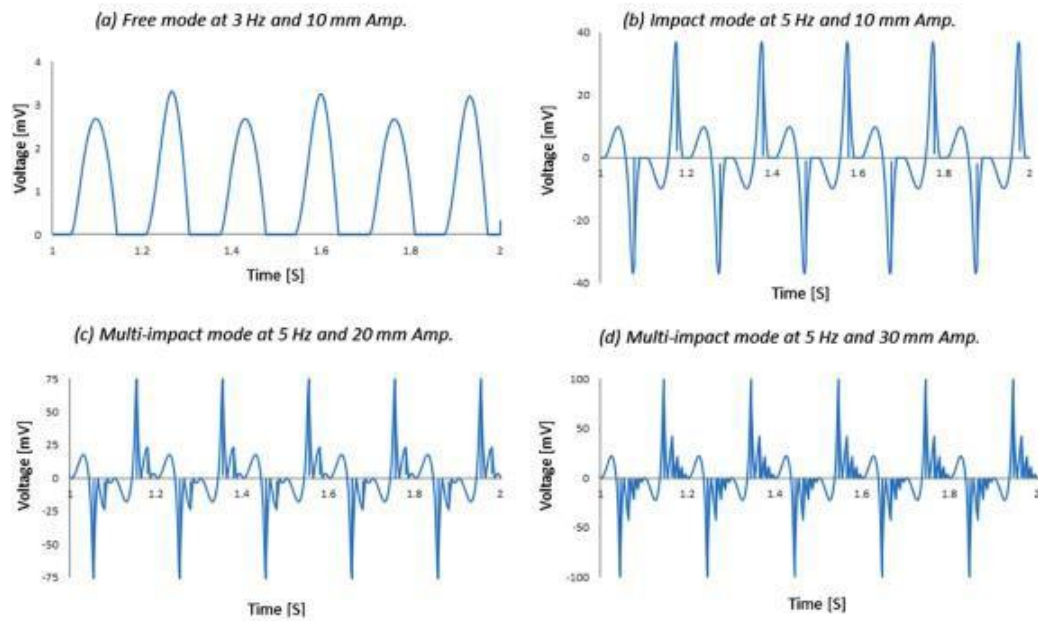


Figure 2.29

Output Voltage for Different Modes of Motion (Haroun et al., 2015a)



After the relative displacement reaches half magnet stroke, it cannot be increased further. But by increasing the input acceleration even further, the impact mode can be changed. In the “Multi-Impact mode”, the magnet collides with one end few times and then collides with the other end few times. In this mode, two or more consecutive impacts or intermediate oscillations appear within the main vibration movement and the number of those intermediate oscillations can be further increased by increasing the input acceleration.

Figure 2.28 and Figure 2.29 shows the relative displacement curves and output voltages resulted by different methods of motion for various input amplitudes and frequencies obtained for the experiments conducted by (Haroun et al., 2015a).

2.3.6 Comparison of Amplification Methods

Each of the above-mentioned amplification methods have their distinctive advantages and disadvantages. Usage of mechanical amplifiers widens the operating frequency range of the system which results in an increase of output power. This is a significant improvement that can be included for devices used to harness low frequency inputs. But by including mechanical amplifiers, the relative displacement of the mass also is increased which results in the system becoming bulkier as extra space is required to accommodate the relevant amplification mechanism. Frequency up mechanism is good for low frequency inputs and are well suited to be incorporated with MEMS devices.

In resonant tuning mechanisms which are used to change the natural frequency of the system, the devices and the overall system is complex when compared with systems with mechanical amplifiers and frequency up mechanisms. Systems with multiple DOFs only work in the vicinity of the resonant peaks and the efficiency rapidly drops otherwise. Systems with multimodal arrays widens the operating bandwidth which results in an increase of power, but the system becomes bulkier due to having multiple beams with tip masses and the electric circuitry is considerably complex. Preloading the system increases the operating range significantly, but is difficult to properly tune in practical applications. The same can be said about magnetic tuning.

A major issue commonly seen in resonant tuning VEH is that the power harvested drops rapidly when the frequency mismatch between the harvester and the excitation frequency. Designing a system which can tune itself to reach the excitation frequency as close as possible to improve the power harvested is complicated and costly when considering low frequency vibrations.

Hybrid systems which incorporate different types of transducing mechanisms increases the operating frequency range moderately, but the overall system design and the required electrical structures becomes significantly complex. The free impact motion amplification is a non-resonant type amplification process and it increases the output considerably. This amplification type is only compatible with electromagnetic VEHs.

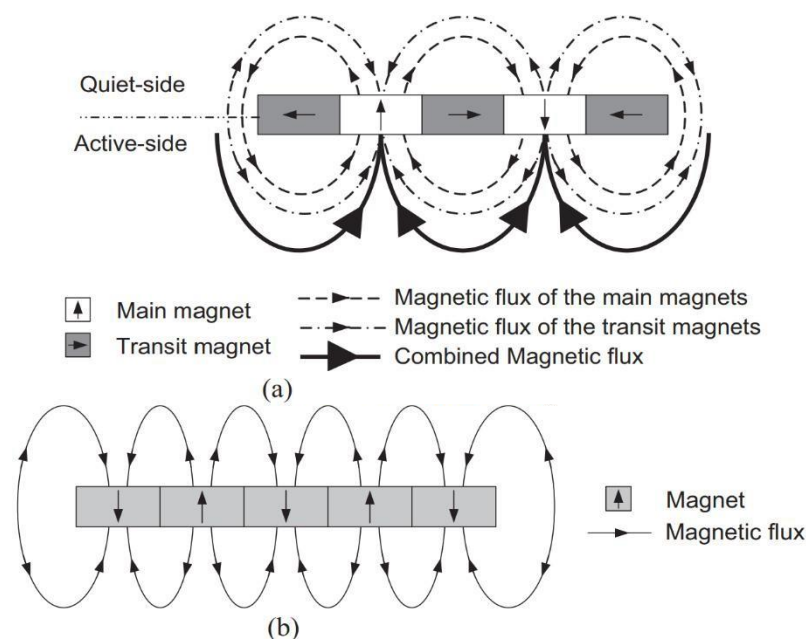
2.4 Magnetic Field Enhancement

2.4.1 Magnet Configuration

In electromagnetic VEHs, proper magnet configuration is vital because the output power is dependent on the rate of change of magnetic flux and the strength of the magnetic flux is determined by the magnet configuration. (Zhu et al., 2013) have

Figure 2.30

(a) Standard Halbach Array and (b) Normal Magnet Configuration (Zhu et al., 2013)

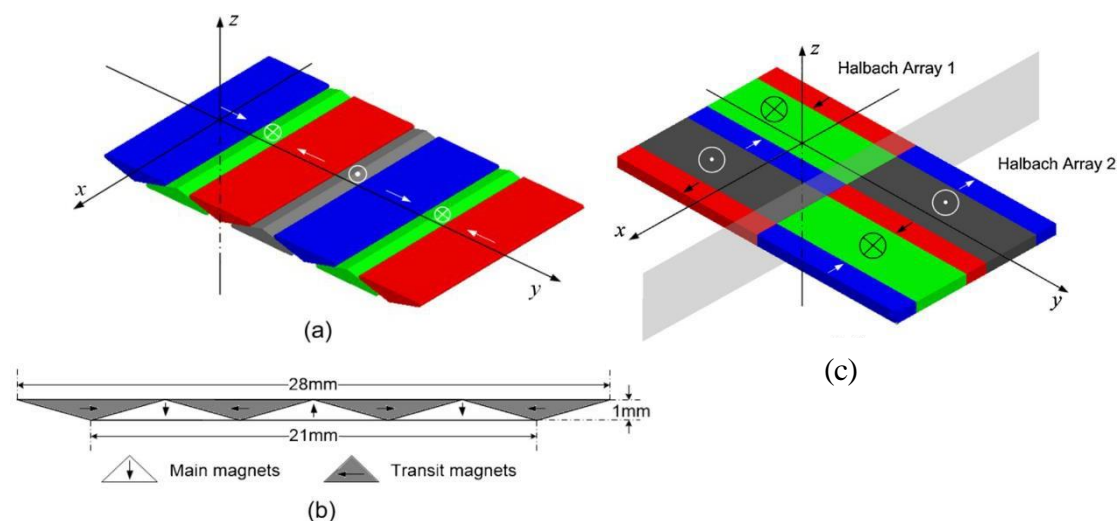


conducted an experiment to check the effect of different magnet configurations have on the power generation. They have compared normal magnets, standard Halbach array, standard Halbach array with triangular magnets and double Halbach array.

As shown by Figure 2.30 (a), Halbach array is a type of magnet arrangement that concentrates the magnetic field on one side of the array while canceling the field to almost zero on the other side. But the experiments conducted by the researchers have revealed that using a standard Halbach array doesn't necessarily increase the harvested energy as it doesn't increase the magnetic flux change rate. This is due to the existence of transit magnets in the magnet set. Although the magnetic field density is increased,

Figure 2.31

(a) Structure of and (b) Cross Section view of Triangular Halbach Array, (c) Structure of Double Halbach Array (Zhu et al., 2013)



the magnet set has to move a long distance for the magnetic flux to change significantly which results in a minimal change in the rate of magnetic flux change. (Zhu et al., 2013) have tried to address this issue in two approaches, by introducing triangular shaped magnets to the standard Halbach array and by experimenting with double Halbach arrays (Figure 2.31).

The conducted tests revealed that standard magnet configuration is better when compared with single Halbach array (both standard and triangular shaped magnets)

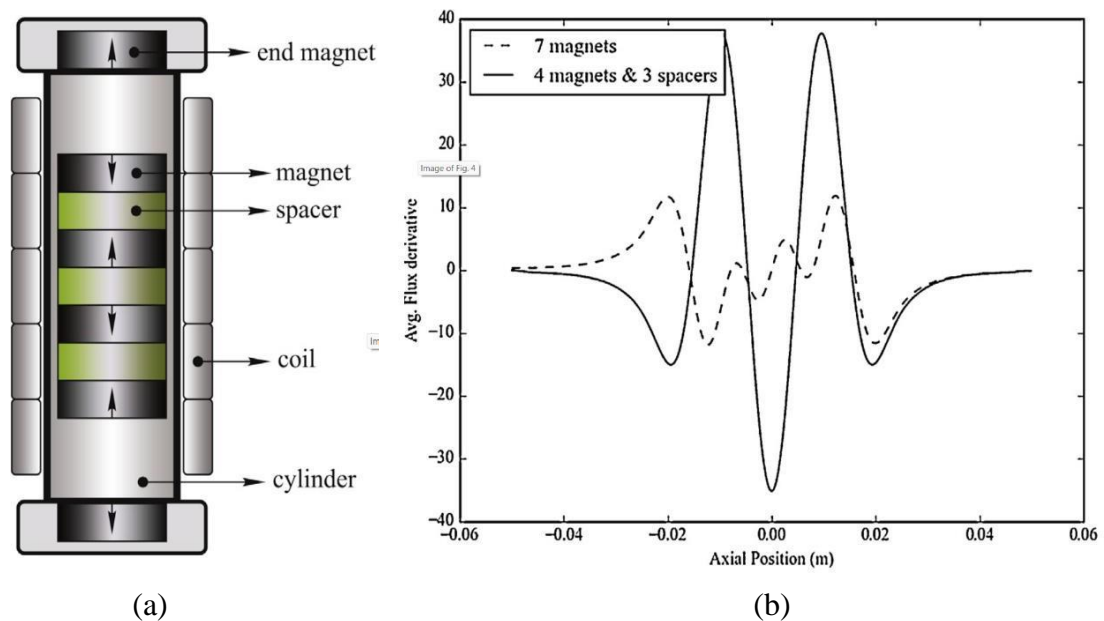
configuration. Theoretically, when compared with the standard Halbach array, Halbach array with triangular shaped magnets and double Halbach array have increased the magnetic flux change rate by 1.88 and 2.74 times respectively and the output power harvested by a factor of 3.5 and 7 respectively. But, only the double Halbach configuration managed to produce more power than the standard magnet configuration (Zhu et al., 2013). One advantage of using Halbach configuration is that the size of the device can be reduced because the magnetic field is concentrated only on one side. This is a considerable advantage when considering micro VEHs.

2.4.2 Magnetic Field Enhancement using Spacers

(Saravia et al., 2017) have conducted an experiment on a levitation based VEH. They have compared two types of stacks; a seven-magnet stack with four magnets and three spacers stack.

Figure 2.32

(a) Harvester Architecture and (b) Magnetic Flux Derivative for Different Stacks (Saravia et al., 2017)



As shown by Figure 2.32, the use of ferromagnetic spacers has drastically increased the rate of change of magnetic flux which results in a higher output power. (Saravia et al., 2017) states that the geometrical shape of the magnets and the spacers play a vital role in a higher flux derivative. The spacers have managed to not only enhance the flux derivative, but also to change the sign.

2.5 Power Management System

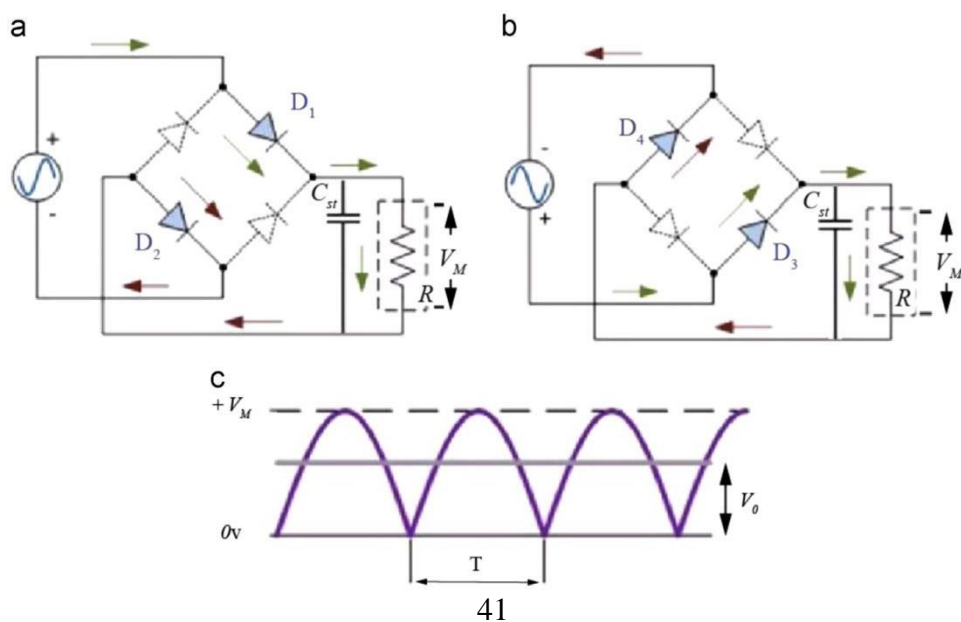
The generated power from the VEH cannot be utilized directly. It should be manipulated according to our requirements and only then it can be used efficiently and safely. This can be achieved by power conversion circuits and power storage devices.

2.5.1 Conversion Circuits

The current output of the harvesters can either be Alternating Current (AC) or Direct Current (DC) depending on various factors like the transduction mechanism, type of application, input characteristics and etc. So, it is necessary to use power conversion circuits to fine tune the output from the harvester to fulfill our requirements. Most of the power storage mechanisms that are used daily is in DC form due to its' lack of

Figure 2.33

Bridge Rectifier (a) During Positive Half-cycle, (b) During Negative Half-cycle and (c) Output Waveform (X. Wang et al., 2015)



complexity, efficiency and financial viability when compared with the AC counterparts. But, majority of VEHs produces AC power. Therefore, AC to DC power converters or Rectifiers are required to bridge the difference between the power generation and power storage technologies.

The most common rectifier used is “Bridge Rectifier” (Figure 2.33) which efficiently converts full AC cycle into DC providing a smooth DC output. To further smoothen the DC output of the bridge rectifier, a capacitor is connected parallel to the load. Since capacitors doesn't allow sudden changes in voltage to occur, it acts as a filter which gets charged during peaks of the waveform and discharges during troughs which results in a more stable DC output voltage.

2.5.2 Storage Types

Power storage components are differentiated based on specifications like the specific energy, specific power, charge and discharge rate, cycle life and type of application. Specific energy is the amount of energy that can be stored per unit mass. In other words, this is the energy density of the material and it is measured in watthours per kilogram (Wh/kg). Specific power is the power output per unit mass and is usually measured by watts per kilogram (W/kg). Some commonly used power storage types at present are Batteries, Capacitors, Super Capacitors (Ultracapacitors) and Flywheels.

In batteries (Figure 2.34(a)), the energy is stored in a chemical form and it gets released when needed via chemical reactions amongst the materials in the battery. The energy density (specific energy) of batteries is higher than other types of storage devices. The charging and discharge rates of batteries are slower when compared with capacitors and supercapacitors. Due to the degradation of the materials inside the batteries, they have a limited life cycle and degrades over time.

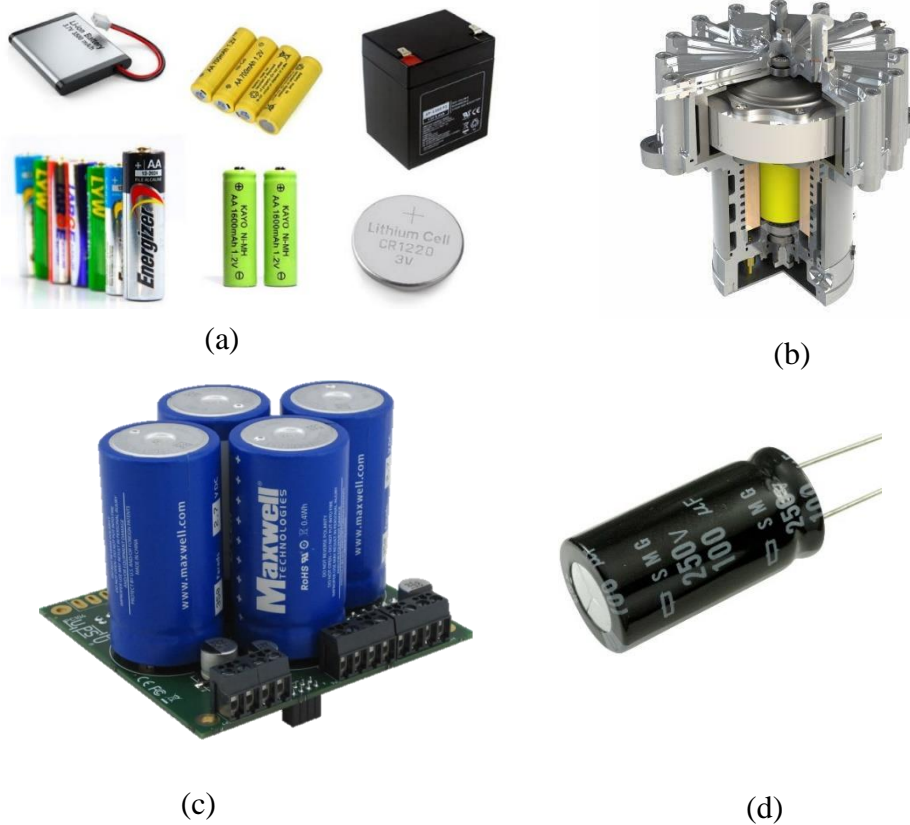
Capacitors (Figure 2.34(d)) and Supercapacitors (Figure 2.34(c)) use the same storage mechanism albeit the latter having a higher capacitance. They accumulate and maintain an electric charge on two conductive plates separated by a dielectric material. The energy densities are lower than batteries with that of capacitors being the lowest among

them. But the charge and discharge rates of these are better than batteries making them suitable for applications that need quick bursts of energy. The life cycle of these two types is also better than that of batteries. Capacitors have an additional advantage of being able to smoothen the output signals.

Flywheels (Figure 2.34(b)) stores energy as rotational kinetic energy. This is basically a spinning mass and is couple with a motor to convert the mechanical energy to electrical energy. In the energy density aspect, flywheels are better than capacitors, but lower than batteries. Flywheels have a very high charge and discharge rate which makes them suitable for high-power applications. They also have a high life cycle than batteries and are usually used for scenarios that require short-term backup power and to smoothen the output energy.

Figure 2.34

(a) Battery Variations, (b) Flywheel, (c) Supercapacitors and (d) Capacitors



2.6 Efficiency

Efficiency is a fundamental parameter that is used to evaluate performance of any machine, process, or device. This can be depicted simply as:

$$Efficiency (\eta) = \frac{Work\ Output\ (W_{out})}{Work\ Input\ (W_{in})} \quad (25)$$

Efficiency of mechanical energy harvesters tends to have a lower value which hinders its' usage in practical applications (Zou et al., 2019). The total efficiency of the system depends on the efficiencies of the subsystems incorporated; amplification systems, transduction system and the electrical system. (Zou et al., 2019) has proposed Equation (26) to calculate the system efficiency.

$$\eta_S = \eta_m \eta_t \eta_e \quad (26)$$

Where,

η_S : System efficiency

η_m : Mechanical modulation efficiency

η_t : Transducer conversion efficiency

η_e : Electrical circuit efficiency

By observing Equation (26), it can be concluded that incorporating mechanical modulation methods like input amplification can result in increasing the system efficiency.

The expression presented by (Wei & Jing, 2017) to describe the efficiency of mechanical to electrical energy conversion is shown by Equation (27).

$$\eta = \frac{k_e^2}{4 - 2k_e^2} \quad (27)$$

k_e^2 is the electromechanical coupling factor and this differs for piezoelectric, electrostatic and electromagnetic systems.

$$\text{Piezoelectric:} \quad k_e^2 = \frac{d_{st}^2 E_Y}{\epsilon_d} \quad (28)$$

$$\text{Electromagnetic:} \quad k_e^2 = \frac{(Bl)^2}{k_{sp}L} \quad (29)$$

$$\text{Electrostatic:} \quad k_e^2 = \frac{V_{in}^2 C_{max}^2}{V_{in}^2 C_{max}^2 + m\omega^2 z_s^2 C(z_s)} \quad (30)$$

Where,

d_{st}^2 : Piezoelectric strain coefficient ϵ_d : Dielectric constant

E_Y : Young's Modulus B : Magnetic field

l : Length of the wire in the coil k_{sp} : spring constant

L : Coil inductance z_s : Displacement of the top electrode

V_{in} : Input Voltage C_{max} : Maximum Capacitance position

$C(z_s)$: Capacitance of the structure

By considering Equation (27) and Equation (29), it can be observed that the efficiency increases when the magnetic field and the wire length of the coil are increased, when a spring with low stiffness which results in low spring constant is used and the coil inductance is kept low. But the major bottleneck is the conversion from mechanical to electrical energy as in this process, a considerable amount of energy is lost due to friction and other environmental conditions.

(H. Wang et al., 2018) has tested an Electromagnetic harvesting system which uses a Supercapacitor to store energy converted from swaying cables. The efficiency of this system is cited as 55%. (X. Wang et al., 2015) has compared the harvested power and efficiencies of various Electromagnetic harvesters with Piezoelectric counterparts. They have concluded that the maximum harvested power that can be achieved is 1/8th

of the maximum input power and the efficiency is about 50%. (Wei & Jing, 2017) have compared few piezoelectric, electromagnetic, electrostatic energy harvesters and their efficiencies vary in a range of 35% to 50%.

Even though these values are not much promising, it must be noted that the efficiency of these vibration energy harvesting systems is far better than the efficiency of commercially available solar panels which is typically hovering in the range of 15% to 22%.

CHAPTER 3

METHODOLOGY

3.1 Overview

This thesis focuses mainly on the development of a single DOF Electromagnetic Free Impact motion type VEH for low frequency vibrations. The idea was to design a prototype which has a higher power density than regular Electromagnetic VEHs. This high-power density and wider operating frequency range is to be achieved by implementing following mechanisms.

1. Integrating a mechanical amplifier to enhance the input vibration amplitude.
2. Implementing Free Impact motion to increase the average magnetic flux derivative and the operating frequency bandwidth.
3. Utilizing magnet spacers to enhance the magnetic flux derivative.

The implemented system can be divided into sections as Input Vibration Platform, Mechanical Amplifier, Energy Harvester and Power Circuit for ease of understanding.

The Input Vibration Platform is used to generate the vibration input according to the predetermined amplitude and frequency. The platform is be able to provide inputs with an amplitude from 0.1 cm up to 4 cm and frequency from 0 Hz up to 5 Hz.

The Mechanical Amplifier was a rack and pinion with piston motion as similar to that of in Figure 2.19 (d) as limiting the maximum allowable output is crucial in protecting the components of the system. This is used to amplify the magnitude of the input vibration. In the Energy Harvester, the conversion of translational motion into electrical energy occurs. In the power circuit, all the related power conversions occur.

The functionality diagram and the overall system diagram are depicted by Figure 3.1 and Figure 3.2 respectively.

Figure 3.1

Overall Functionality Diagram

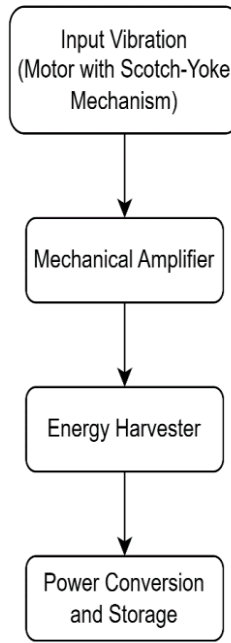
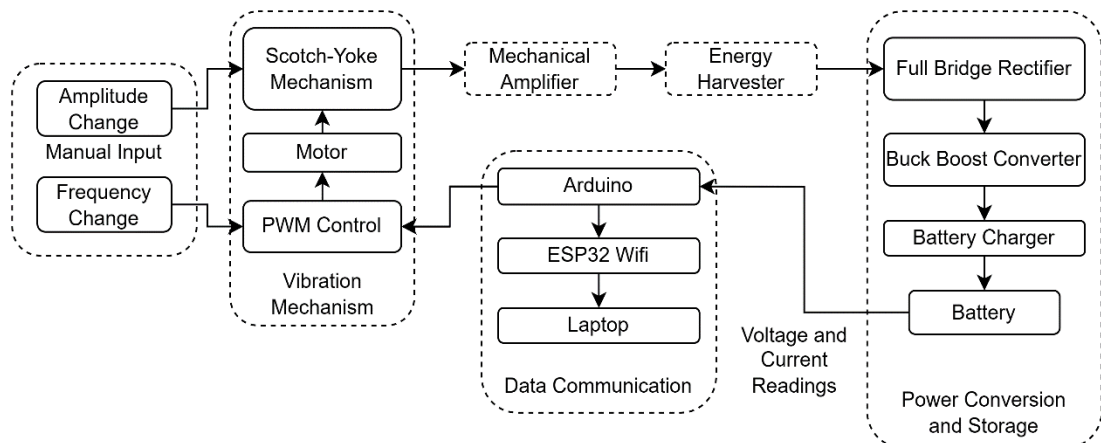


Figure 3.2

Schematic Diagram



3.2 Simulation Related Design

The mathematical model for the simulation was built in MATLAB 2022b. The following equations were modelled using MATLAB Simulink and the necessary results were obtained. The results will be discussed in next chapter. The Overall design of the system is depicted by Figure 3.3.

3.2.1 Equations

(Haroun et al., 2015a, 2015b) mentions that electrical voltage generated by induction due to relative motion can be found using Faraday's Law (Equation (31)).

$$emf = -\frac{d\varphi}{dt} = -\frac{d\varphi}{dz} \left| \frac{dz}{dt} \right| \quad (31)$$

The total magnetic flux through the coil turns is φ . As the polarity of emf depends on the direction of the relative displacement, the absolute value of relative velocity (dz/dt) is taken. Magnet relative displacement is z (Haroun et al., 2015a, 2015b).

As the magnetic flux rate change depends on the number of turns, layers and the distance of the coil from the dipole center of the magnet, it must be approximated via a mean coil layer to make the calculations easier. The magnetic flux through one turn of the mean coil layer (φ_t) located at a distance z from the magnet dipole center is obtained by integrating the equation of the magnetic flux density or magnetic field through the turn over the area bounded by the turn (Haroun et al., 2015a, 2015b). It is expressed by Equation (32).

$$\varphi_t = \frac{\mu_0 m}{2} \left[\frac{1}{\sqrt{(r^2 + z^2)}} - \frac{z^2}{(r^2 + z^2)^{3/2}} \right] \quad (32)$$

Where μ_0 is permeability of free space, m is magnetic moment and r is coil mean radius.

When Equation (32) is differentiated, magnetic flux change through one coil turn with a mean radius of r which is located at z distance from the magnet dipole center (Haroun et al., 2015a, 2015b). It is expressed by Equation (33).

$$\frac{d\phi_t}{dz} = \frac{\mu_0 m}{2} \left[\frac{3z^3}{(r^2 + z^2)^{5/2}} - \frac{3z}{(r^2 + z^2)^{3/2}} \right] \quad (33)$$

Equation (34) shows the total flux change through the whole coil. This is the summation of magnetic flux change through each turn of the mean layer multiplied by the number of layers (Haroun et al., 2015a, 2015b).

$$\frac{d\phi}{dz} = N_l \frac{\mu_0 m}{2} \sum_{n=-N_t/2}^{n=N_t/2} z_n \left[\frac{3z_n^2}{(r^2 + z_n^2)^{5/2}} - \frac{3}{(r^2 + z_n^2)^{3/2}} \right] \quad (34)$$

$$z_n = z + n \left(\frac{l}{N_t - 1} \right) \quad (35)$$

Where,

l : length of the electric coil N_t : number of turns per each layer

N_l : number of coil layers

The induced voltage in a closed loop electrical circuit is expressed by,

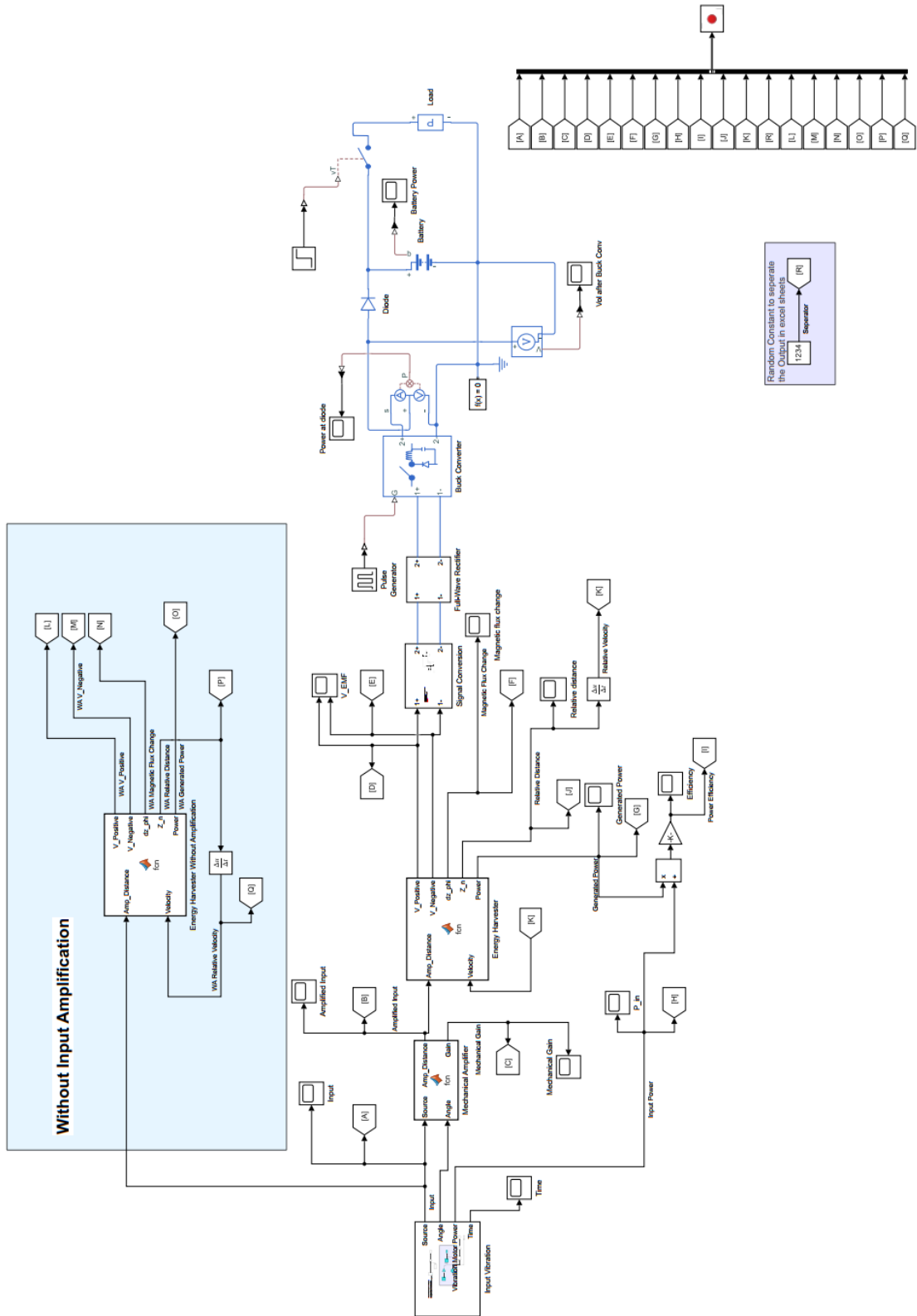
$$emf - L \frac{di}{dt} = iR \quad (36)$$

Where L is the coil inductance and R is the total circuit resistance. As the voltage drop across the inductor is very minimal when compared with the emf, the power generated by induction (P) can be calculated using Equation (37).

$$P = \frac{emf^2}{R} \quad (37)$$

Figure 3.3

Overall System Designed using MATLAB Simulink



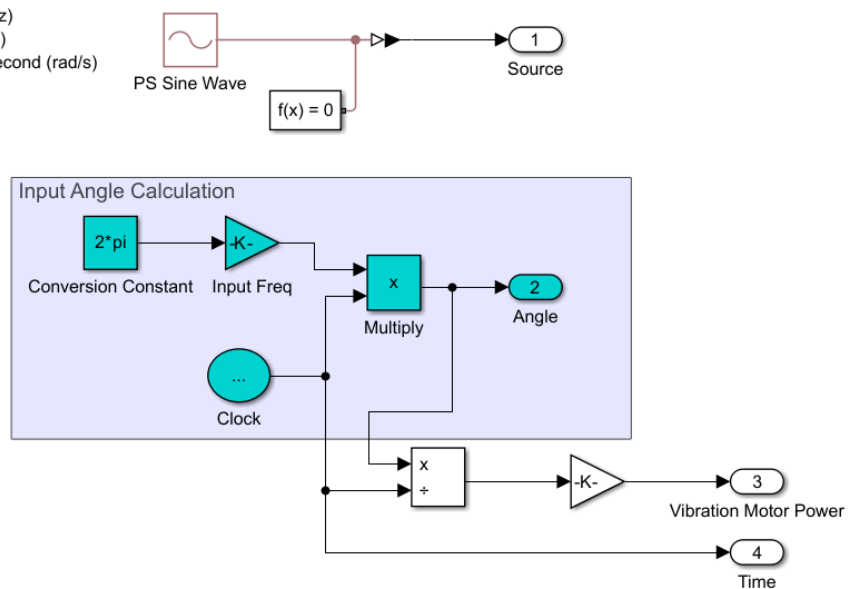
3.2.2 Input Vibration Platform

This was modelled using math blocks and electrical blocks. Since this thesis is focused on oscillatory motion, a sine wave block is used. As shown in Figure 3.4, the input frequency should be provided in Hertz and output angle is obtained in radians for ease of calculations as the default angle format used in MATLAB is in radians.

Figure 3.4

Modelled Input Vibration Platform

1. Input Frequency is in Hertz (Hz)
2. Output angle is in radians (rad)
3. Angular Speed is in radians/second (rad/s)



3.2.3 Mechanical Amplifier

Figure 3.5

Modelled Mechanical Amplifier

```

My_System_Copy_Full_Numerical_V2 ▸ Mechanical Amplifier
1  function [Out, Gain]= fcn(Source, Angle)
2  %Values in mm
3  Rval = 25*10^(-3);
4  rval = 06*10^(-3);
5  Lval = 40*10^(-3);
6
7  % pre allocating and initializing variables
31 x = sin(Angle) + (sin(2*(Angle))/2*sqrt(power(Lval/Rval,2) - power(sin(Angle),2)));
32 Gain = abs((Rval/rval)*x);
33 Out = Gain * Source;
34

```

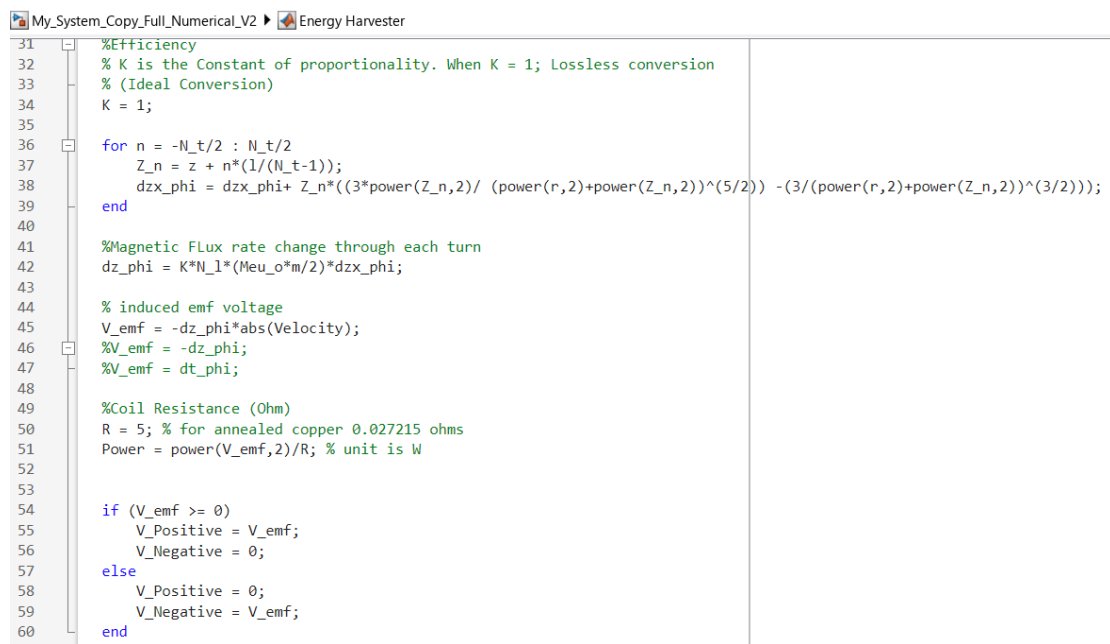
A “user-defined function block” was used to model the mechanical amplifier as it was easier. The equation shown in Figure 2.19(d) was modelled as the mechanical amplifier is made by a combination of rack-and-pinion system and a slider-crank system.

3.2.4 Electromagnetic Harvester

The equations presented in “3.2.1 Equations” were used to model the electromagnetic harvester. The parameter values were set according to the actual components that were used to fabricate the prototype. Those parameter values are discussed in “3.5 Fabrication”.

Figure 3.6

Modelled Electromagnetic Harvester



```

31 %Efficiency
32 % K is the Constant of proportionality. When K = 1; Lossless conversion
33 % (Ideal Conversion)
34 K = 1;
35
36 for n = -N_t/2 : N_t/2
37     Z_n = z + n*(1/(N_t-1));
38     dzx_phi = dzx_phi+ Z_n*((3*power(Z_n,2)/ (power(r,2)+power(Z_n,2))^(5/2)) -(3/(power(r,2)+power(Z_n,2))^(3/2)));
39 end
40
41 %Magnetic FLux rate change through each turn
42 dz_phi = K*N_l*(Meu_o*m/2)*dzx_phi;
43
44 % induced emf voltage
45 V_emf = -dz_phi*abs(Velocity);
46 %V_emf = -dz_phi;
47 %V_emf = dt_phi;
48
49 %Coil Resistance (Ohm)
50 R = 5; % for annealed copper 0.027215 ohms
51 Power = power(V_emf,2)/R; % unit is W
52
53
54 if (V_emf >= 0)
55     V_Positive = V_emf;
56     V_Negative = 0;
57 else
58     V_Positive = 0;
59     V_Negative = V_emf;
60 end

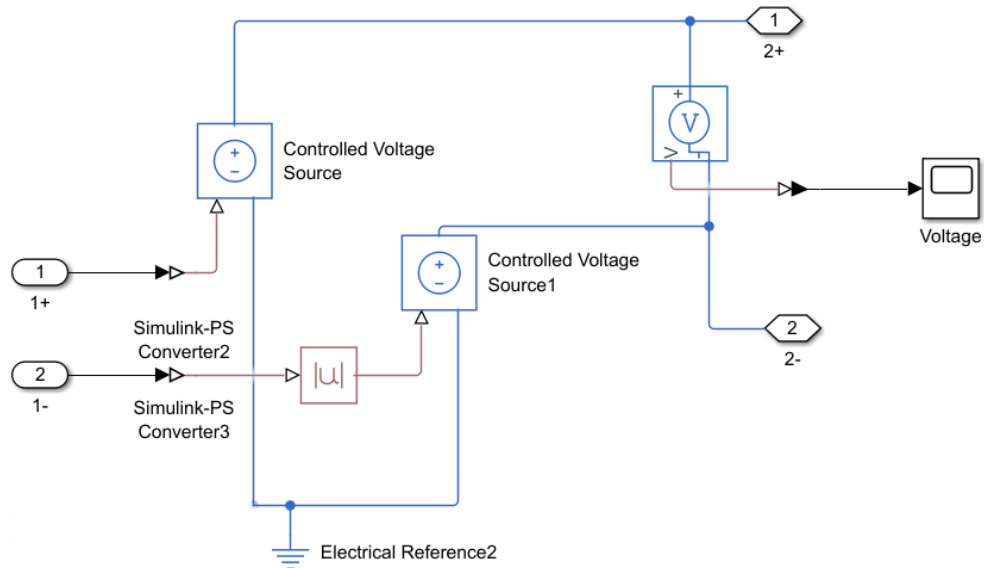
```

3.2.5 Power Collector

As the power collector comprised of electrical components, it was modelled using components from “Simscape Electrical” library. Figure 3.7 shows the block that was made to covert the Simulink numerical signal values of the Energy Harvester to physical signals which is compatible with Simscape Electrical components.

Figure 3.7

Signal Conversion Block



The converted emf signal was an AC signal. Therefore, a full-bridge rectifier was implemented to convert it to a DC voltage signal. Then, the voltage was smoothed with the help of a Buck Converter and energy was stored in a 3.7 V LiPo battery (Figure 3.9).

Figure 3.8

Modelled Full-Wave Bridge Rectifier

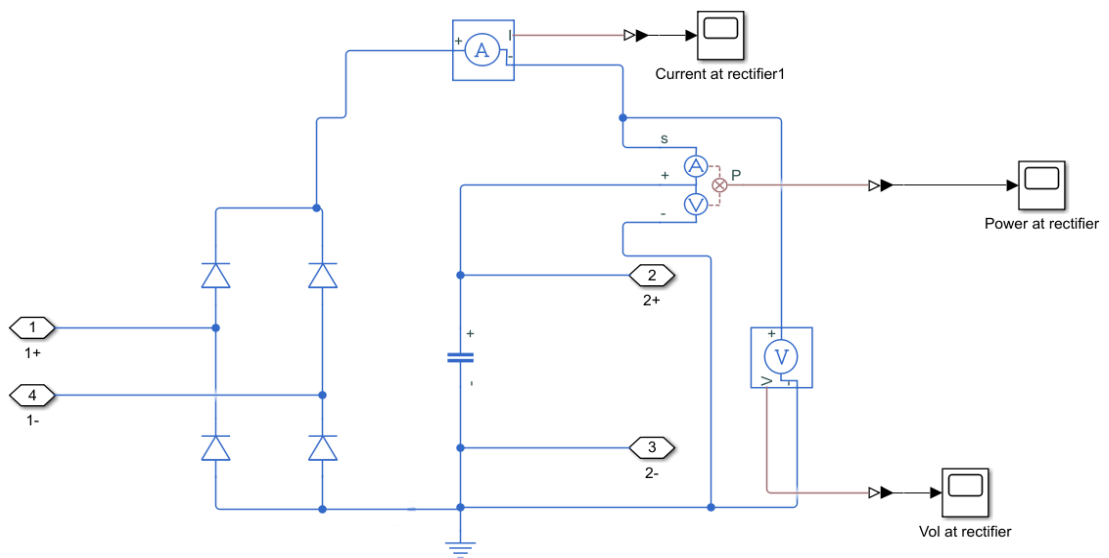
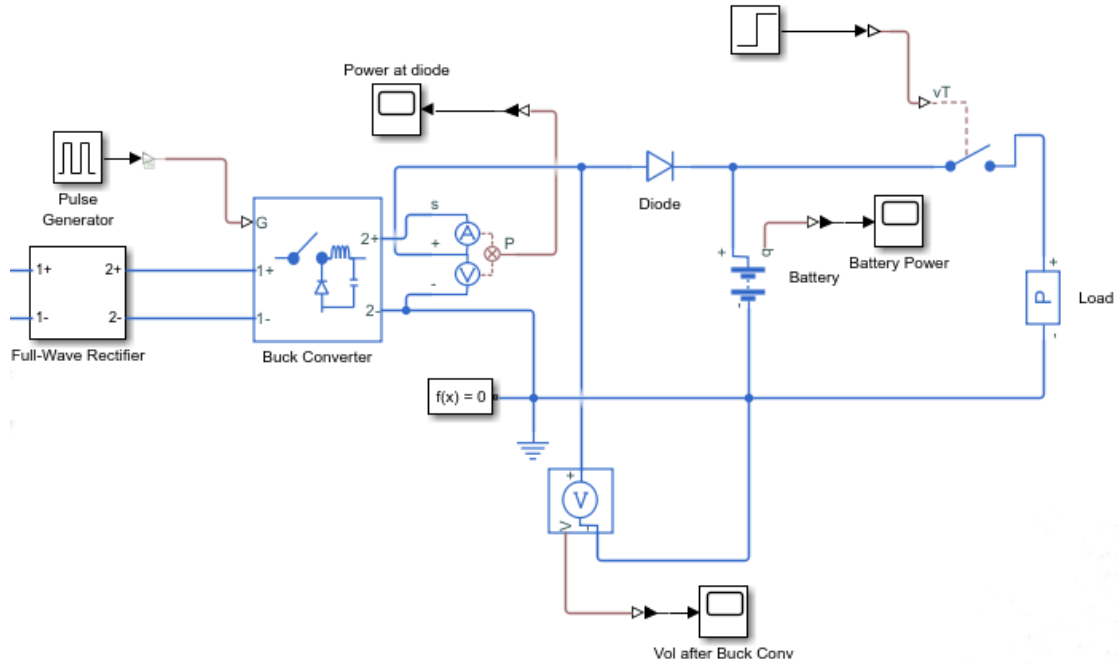


Figure 3.9

Modelled Power Collector Section



3.3 CAD Model

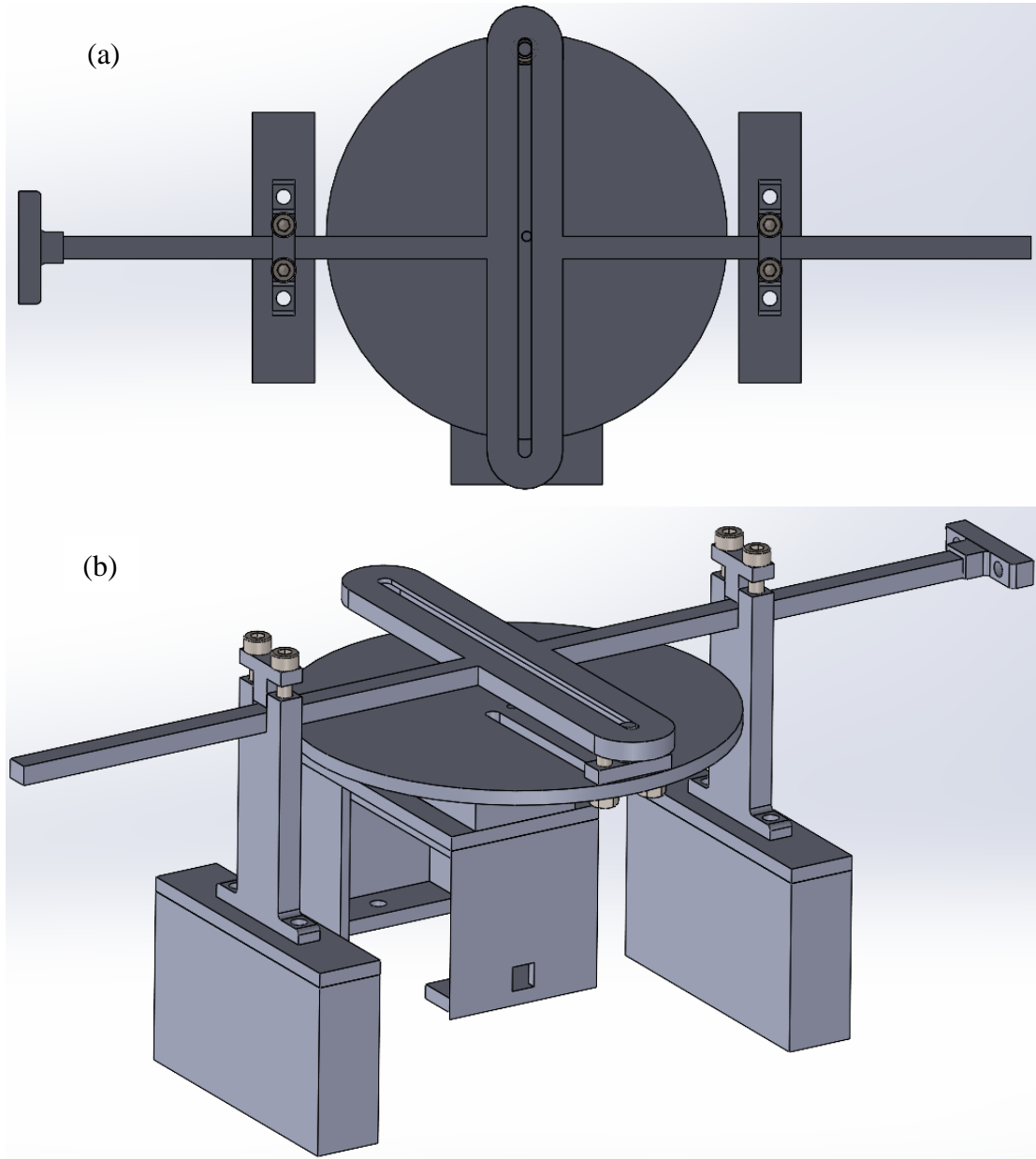
The mechanical model of the prototype was designed using SOLIDWORKS 2022. Mechanical Model was divided as Input Vibration Platform, Mechanical Amplifier and Energy Harvester.

3.3.1 Input Vibration Platform

A Scotch-Yoke mechanism was considered to be used as the vibration source. The system was to have the ability adjust its' vibration frequency and the amplitude. To accommodate the amplitude manipulation, a sliding slot was included in the design. The frequency is controlled using PWM method. The Rotating disc connected to the motor has a diameter of 9 cm to make the amplitude changes from 0.1 cm to 4 cm viable. The design is depicted by Figure 3.10.

Figure 3.10

(a) Top view (b) Side view of the Modelled Vibration Input System



3.3.2 Mechanical Amplifier

Two versions of mechanical amplifiers; the intended rack-and-pinion coupled with slider-crank mechanism (Figure 3.11) and a rack-and-pinion coupled with a scotch-yoke mechanism (Figure 3.12) were modelled and fabricated to check the functionality.

In the amplifier, the pinion pitch diameter was set to 6 mm and disc diameter was set to 25 mm. The crank length was taken as 40 mm. The slider was 50 mm in length and required guide mechanisms were modelled and assembled to ensure proper translational motion of the slider. The Mechanical Amplifier with Slider-Crank was selected to be used in the prototype.

Figure 3.11

Mechanical Amplifier with Slider-Crank Mechanism

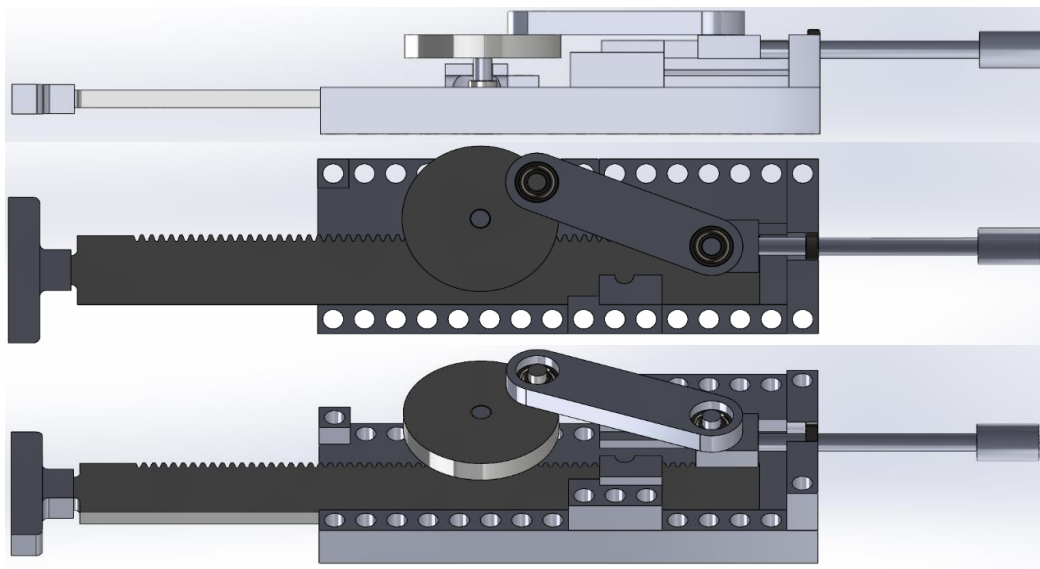
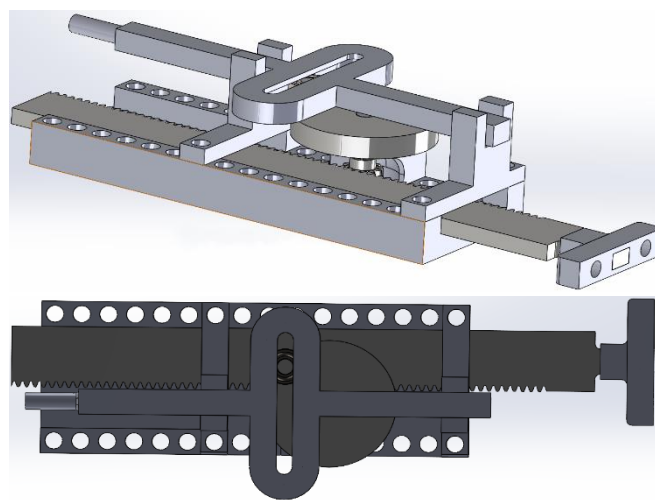


Figure 3.12

Mechanical Amplifier with Scotch-Yoke Mechanism

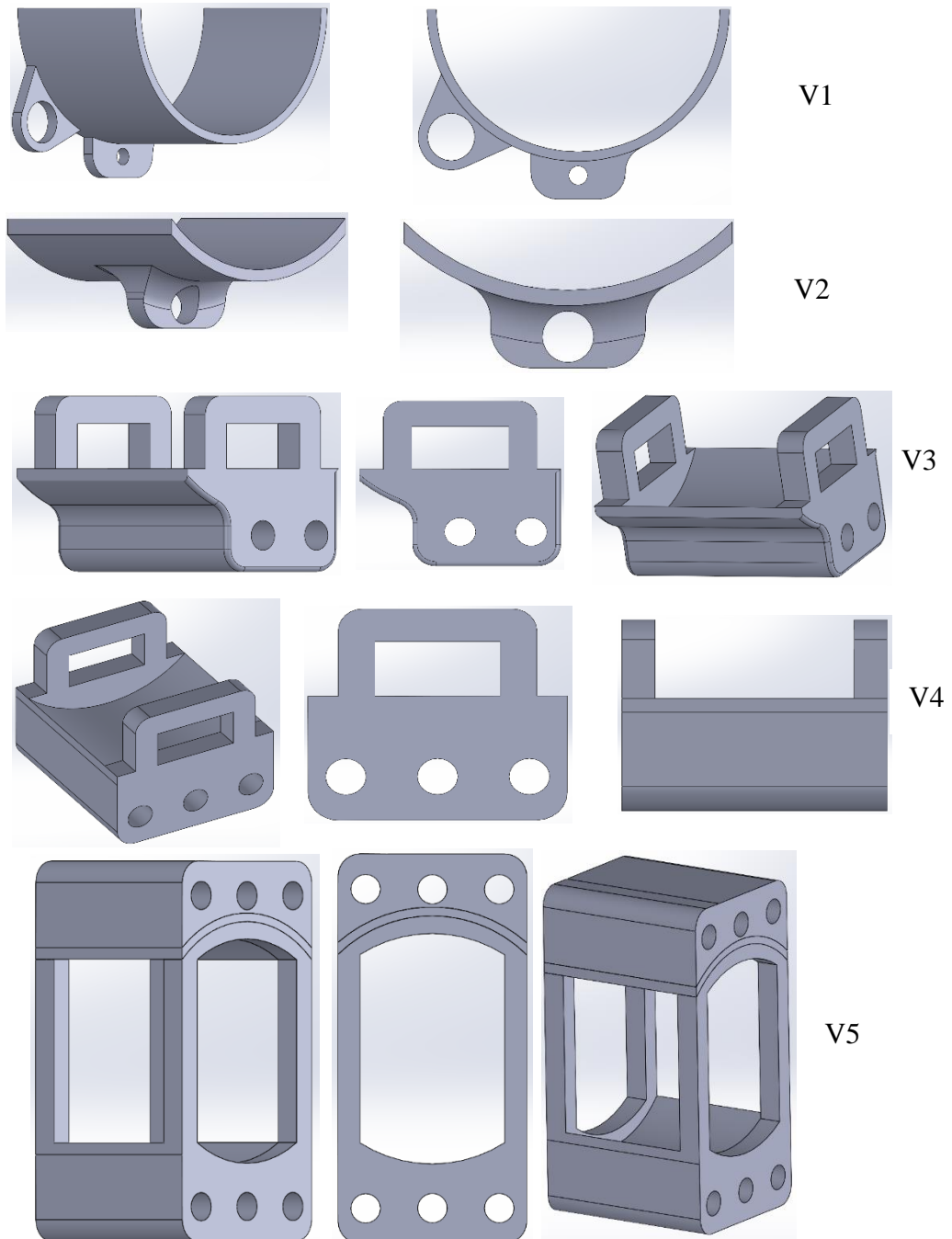


3.3.3 Energy Harvester

The Energy harvester was modelled as few separate sectors. The “moving mass” was the section that held the magnets and spacers. The “end holders” were the parts that

Figure 3.13

Versions of Moving Mass Holder



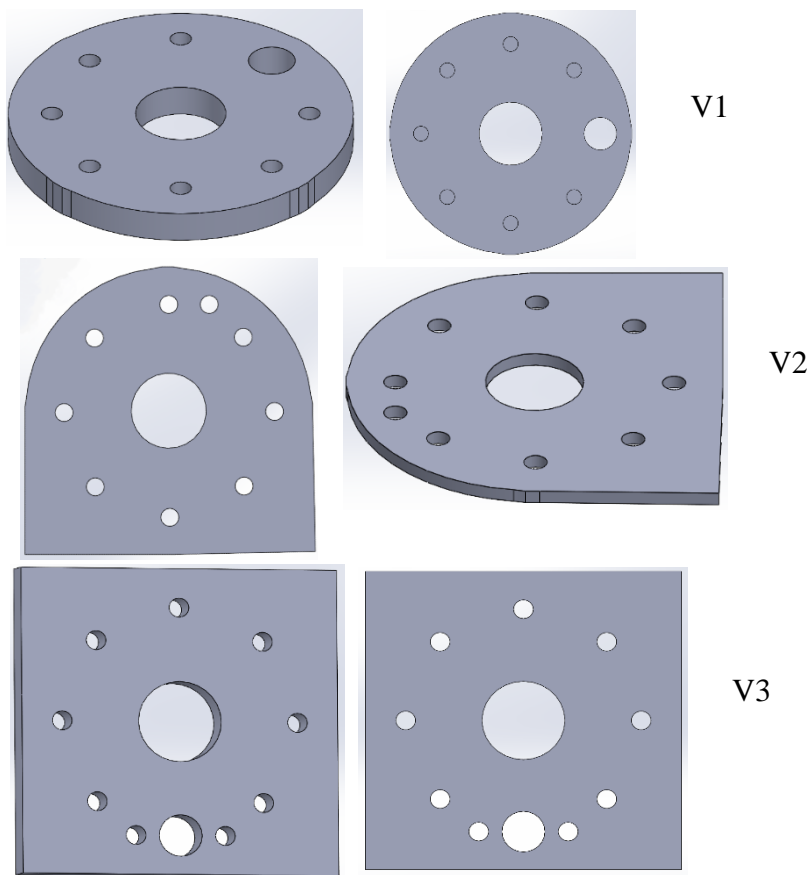
were used to hold the Steel rods and guide rods which made up the structure of the energy harvester. Then “End base holders” were used to mount the energy harvester to the base.

The moving mass (magnets with spacers) consists of 5 magnets and 4 spacers with each piece having a diameter of 30 mm and a thickness of 2 mm. Few versions of moving mass holder were modelled, fabricated and tested. After testing, evaluating the complexity and practicality, “V4” version of the moving mass assembly was used in the prototype.

The end holders had all the required holes to hold the guide rods, springs, steel rods. It was a Square with a length of 53 mm and a thickness of 5 mm. As was the case with

Figure 3.14

Versions of End Holders



“moving mass” section, few versions were designed and after evaluating each iteration, “V3” was used in the final fabrication.

The end base holder and steel rods designed are shown in Figure 3.15. The Final design of the energy harvester system is shown by Figure 3.16.

Figure 3.15

(a) Steel Rod (3 mm diameter, 70 mm length) (b) End Base Holder

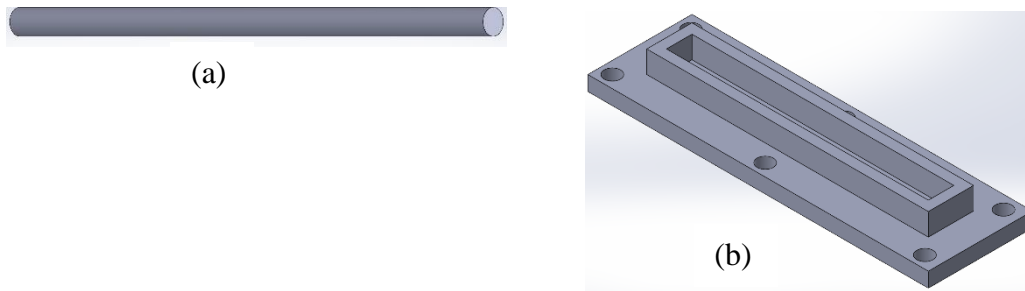
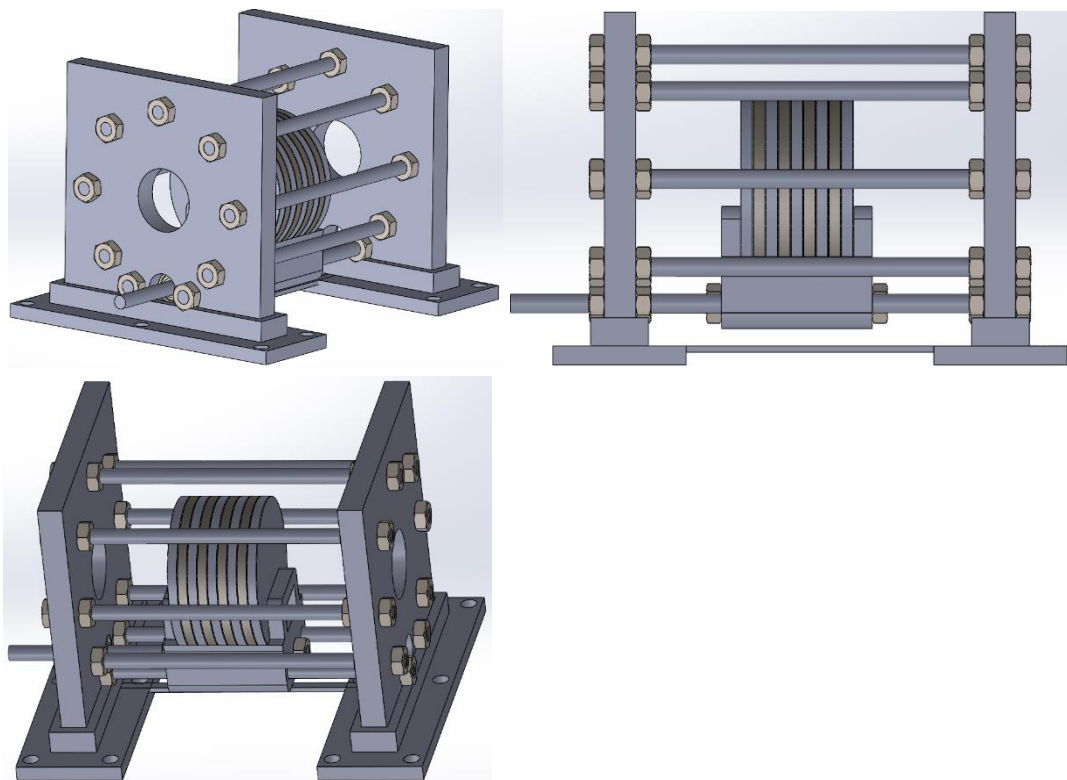


Figure 3.16

Final Energy Harvester System

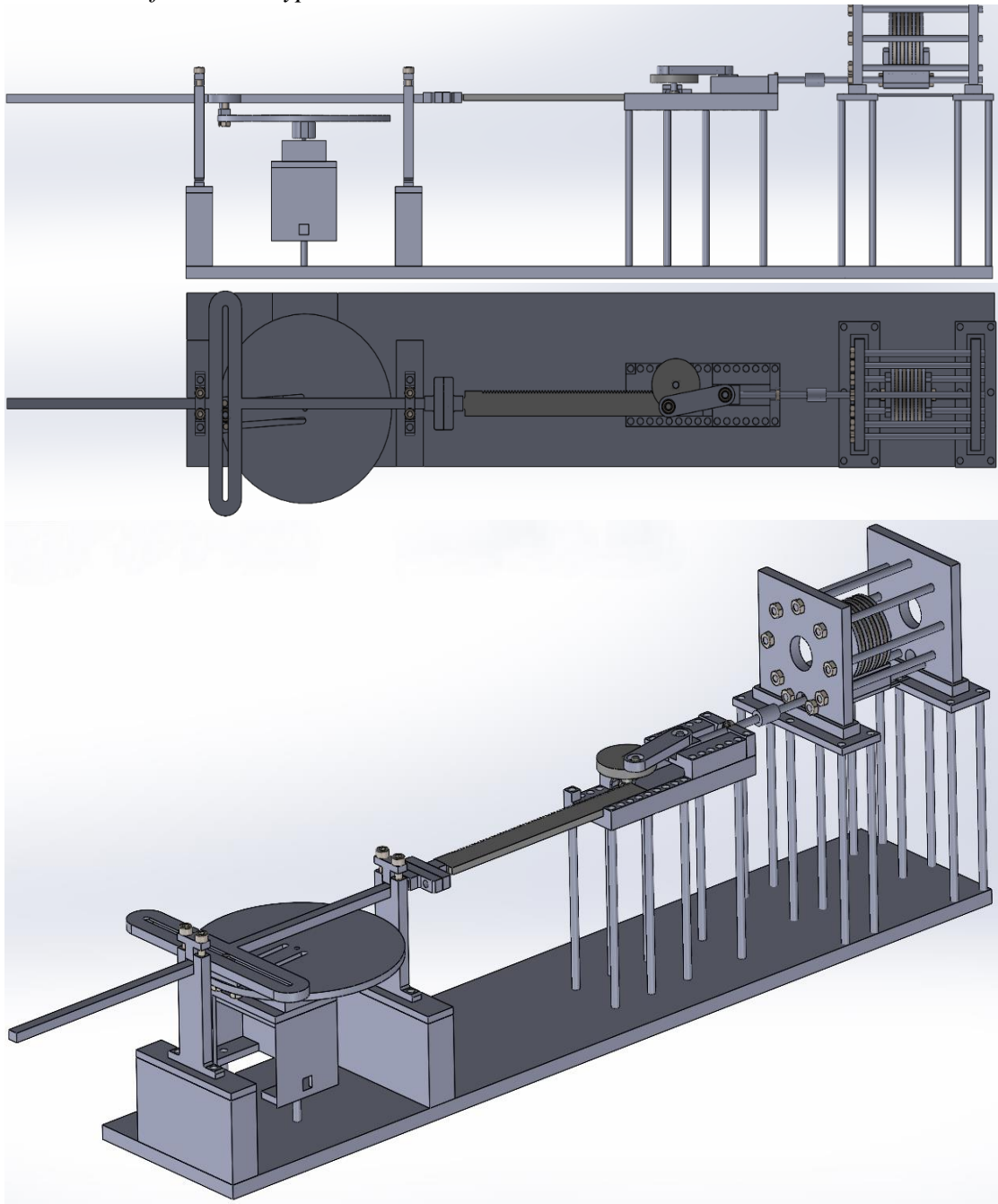


3.3.4 Final Assembly

The final assembly of the system is shown by Figure 3.17. The base area on which the system is assembled is 420 mm long and 83 mm wide.

Figure 3.17

Final CAD of the Prototype



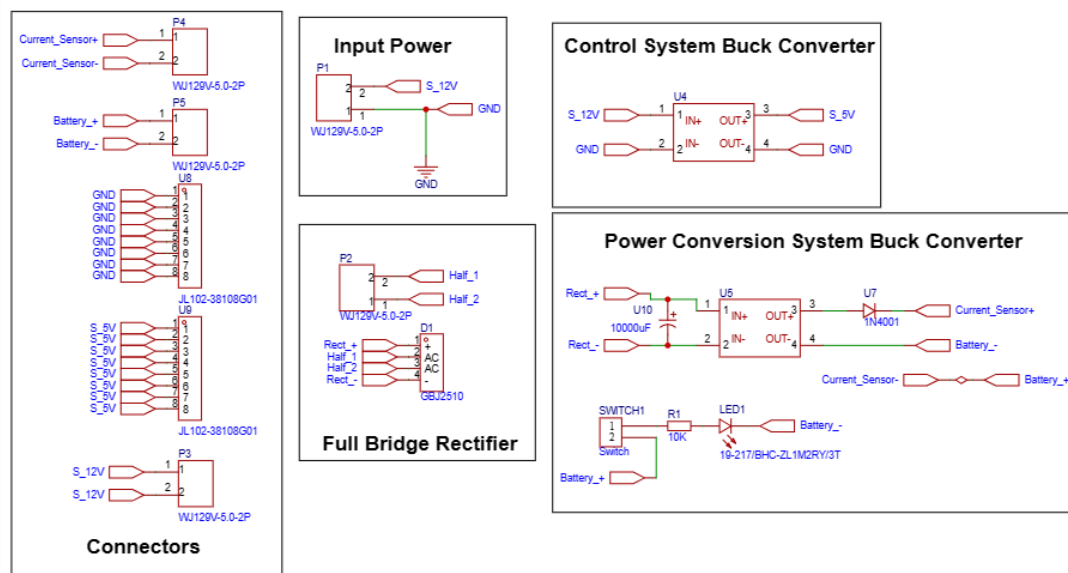
3.4 Circuit Board

The electrical board designed is used to achieve two main goals. They are, (1) controlling the frequency of the motor responsible for the input vibration and (2) receiving the power produced by the energy harvester and observing and harvesting that produced energy.

The schematic diagram and the PCB was designed using “easyEDA” software. It is an online circuit designing platform. As the frequency control of the input vibration motor was done with the help of an Arduino MEGA microcontroller, the PCB was designed mainly focusing on the 2nd goal, that is observing and harvesting the produced energy. The schematic diagram is shown by Figure 3.18. The designed PCB is shown by Figure 3.19 while the overall electrical wiring diagram of the control system was made using “fritzing” software and is shown by Figure 3.20. As shown by Figure 3.18 and Figure 3.20, the system is powered using a 12V power supply and 2 peripheral connection joints are made if any 12V components are required to be powered up. The 12V is stepped down to 5V using a LM2596 Buck convertor and 8 connection joints are included. As shown by Figure 3.20, a 12V connection is used to supply power for the

Figure 3.18

Schematic Diagram of the Circuit



motor via a L298N motor driver while two 5V connections are used to supply reference voltage for the ACS712 Current sensor and 0-25V Voltage Sensor.

Figure 3.19

Designed PCB

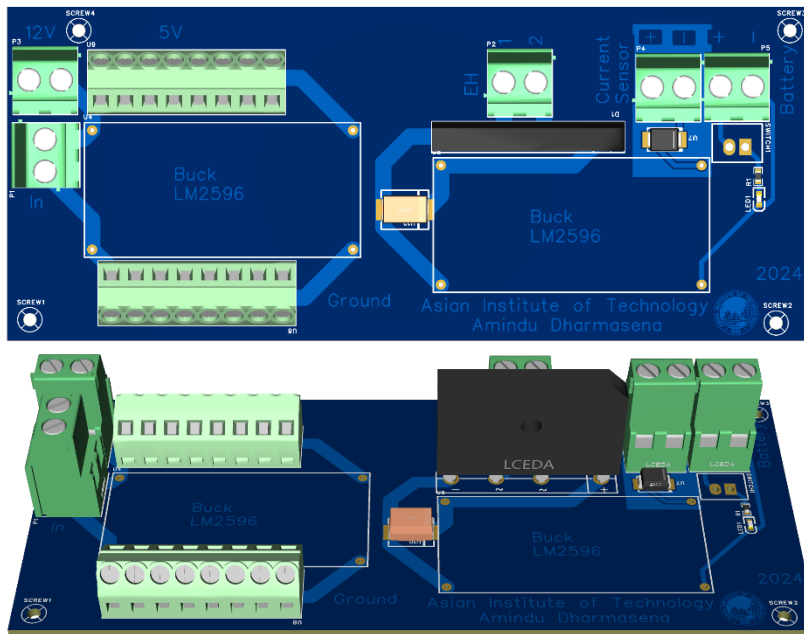
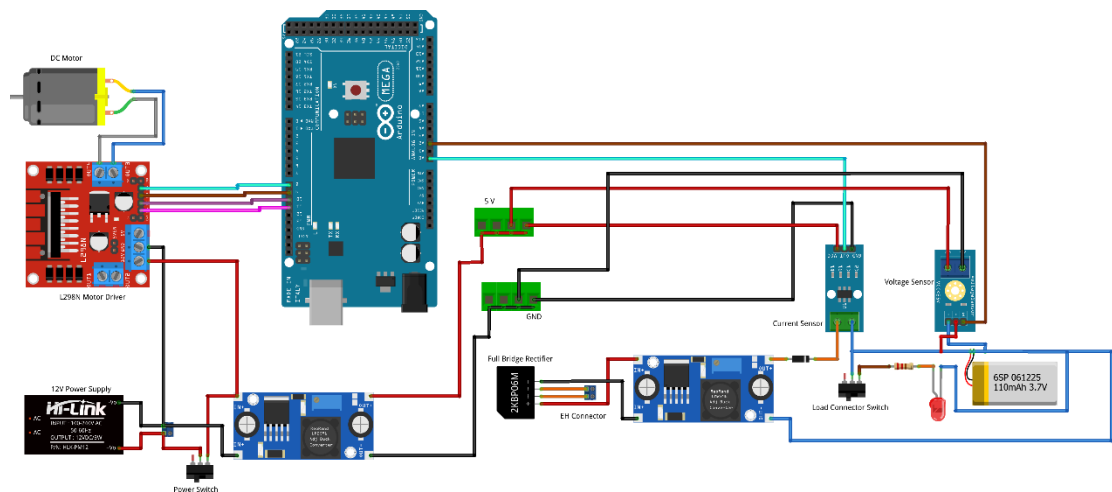


Figure 3.20

Electrical Wiring of the Control System



A 2-pin screw terminal is used to connect the two-coil winding ends of the Energy Harvester. The produced AC voltage is converted into DC with the help of 2KBP06M Full-Bridge Rectifier. The rectified voltage is fed through another LM2596 Buck convertor to step down the voltage to 3.7V and a 3.7V 50mAh LiPo battery is charged. A 1N4001 rectifier diode is connected in series after buck convertor to ensure one way energy transmission and the load can be enabled or disabled by the integrated switch. An LED is used as the load.

3.5 Fabrication

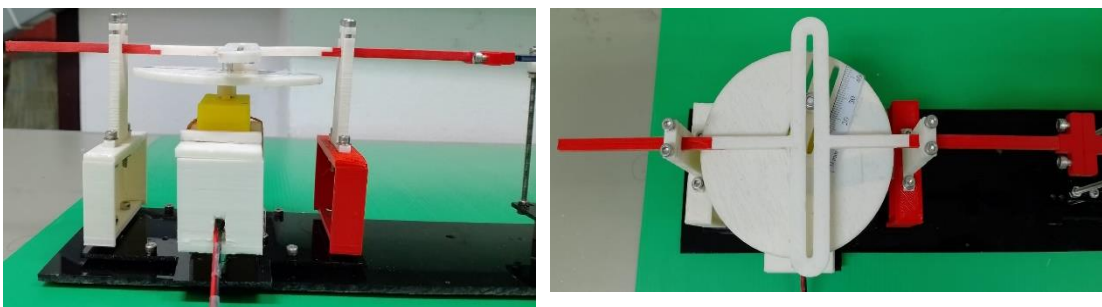
The designed parts of the CAD were fabricated by 3D printing. PLA was used as the material. The reasons for using PLA for fabrication were being inexpensive, not warping, being eco-friendly and non-toxic. All the different versions mentioned in Section 3.3 were fabricated and optimum versions were selected via trial and error. A major issue was shrinkage that occurred in 3D printed parts not being consistent as this caused uneven shrinkages in screw holes, guide rod holes, and caused changes in overall dimensions. This was tackled by changing the dimensions of separate parts individually to allocate tolerances and then fine tuning the dimensions using sandpaper and filing.

3.5.1 Input Vibration System

Input vibration system is shown by Figure 3.21. M3 screws and nuts were used to fasten the components and a 683ZZ ball bearing (3mm internal and 7mm outer diameters) was used to enable movement of the scotch-yoke guide rod.

Figure 3.21

Final Assembled Vibration System

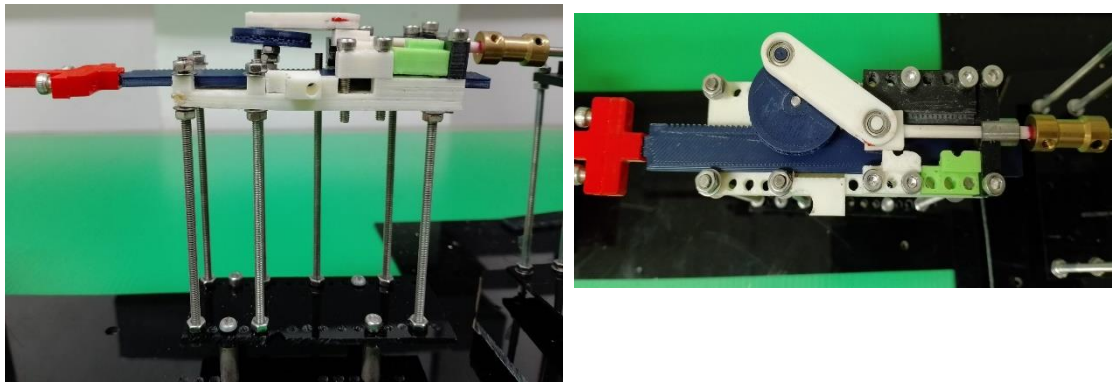


3.5.2 Mechanical Amplifier

The fabricated system is shown by Figure 3.22. M3 screws and nuts were used to fasten the components while M3 80mm studs were used to align the rack of the mechanical amplifier with the guide rod of the input vibration system. Two 683ZZ ball bearings and a LM3UU (3mm internal and 7mm external diameter) linear bearing was used enable smooth linear movement of the slider crank mechanism.

Figure 3.22

Final Assembled Mechanical Amplifier

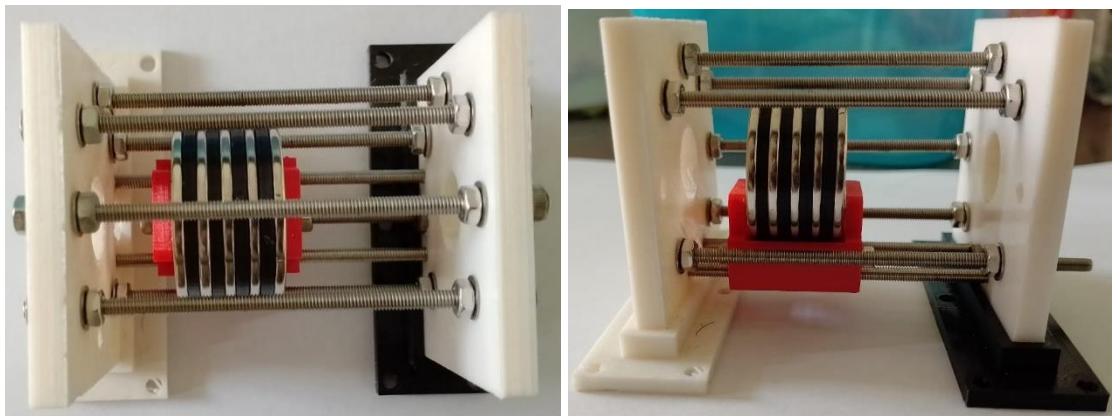


3.5.3 Energy Harvester

In the Energy Harvester, Neodymium Iron Boron (NdFeB) magnets with 3D printed spacers in-between was used as the moving mass. The coils were made using 30m of

Figure 3.23

Energy Harvester with Assembled Moving Mass



enameled copper wire with 0.4mm diameter. A spring was used as a stopper for the moving mass. The assembled moving mass and the coil windings are shown by Figure 3.23 and Figure 3.24 while the fully assembled system is shown by Figure 3.25.

Figure 3.24

Energy Harvester with Coil Windings

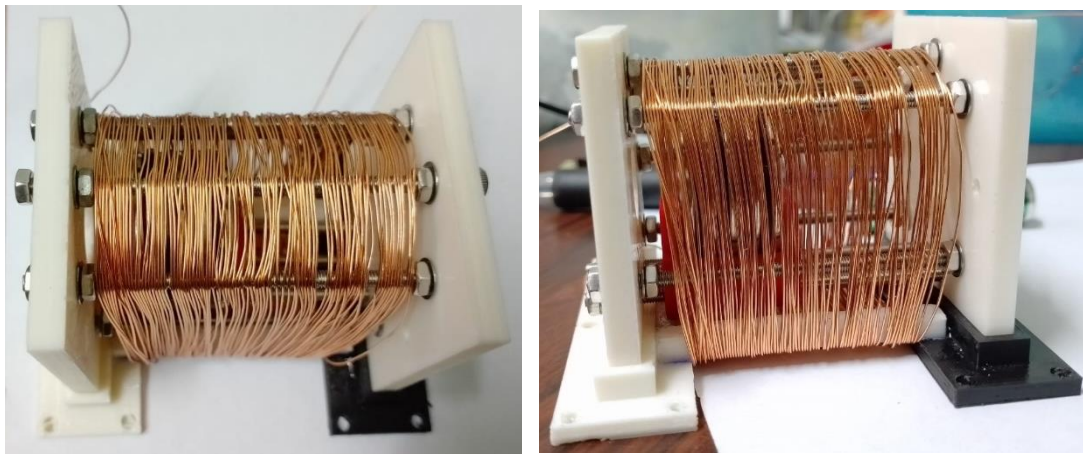
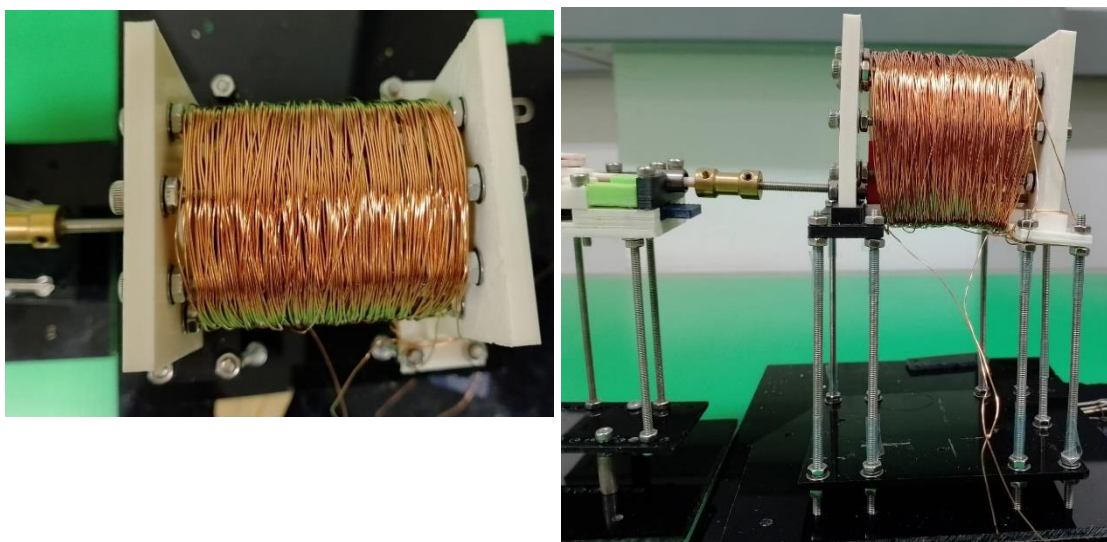


Figure 3.25

Final Assembled Energy Harvester



3.5.4 Full Fabrication

The base of the system was made using acrylic sheets. This is shown by Figure 3.26.

Figure 3.26

Cutting the Base using Acrylic Sheet

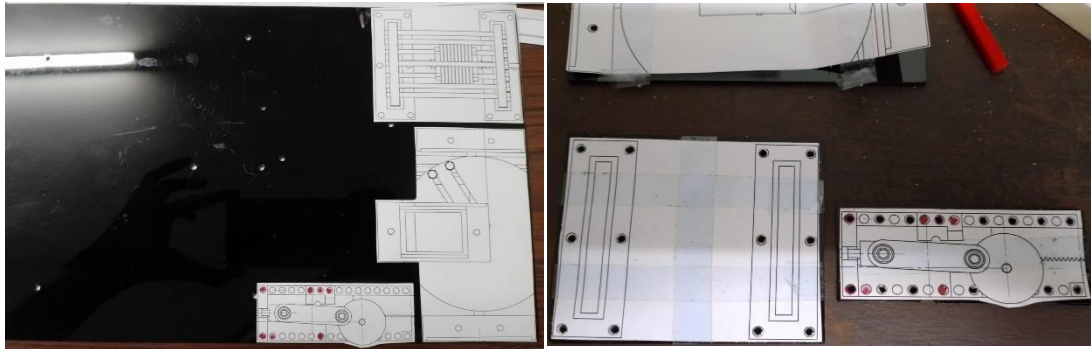
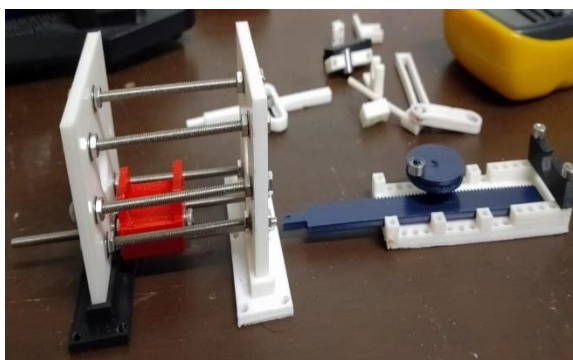
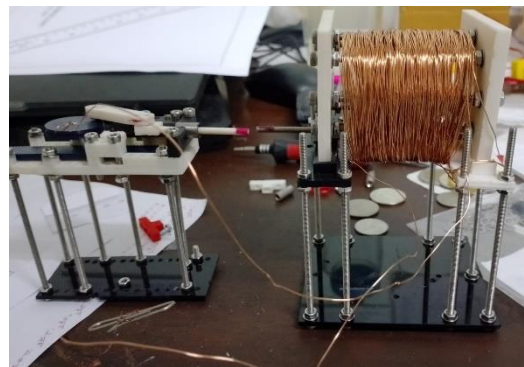


Figure 3.27

(a) Fabricated Parts, Height Alignment between (b) Mechanical Amplifier and Energy Harvester, (c) Input Vibration System and Mechanical Amplifier



(a)



(b)



(c)

Figure 3.27 and Figure 3.28 shows photos taken during the fabrication process and Figure 3.29 shows the fully fabricated system.

Figure 3.28

Test Fitting Components Together

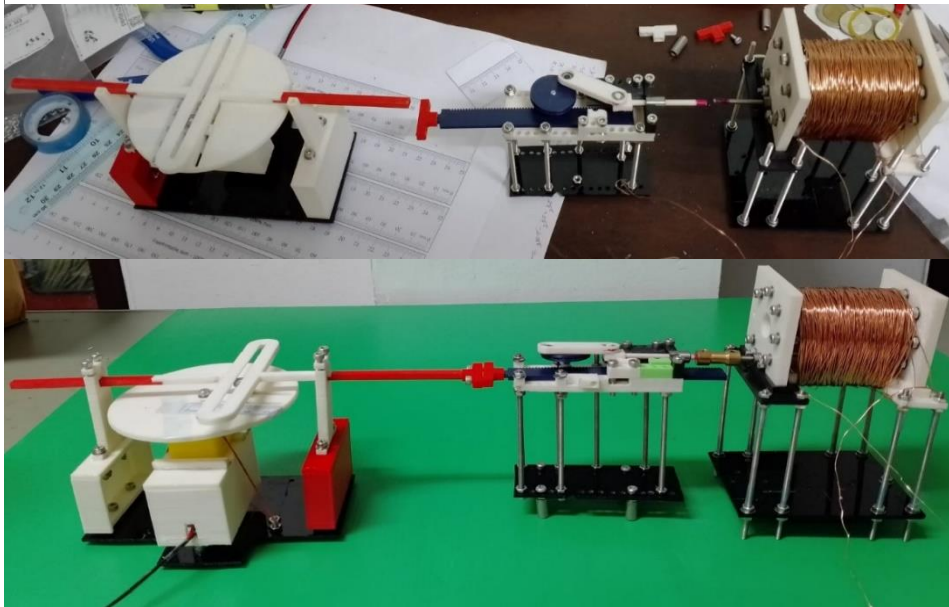
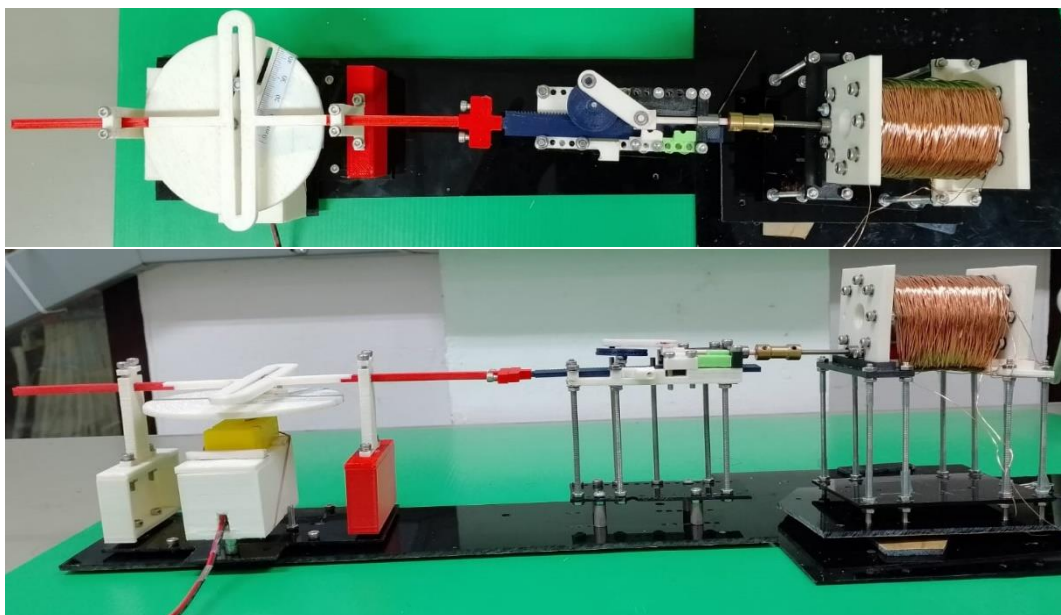


Figure 3.29

Final Fabricated System



3.5.5 Electrical System

The electrical system was fabricated with a dot board due to availability of components and time constraints.

Figure 3.30

Electrical Circuit during Fabrication

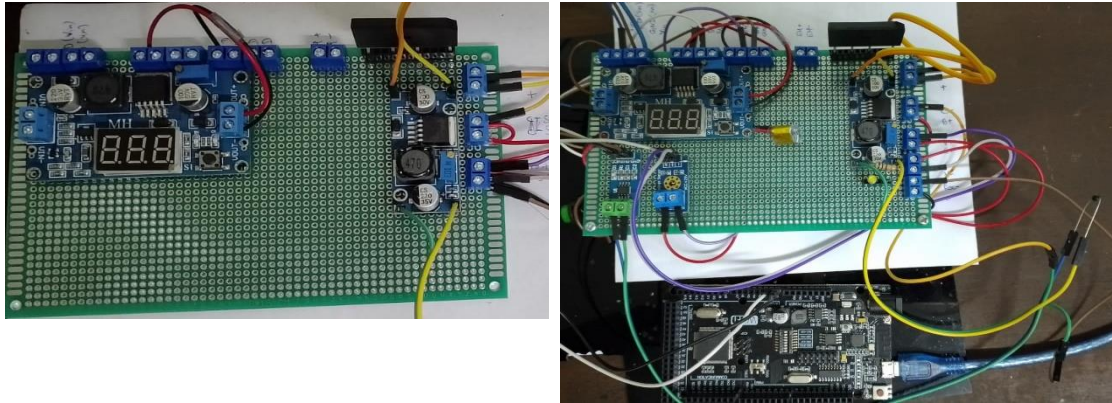
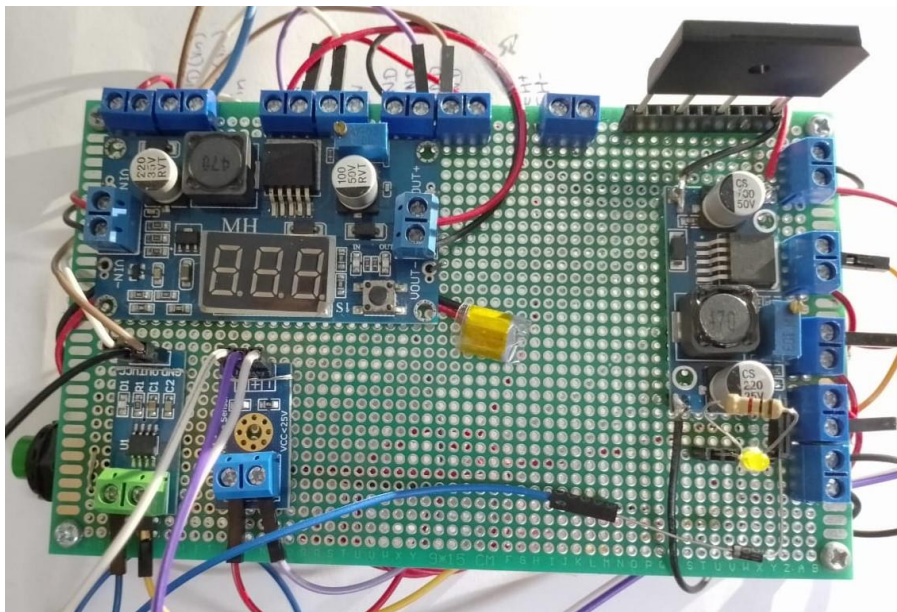


Figure 3.31

Fabricated Electrical Circuit



The mechanical, electrical and magnetic parameters of the fabricated system are tabulated in Table 3.1 and Table 3.2. These values were used for the simulations.

Table 3.1*Mechanical System Parameters*

Parameter	Value	Unit
Magnet diameter	30	mm
Magnet thickness	2	mm
Magnet Stroke	40	mm
Magnet Mass	141	g

Table 3.2*Electrical Circuit and Magnetic Parameters*

Parameter	Value	Unit
Coil mean diameter (2r)	0.4	mm
Coil resistance (R)	15.2	Ω
Coil length (l)	40	Mm
Number of turns per layer (N_l)	200	-
Number of coil layers (N_l)	1	-
Magnetic moment	1.2369	Am^2
(m) One magnet		
Total	6.1775	
Permeability of free space (μ_o)	1.256637061 μ	N/A ²

CHAPTER 4

RESULTS

This chapter consists of three subsections; for simulation results, for experimental results and for comparison between the simulation and experimental results.

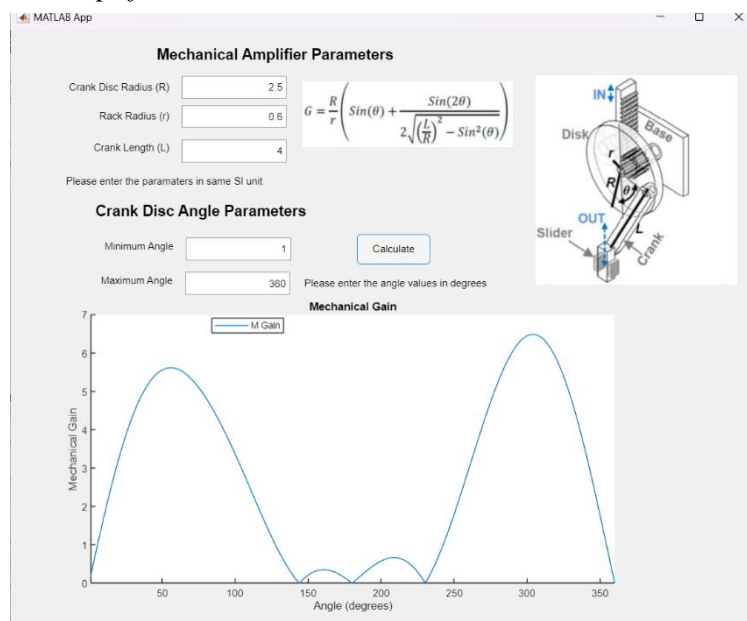
4.1 Simulation Results

4.1.1 Effect of Mechanical Amplifier on Input

The effect of the mechanical amplifier was examined initially before conducting the simulations. This was done by making a small app using MATLAB. The parameters entered and the plot depicting the effect of the amplifier is shown by Figure 4.1.

Figure 4.1

Mechanical Amplifier Simulation



The evaluation was done for a full revolution of the mechanical amplifier. The idea was to observe the effect of the disk-crank angle (Figure 2.19 (d)) have on the magnification. By observing Figure 4.1 and Figure 4.2, it can be observed that the amplifier has the possibility of negatively impacting the input during certain disk-crank angles (magnification becomes less than 1).

Figure 4.2

Polar Representation of the Magnification Effect

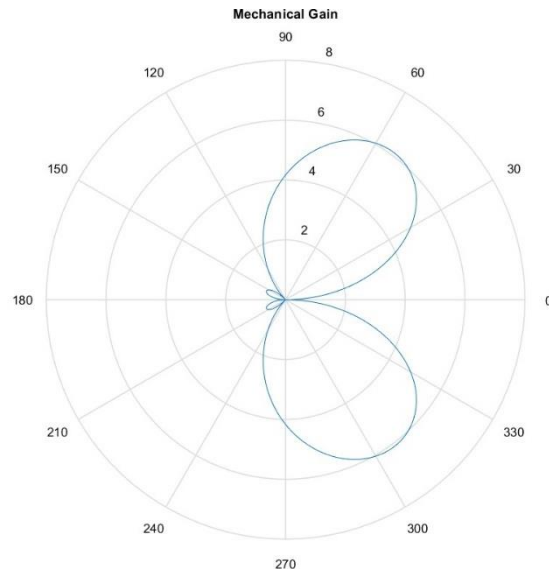


Table 4.1

Magnification Gain Breakdown of the Mechanical Amplifier

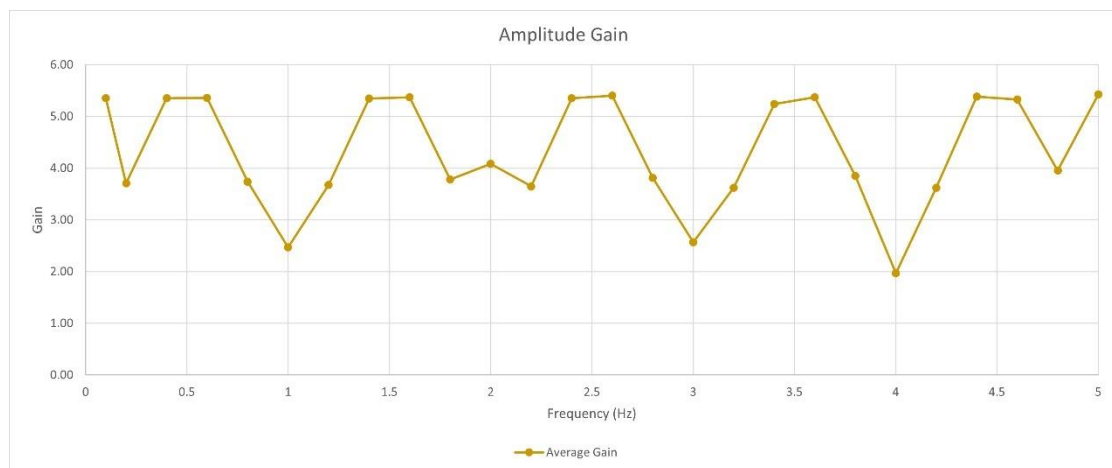
Magnification	Angle (°)
0 - 1	0 - 5, 122 - 238, 355 - 360
1 - 2	6 - 10, 112 - 121, 239 - 248, 350 - 354
2 - 3	11 - 16, 103 - 111, 249 - 257, 344 - 349
3 - 4	17 - 23, 92 - 102, 258 - 268, 337 - 343
4 - 5	24 - 31, 81 - 91, 269 - 279, 329 - 336
5 - 6	32 - 46, 62 - 80, 280 - 298, 314 - 328
6 - 7	47 - 61, 299 - 313

Table 4.1 provides the breakdown of the gain corresponding to the disk-crank angle. The highest gain is 6.11 and it is achieved at 2 angle values, at 54° and at 306° . By ensuring the disk-crank angle is kept between either $6^\circ - 121^\circ$ or $239^\circ - 354^\circ$, an amplifying effect on the input can be achieved. A full revolution provides an average magnification gain of 2.88.

When the system shown by Figure 3.3 was simulated, a unique pattern for the system input was observed. For all of the amplitude values and majority of frequency values (except 1, 2, 3, 4, 5 Hz), the magnification factor of the input was same. The detailed values are shown in APPENDIX A. These values indicate that the input amplitude doesn't have an impact on the gain and the gain is dependent on the input frequency. Figure 4.3 depicts the average gain for different frequencies and it can be noted that for all the frequencies of the experiment, the implemented mechanical amplifier has managed to enhance the input. This validates the notion that mechanical amplifiers are suitable to enhance low frequency inputs.

Figure 4.3

Input Gain vs Frequency Plot



4.1.2 Generated Voltage on Simulation

During the simulation, the average voltage value was taken into consideration. As shown by Figure 4.4, the generated voltage gets increased when the amplitude and frequency gets higher in both system simulations; with amplifier and without amplifier. In the system with the amplifier, highest voltage of 140.36 mV is generated at an amplitude of 32mm and frequency of 4.8 Hz. 72.22 mV is the highest voltage generated when the system doesn't have the amplifier, at that value is obtained at an amplitude of 40mm and frequency of 5.0 Hz. Figure 4.5 depicts the voltage gain corresponding to different amplitude ranges and the effect on low amplitude and frequency settings can be clearly seen. Table 4.2 provides the breakdown of the average voltage gain based on **Figure 4.4**

Generated Voltage (Top) with Amplification, and (Bottom) without Amplification



amplitude and frequency ranges. This is a very good indicator that the amplifier is useful in enhancing low amplitude and low frequency input vibrations.

Figure 4.5

Voltage Magnitude Gain for Different Amplitude Ranges

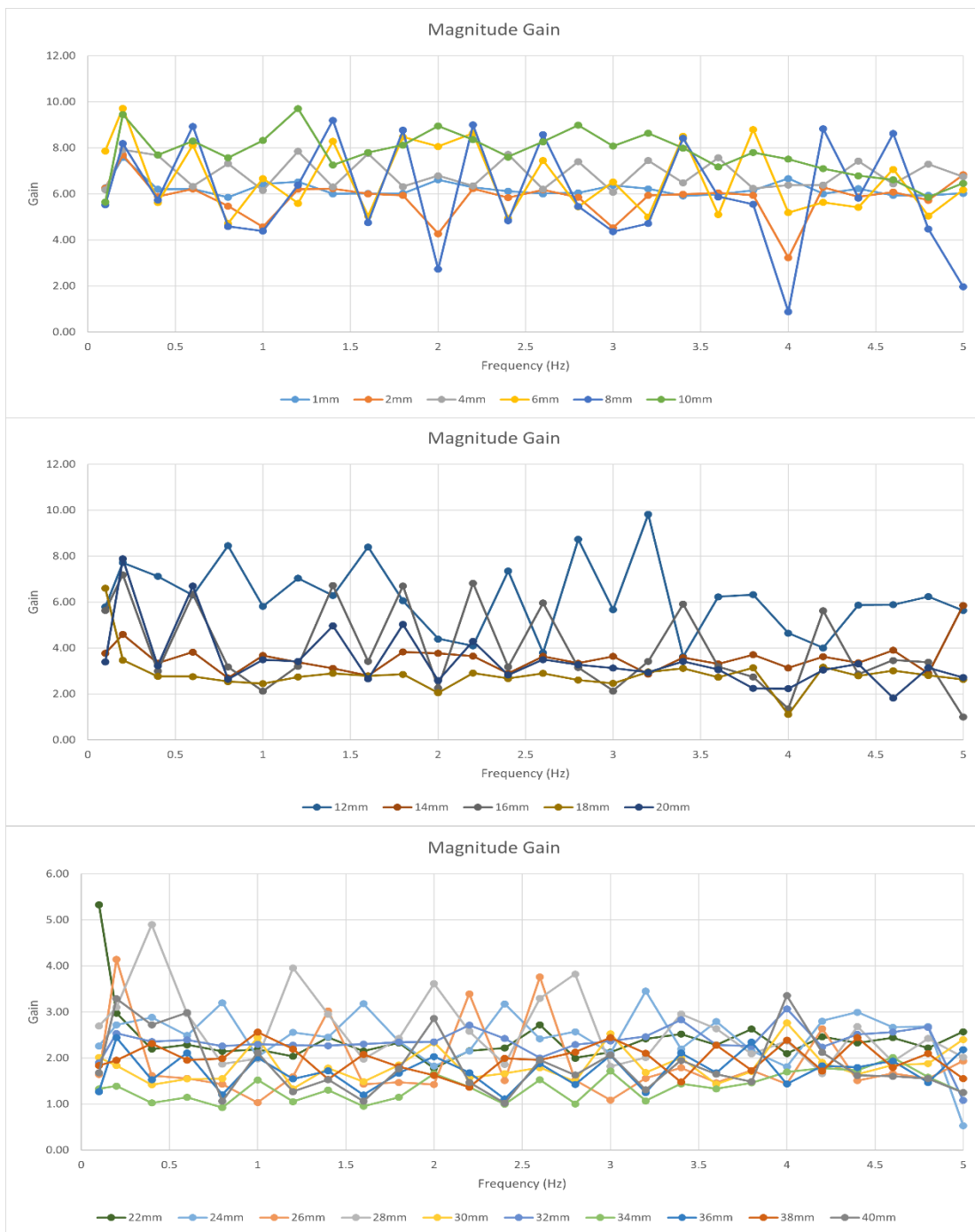


Table 4.2*Simulated Voltage Gain Breakdown Based on Amplitude and Frequency*

Amplitude Range (mm)	Average Amplification	Frequency Range (Hz)	Average Amplification
0 – 10	6.56	0 – 1	4.07
12 – 20	4.03	1.2 – 2	3.87
22 – 30	2.25	2.2 – 3	3.81
32 – 40	1.86	3.2 – 4	3.64
		4.2 – 5	3.61

Even though the amplification is considerably good for all ranges of amplitudes and frequencies, the optimum range is when the amplitude is in the range of 0 – 10mm and frequency in the range of 0 – 3 Hz.

4.1.3 Generated Power on Simulation

The power calculations were done using the generated voltage values. As was the previous case and by observing Figure 4.6, it can be determined that the generated power is increased with the increase of amplitude and frequency. In the system with amplification, the highest power generation has occurred at an amplitude of 32mm and at a frequency of 4.8 Hz while in the system without the amplification, the highest power generation is at an amplitude of 40mm and at a frequency of 5 Hz. The generated power values are 1296 μ W and 343 μ W respectively. When considering the effect of amplification imparted to the system by the mechanical amplifier, it is noticed that the amplifier is beneficial for low amplitude (less than 10mm) and low frequency (0 – 3Hz) applications. This can be determined by referring Table 4.3 and Figure 4.7.

Figure 4.6

Generated Power during Simulations

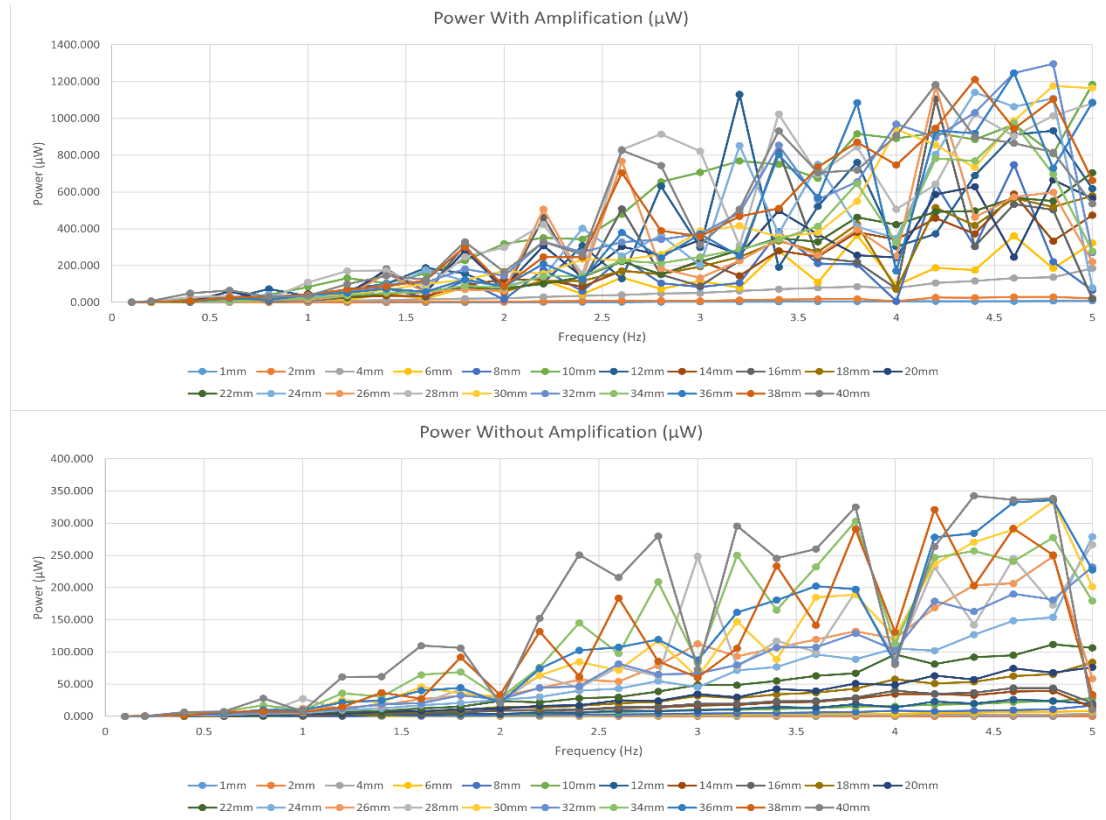


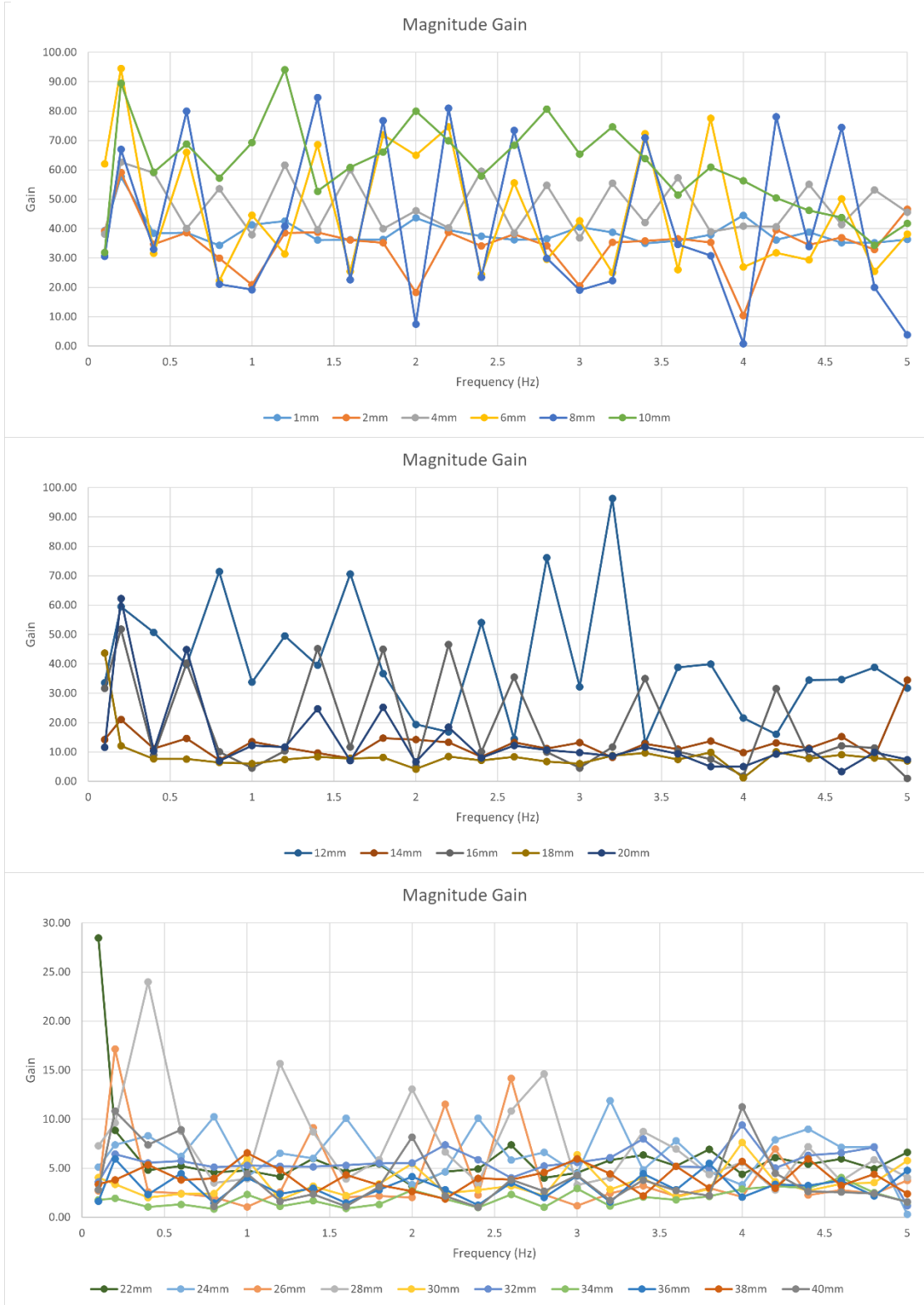
Table 4.3

Power Amplification Breakdown Based on Amplitude and Frequency

Amplitude Range (mm)	Average Amplification	Frequency Range (Hz)	Average Amplification
0 – 10	45.08	0 – 1	22.12
12 – 20	19.24	1.2 – 2	20.74
22 – 30	5.61	2.2 – 3	19.69
32 – 40	3.72	3.2 – 4	18.17
		4.2 – 5	17.20

Figure 4.7

Power Amplification Breakdown for Amplitude Ranges

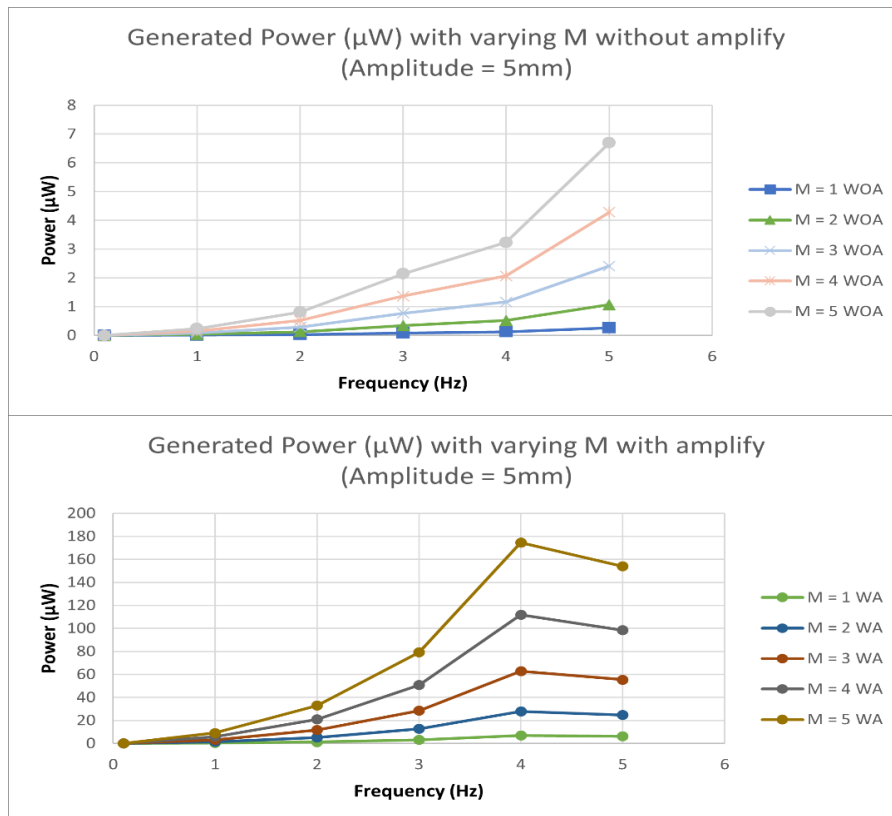


4.1.4 Effect of Magnetic Moment on Output Power

As the name implies, electromagnetic energy harvesters are dependent on the magnetic moment the system possesses. Having a higher magnetic moment result in generating a higher power. This is confirmed by equations (32) and (34) mentioned in the methodology. Few tests were conducted to determine the effect of magnetic moment on power generation. The “M” value shown in Figure 4.8 means the number of magnets that were used. As the moving mass was made using 5 magnets, the system was also modelled to mimic the usage of 5 magnets. In the legend of the graph, “WOA” implies without amplifier while “WA” implies with amplification. As shown in Figure 4.8, the generated power increases with the increase of magnetic moment. This proves the validity of the equations (32) and (34). Increasing the number of magnets will result in an increase of the weight of the system. So, the supporting elements of the system should be determined accordingly

Figure 4.8

Power Generation with Varying Magnetic Moment

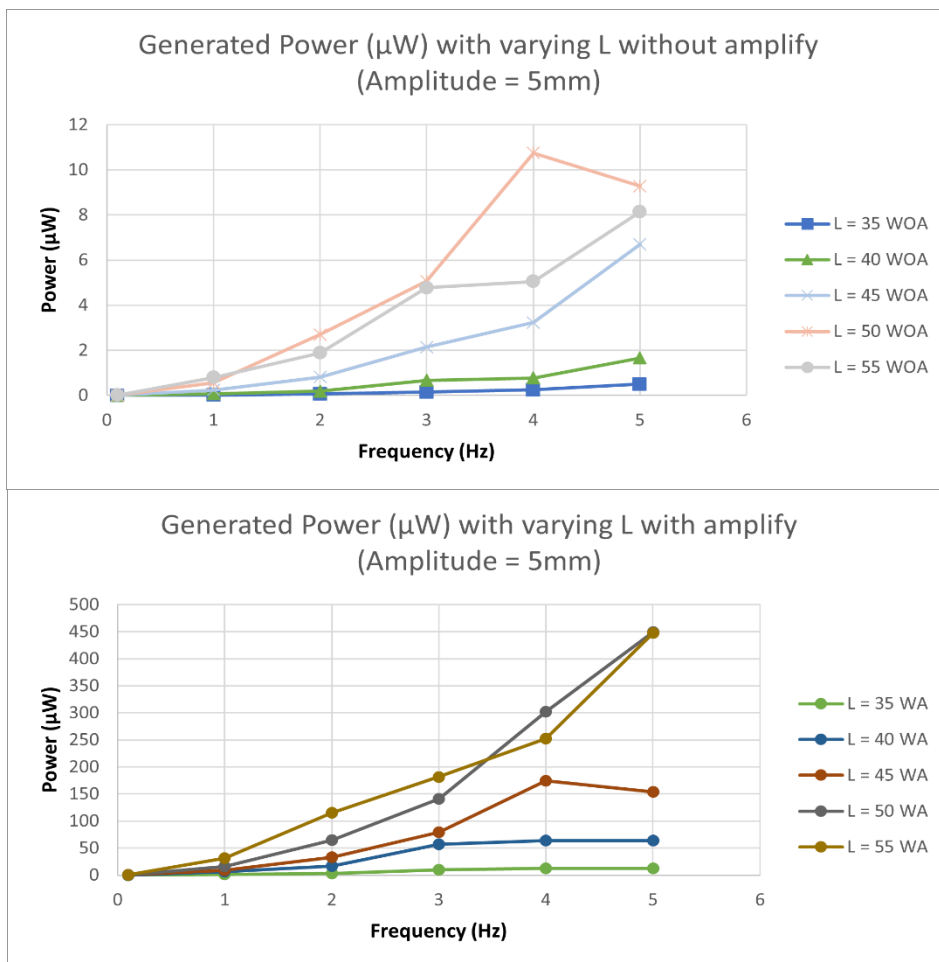


4.1.5 Effect of Coil Length on Output Power

When considering the equation (35) mentioned in the methodology, an increase of coil length results in an increase in relative distance from magnets' dipole center. This should ultimately increase the generated power. As shown in Figure 4.9, the generated power is increasing with the increase of the coil length, thus proving our initial argument made in equation (35). The "WOA" in the legend of the graph stands for without amplifier while "WA" implies with amplifier. It should be noted that the increase of coil length results in lengthening the energy harvester which would make the system bulkier. So, the coil length should be decided according to the requirements of the application.

Figure 4.9

Power Generation with Varying Coil Length



4.2 Experimental Results

The fabricated system was tested for multiple amplitude and frequency combinations. The voltage value was obtained using an Oscilloscope and this value was used for the relevant power calculations. Few issues arose during the experimentation process. Considering the time constraints, only temporary solutions were implemented so that the experiments could be carried out. When testing for frequencies below 0.8 Hz, the movement of the system was erratic and when the frequency was above 3 Hz, the system was swaying considerably and some parts of the system ended up getting snapped (Figure 4.10 (Right)).

By loosening few screws in link-holders to allow components to slide off instead of snapping, by reducing the testing time to 2 seconds to mimic an impact input and to reduce the strain imparted on the system, and by reinforcing the sides of the energy harvester base to reduce swaying; the issues were mitigated significantly and system was able to take readings up to 4.6 Hz. Experimental readings for the frequency ranging from 0.8 Hz to 4.6 Hz was obtained.

4.2.1 Generated Voltage during Experimentation

Figure 4.10

(Left) During Testing and (Right) Link Connecting the Scotch-Yoke Mechanism to Amplifier being Snapped

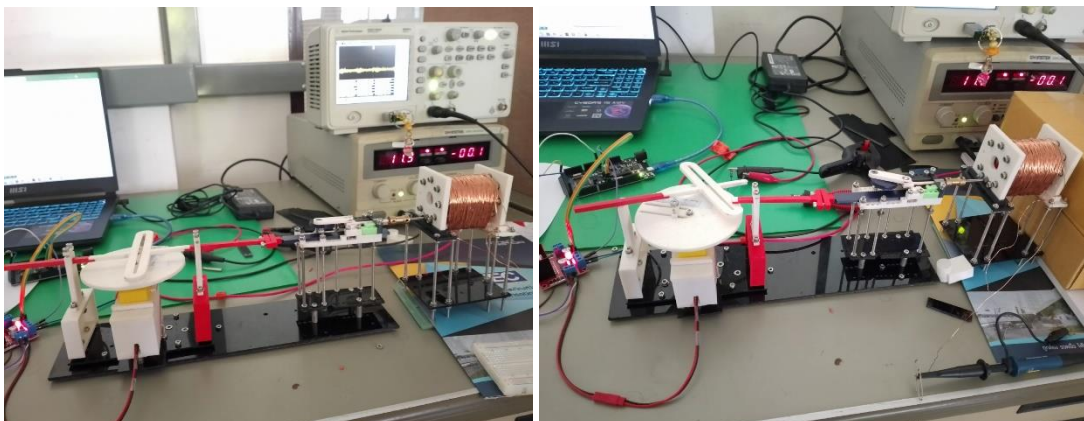


Figure 4.11 shows the generated voltage by the experimental rig. When considering the system with amplification the maximum voltage generated is 59 mV at amplitude and frequency of 10mm and 2.8 Hz respectively. In the system without amplification, the maximum generated voltage is 40 mV at an amplitude and frequency of 30mm and 2.8 Hz respectively. When considering the magnitude gain (Figure 4.12), the magnification factor is larger at lower amplitudes than that of at higher amplitudes. For amplitudes less than 6mm, the magnification factor is between 5 – 12.9 for all frequencies. For inputs of amplitude between 6mm – 16mm the amplification factor is between 2 – 5 for all frequencies. The same can be said for systems with amplitude between 32mm – 40mm, but the magnification factor drops to a range of 1 – 2 for frequencies less than 1.2 Hz. The systems with input amplitude between 16mm – 32mm have a magnification factor between 1 – 3.5 for all frequencies. Table 4.4 shows the average amplification

Figure 4.11

Generated Voltage during Experimentation

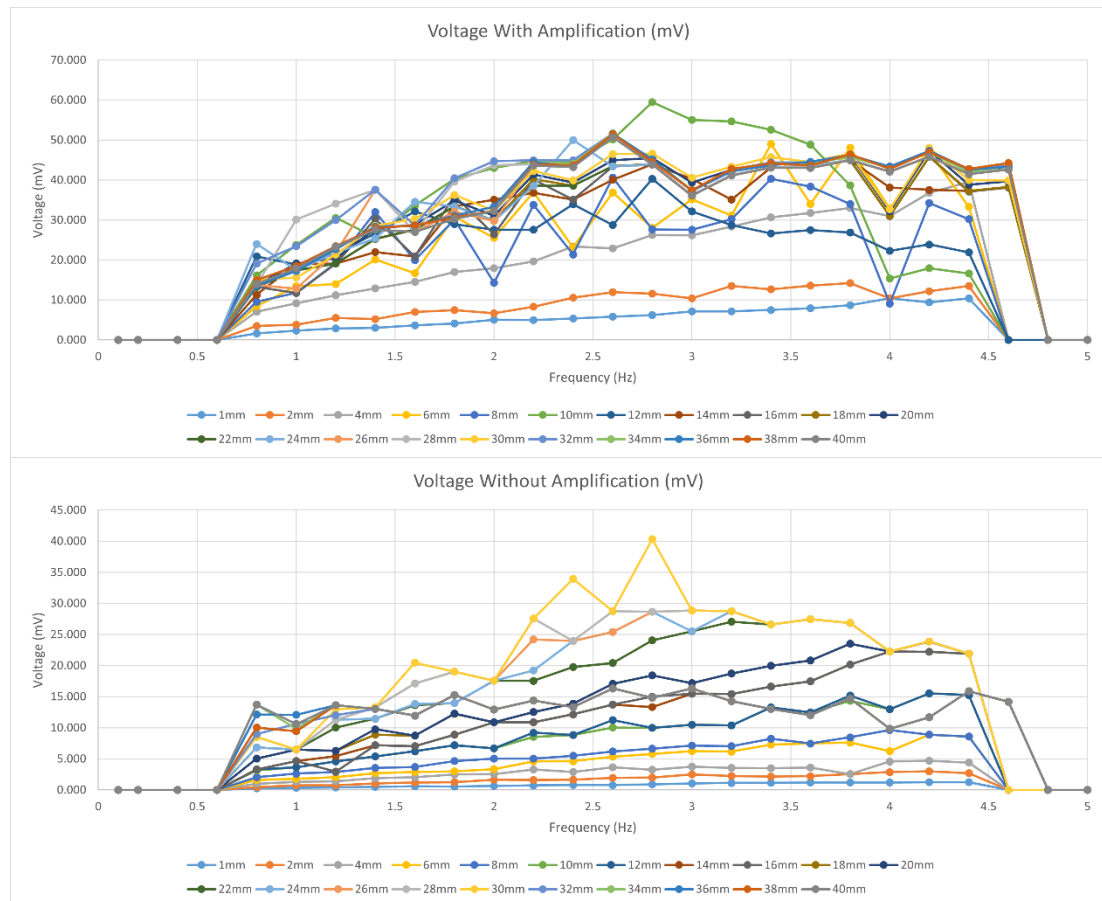
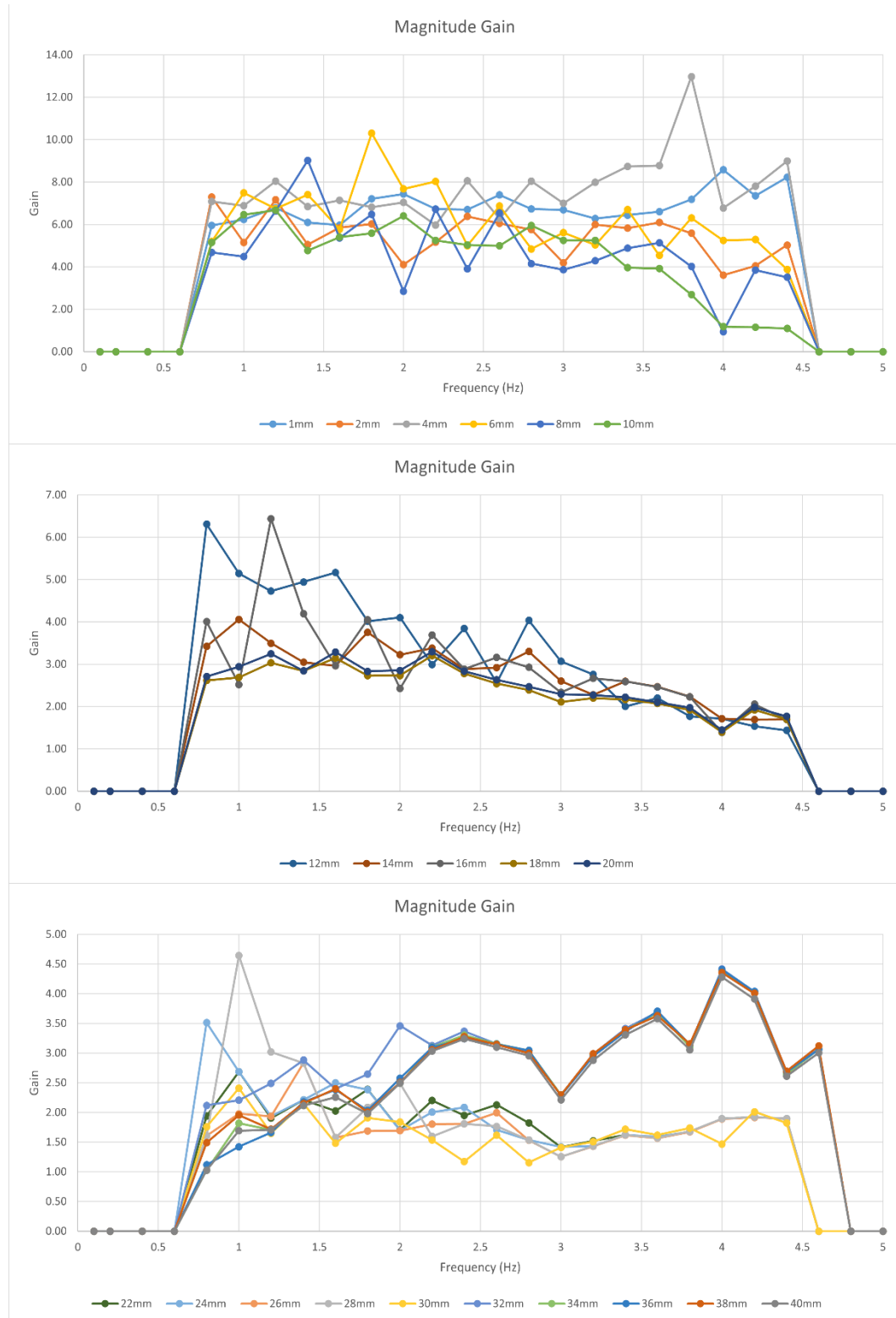


Figure 4.12

Voltage Amplification Breakdown for Amplitude Ranges



for different amplitude and frequency ranges. The results imply that the designed system is suitable to enhance low amplitude and low frequency inputs. Overall, we can say that there is a positive impact from the mechanical amplifier as the comparison between the two systems reveal a considerable magnification for all the frequencies.

Table 4.4

Experimental Voltage Gain Breakdown Based on Amplitude and Frequency

Amplitude Range (mm)	Average Amplification	Frequency Range (Hz)	Average Amplification
0 – 10	5.94	0 – 1	3.55
12 – 20	2.83	1.2 – 2	3.73
22 – 30	1.87	2.2 – 3	3.50
32 – 40	2.81	3.2 – 4	3.36
		4.2 – 5	3.10

4.2.2 Generated Power during Experimentation

In the system with amplification, the highest power which is 233 μW is generated at 10mm and 2.8Hz configuration. In the system without amplifier, the maximum generated power is 106 μW at 30mm and 2.8Hz configuration (Figure 4.13). When looking at the amplification factor within these two systems, the values are amplified throughout the amplitude and frequency range. It is implied by the magnification gain of the system (Figure 4.14). For inputs of amplitude between 1mm – 6mm, the magnification ranges from 35- 73 for all frequencies while it is between 5 to 16 for amplitudes of 6mm – 16mm. Magnification drops to a range of 1 – 9 for input amplitudes of 16mm – 32mm. In the amplitude range 32mm – 40mm, the magnification is between 5 – 16 for frequencies greater than 1.2 Hz while it is between 1 – 5 for frequencies less than 1.2 Hz. Table 4.5 shows the average magnification breakdown for different amplitude and frequency ranges.

Figure 4.13

Generated Power during Experimentation

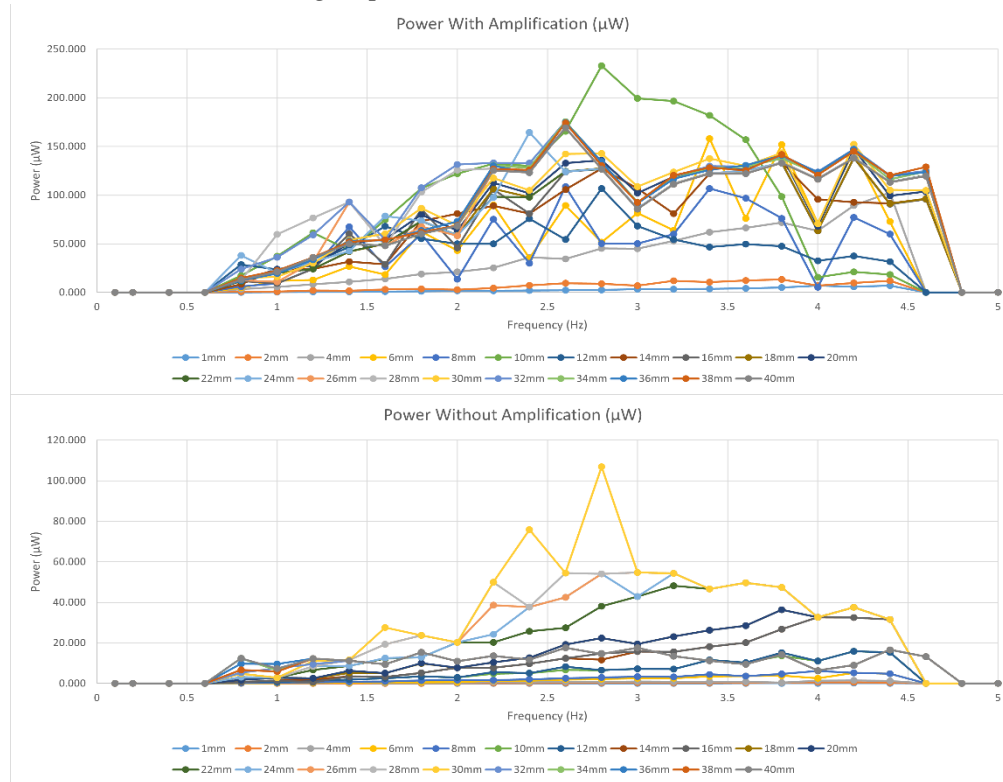


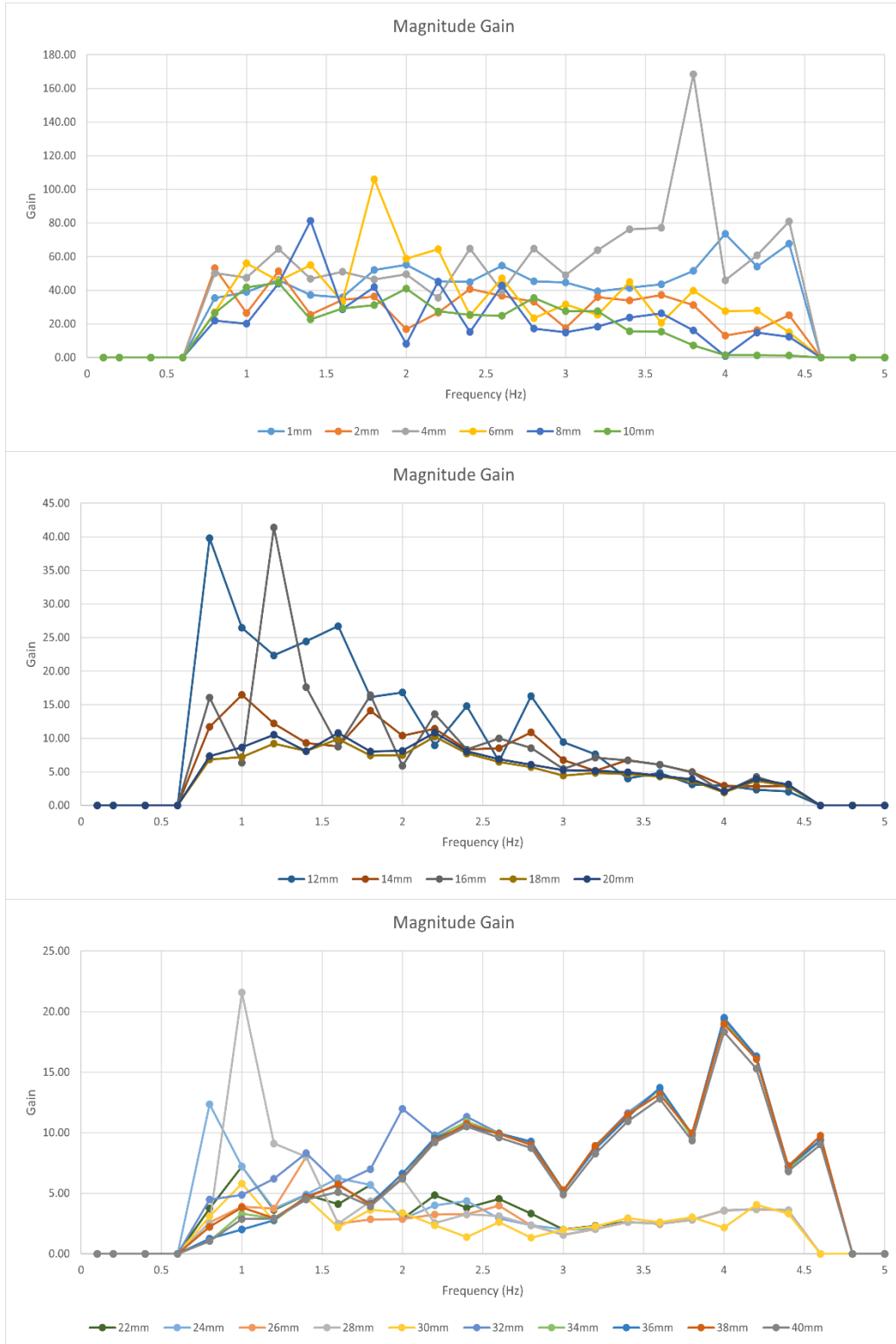
Table 4.5

Experimental Power Gain Breakdown Based on Amplitude and Frequency

Amplitude Range (mm)	Average Amplification	Frequency Range (Hz)	Average Amplification
0 – 10	38.58	0 – 1	16.41
12 – 20	8.97	1.2 – 2	18.12
22 – 30	3.75	2.2 – 3	15.47
32 – 40	8.51	3.2 – 4	15.60
		4.2 – 5	13.36

Figure 4.14

Power Amplification Breakdown for Amplitude Ranges



By examining these values, it can be determined that the implemented system is preferable to be used to amplify low amplitude, low frequency vibrations.

4.3 Comparison between Simulation and Experimental Results

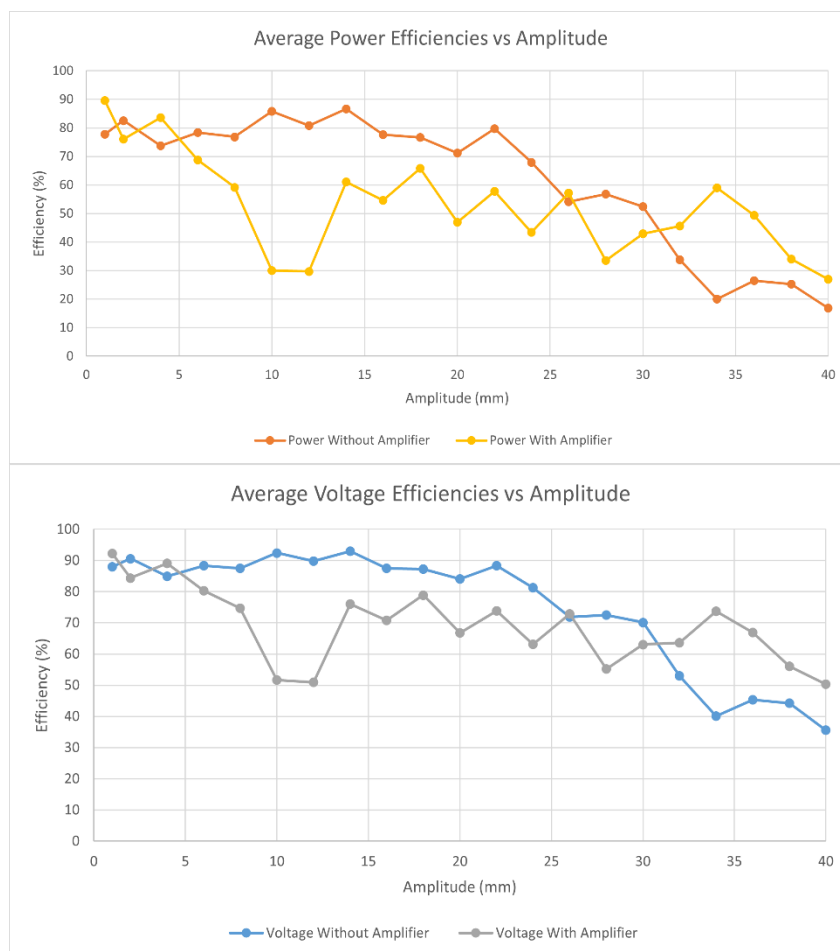
The experimental and simulation results were compared to determine the accuracy of each system. The comparison was done with regard to amplitude and frequency.

4.3.1 Comparison According to Amplitude

By referring the relevant data are shown in Figure 4.15, it can be determined that the efficiency of the physical system was fairly high when compared with the simulated

Figure 4.15

(Top) Average Power, and (Bottom) Average Voltage Efficiencies with Respect to Amplitude

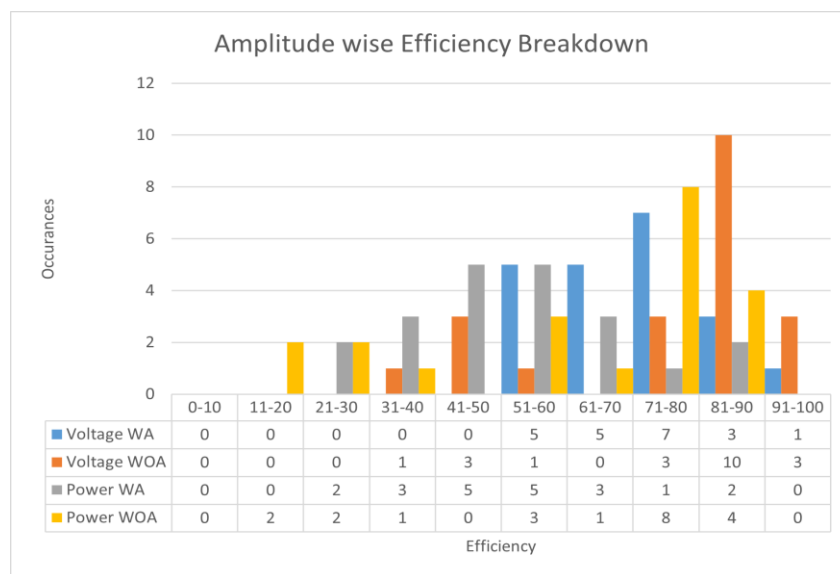


system. When considering the power of the system without the amplifier, the efficiency is above 60% until the amplitude reaches 25mm and then it hovers between 50% – 60% until amplitude becomes 30mm. Then the efficiency drop that happens is pretty steep as it falls to 16% by the time amplitude becomes 40mm. The same trend can be seen in the system with the amplifier albeit the efficiency values being lower. The efficiency value is higher when the amplitude is low and it gradually decreases as the amplitude increases. The reason for the reduced efficiency values of the system with the amplifier could be due to addition of the mechanical amplifier, as it has moving parts which can hinder the energy conversion process due to friction.

The voltage efficiency plots for systems with amplifier and without amplifier follow the same pattern of that of the power plot because of the relationship between voltage and power (Equation (37)). Figure 4.16 shows the efficiency breakdown to according to few ranges to provide more detailed information about the system. The “WA” stands for “With Amplifier” while “WOA” stands for “Without Amplifier”. The majority of the tested instances fall above 60% efficiency which is encouraging.

Figure 4.16

Amplitude wise Efficiency Breakdown



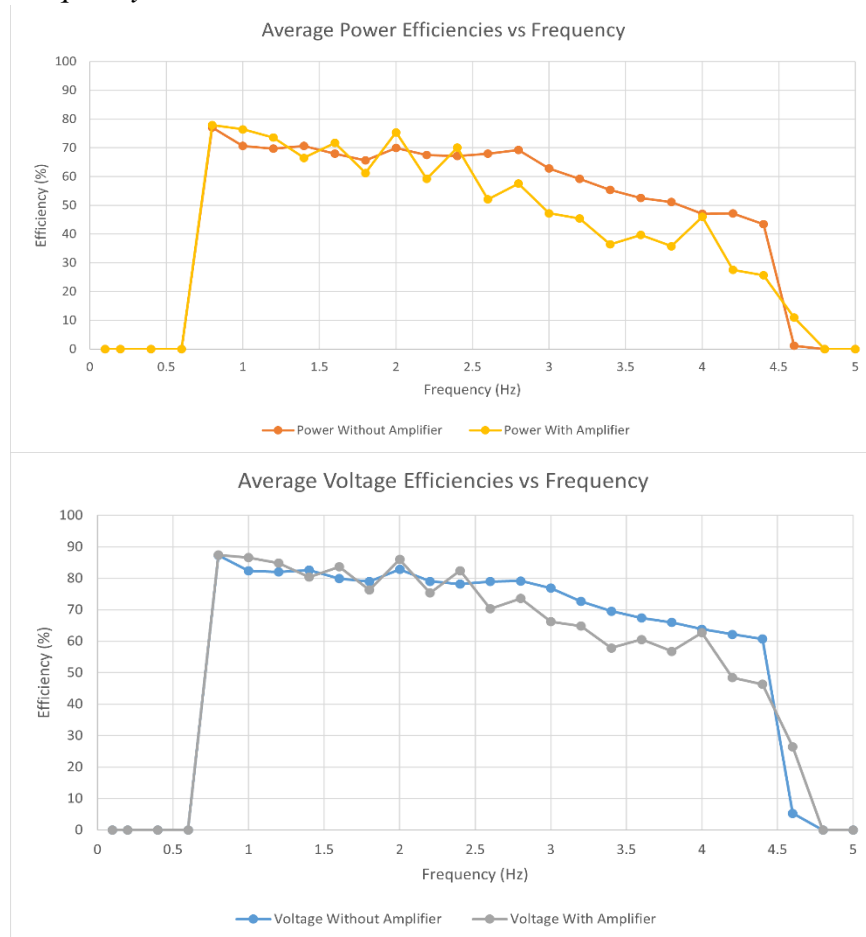
4.3.2 Comparison According to Frequency

Figure 4.17 shows the evaluated voltage, power efficiency data with respect to frequency and a detailed breakdown of the obtained efficiency values. It must be noted that values up to 0.6 Hz and values from 4.8 Hz up to 5 Hz are zero because the system was not tested for those frequency values. The reason for that decision is described previously on “4.2 Experimental Results”. These zero values are easily recognized in the efficiency breakdown.

When considering the generated power of the system without the amplifier, the efficiency stays above 60% until 3 Hz and then it stays between 50% - 60% until frequency is 3.8 Hz. Then a slight drop can be seen and the value becomes 43% for the

Figure 4.17

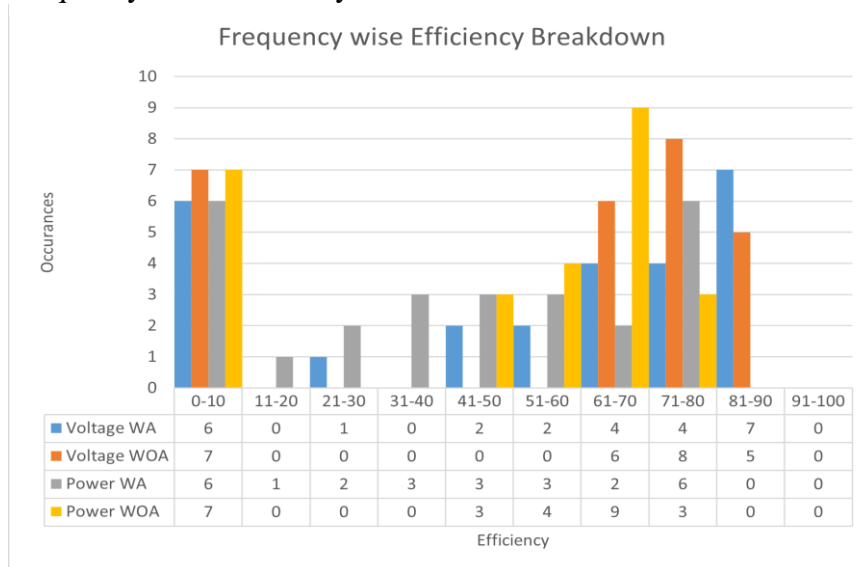
(Top) Average Power, (Bottom) Average Voltage Efficiencies with Respect to Frequency



frequency setting of 4.6 Hz. For the system with the amplifier, the voltage efficiency stays above 60% until 2 Hz and then it drifts between 45% - 60% till the frequency becomes 3.2 Hz. The frequency follows a decreasing sawtooth pattern and finally reaches 11% at 4.6 Hz. The reason for this efficiency discrepancy can be the additional frictional loss that occurs in the energy conversion process due to the inclusion of the mechanical amplifier. The voltage efficiency curves follow the same trend as that of power efficiency curves with an overall efficiency increase of about 10%. The six frequency settings (0.1 Hz, 0.2 Hz, 0.4Hz, 0.6 Hz, 4.8 Hz, 5.0 Hz) excluded during the experimental phase is clearly visible in the efficiency breakdown graph in Figure 4.17. When considering with respect to frequency, more than half the efficiency values are above 60% and the majority of the efficiency values are over 40% which is promising as this implies the outputs of the physical system and simulated system are accurate.

Figure 4.18

Frequency wise Efficiency Breakdown



As the simulation model was made considering lossless energy conversion, it was taken as the experimental values which has a 100% efficiency value. Considering the efficiency values that were obtained from the experiments and which were compared above according to the amplitude and frequency, it can be noted that the requirement of building a system which has an efficiency greater than 40% is achieved.

CHAPTER 5

CONCLUSION

This chapter will provide a final conclusion about the results mentioned in above chapter and recommendations to improve the system.

5.1 Conclusion

The aim of this thesis was to design and develop a free-impact motion type vibration energy harvester which is incorporated with an amplitude magnification mechanism to increase the power for a wider operating frequency. Objectives 1 and 3 were related to the designing, fabricating and testing the physical system. Objective 2 was about the simulation aspect while Objective 4 was about efficiency of the system. By considering the results obtained, it can be stated that the objectives of the thesis were fulfilled while adhering to the stated scope and limitations.

The physically implemented system was capable of working in the broad frequency range of 0.8 Hz – 4.6 Hz and managed to maintain a higher efficiency value above 60% for majority of the tested scenarios for both amplitude and frequency. The system has exceeded the proposed scope of having an efficiency above 40%. Particularly the system has an efficiency value above 80% for low amplitude and low frequency input parameters which make this a perfect candidate to enhance low-frequency power harvesters. As discussed in the “Results” chapter, this efficiency can be increased by addressing the issues arose during physical testing in a permanent manner.

5.2 Recommendations

From the experience that was obtained during the theses work, following recommendations can be made regarding the work and regarding future focus areas for improvement.

1. Fabricate the system using material that has a lower frictional loss. Then the efficiency of the system can be further improved.

2. Improving the base of the system in a way that reduces the swaying. From this the probability of components getting broken can be reduced and the efficiency can be improved.
3. Considering the possibility of including a tuning system to tune the system according to the best input. So, the system will focus on the optimum frequency range when there are inputs with varying frequencies and it will increase the harnessed energy output. This should be done in a way that the system stays being a low-cost implementation and this requires greater insight regarding the dynamics of the system. This will enhance the practical implementation aspect of this system.
4. Conducting experiments to detect the effect of magnetic moment on the power generation. This requires specific instruments and setups and it would be better if this effect can be measured physically.
5. Conducting a comparison of this prototype with already available electromagnetic, piezo electric, electro static energy harvesters to assess the efficiency with respect to those prototypes.

REFERENCES

- Challa, V. R., Prasad, M. G., Shi, Y., & Fisher, F. T. (2008). A vibration energy harvesting device with bidirectional resonance frequency tunability. *Smart Materials and Structures*, *17*(1). <https://doi.org/10.1088/0964-1726/17/01/015035>
- Cho, J. Y., Jeong, S., Jabbar, H., Song, Y., Ahn, J. H., Kim, J. H., Jung, H. J., Yoo, H. H., & Sung, T. H. (2016). Piezoelectric energy harvesting system with magnetic pendulum movement for self-powered safety sensor of trains. *Sensors and Actuators, A: Physical*, *250*, 210–218. <https://doi.org/10.1016/j.sna.2016.09.034>
- Cleante, V. G., Brennan, M. J., Gatti, G., & Thompson, D. J. (2019). On the target frequency for harvesting energy from track vibrations due to passing trains. *Mechanical Systems and Signal Processing*, *114*, 212–223. <https://doi.org/10.1016/j.ymssp.2018.05.003>
- Dong, L., Closson, A. B., Jin, C., Trase, I., Chen, Z., & Zhang, J. X. J. (2019). Vibration-Energy-Harvesting System: Transduction Mechanisms, Frequency Tuning Techniques, and Biomechanical Applications. In *Advanced Materials Technologies* (Vol. 4, Issue 10). Wiley-Blackwell. <https://doi.org/10.1002/admt.201900177>
- Eichhorn, C., Goldschmidtboeing, F., & Woias, P. (2009). Bidirectional frequency tuning of a piezoelectric energy converter based on a cantilever beam. *Journal of Micromechanics and Microengineering*, *19*(9). <https://doi.org/10.1088/0960-1317/19/9/094006>
- Fan, F. R., Tian, Z. Q., & Lin Wang, Z. (2012). Flexible triboelectric generator. *Nano Energy*, *1*(2), 328–334. <https://doi.org/10.1016/j.nanoen.2012.01.004>
- Fan, K., Liu, S., Liu, H., Zhu, Y., Wang, W., & Zhang, D. (2018). Scavenging energy from ultra-low frequency mechanical excitations through a bi-directional hybrid energy harvester. *Applied Energy*, *216*, 8–20. <https://doi.org/10.1016/j.apenergy.2018.02.086>

- Gholikhani, M., Beheshti Shirazi, S. Y., Mabrouk, G. M., & Dessouky, S. (2021). Dual electromagnetic energy harvesting technology for sustainable transportation systems. *Energy Conversion and Management*, 230. <https://doi.org/10.1016/j.enconman.2020.113804>
- Haroun, A., Yamada, I., & Warisawa, S. (2015a). Micro electromagnetic vibration energy harvester based on free/impact motion for low frequency-large amplitude operation. *Sensors and Actuators, A: Physical*, 224, 87–98. <https://doi.org/10.1016/j.sna.2015.01.025>
- Haroun, A., Yamada, I., & Warisawa, S. (2015b). Study of electromagnetic vibration energy harvesting with free/impact motion for low frequency operation. *Journal of Sound and Vibration*, 349, 389–402. <https://doi.org/10.1016/j.jsv.2015.03.048>
- He, X., Teh, K. S., Li, S., Dong, L., & Jiang, S. (2017). Modeling and experimental verification of an impact-based piezoelectric vibration energy harvester with a rolling proof mass. *Sensors and Actuators, A: Physical*, 259, 171–179. <https://doi.org/10.1016/j.sna.2017.03.034>
- Hendijanizadeh, M., Sharkh, S. M., Elliott, S. J., & Moshrefi-Torbati, M. (2013). Output power and efficiency of electromagnetic energy harvesting systems with constrained range of motion. *Smart Materials and Structures*, 22(12). <https://doi.org/10.1088/0964-1726/22/12/125009>
- Hou, W., Zheng, Y., Guo, W., & Pengcheng, G. (2021). Piezoelectric vibration energy harvesting for rail transit bridge with steel-spring floating slab track system. *Journal of Cleaner Production*, 291. <https://doi.org/10.1016/j.jclepro.2020.125283>
- Iqbal, M., & Khan, F. U. (2018). Hybrid vibration and wind energy harvesting using combined piezoelectric and electromagnetic conversion for bridge health monitoring applications. *Energy Conversion and Management*, 172, 611–618. <https://doi.org/10.1016/j.enconman.2018.07.044>
- Lin, T., Pan, Y., Chen, S., & Zuo, L. (2018). Modeling and field testing of an electromagnetic energy harvester for rail tracks with anchorless mounting.

- Applied Energy*, 213, 219–226.
<https://doi.org/10.1016/j.apenergy.2018.01.032>
- Lin, T., Wang, J. J., & Zuo, L. (2018). Efficient electromagnetic energy harvester for railroad transportation. *Mechatronics*, 53, 277–286.
<https://doi.org/10.1016/j.mechatronics.2018.06.019>
- Ooi, B. L., & Gilbert, J. M. (2014). Design of wideband vibration-based electromagnetic generator by means of dual-resonator. *Sensors and Actuators, A: Physical*, 213, 9–18. <https://doi.org/10.1016/j.sna.2014.03.037>
- Saravia, C. M., Ramírez, J. M., & Gatti, C. D. (2017). A hybrid numerical-analytical approach for modeling levitation based vibration energy harvesters. *Sensors and Actuators, A: Physical*, 257, 20–29.
<https://doi.org/10.1016/j.sna.2017.01.023>
- Shahosseini, I., & Najafi, K. (2014). Mechanical amplifier for translational kinetic energy harvesters. *Journal of Physics: Conference Series*, 557(1).
<https://doi.org/10.1088/1742-6596/557/1/012135>
- Shahruz, S. M. (2006). Design of mechanical band-pass filters with large frequency bands for energy scavenging. *Mechatronics*, 16(9), 523–531.
<https://doi.org/10.1016/j.mechatronics.2006.04.003>
- Shen, Y., & Lu, K. (2020). Scavenging power from ultra-low frequency and large amplitude vibration source through a new non-resonant electromagnetic energy harvester. *Energy Conversion and Management*, 222.
<https://doi.org/10.1016/j.enconman.2020.113233>
- Wang, H., He, C., Lv, S., & Sun, H. (2018). A new electromagnetic vibrational energy harvesting device for swaying cables. *Applied Energy*, 228, 2448–2461. <https://doi.org/10.1016/j.apenergy.2018.07.059>
- Wang, X., Liang, X., & Wei, H. (2015). A study of electromagnetic vibration energy harvesters with different interface circuits. *Mechanical Systems and Signal Processing*, 58, 376–398. <https://doi.org/10.1016/j.ymsp.2014.10.004>
- Wang, Z., Wang, W., Gu, F., Wang, C., Zhang, Q., Feng, G., & Ball, A. D. (2021). On-rotor electromagnetic energy harvester for powering a wireless condition

- monitoring system on bogie frames. *Energy Conversion and Management*, 243. <https://doi.org/10.1016/j.enconman.2021.114413>
- Wei, C., & Jing, X. (2017). A comprehensive review on vibration energy harvesting: Modelling and realization. In *Renewable and Sustainable Energy Reviews* (Vol. 74, pp. 1–18). Elsevier Ltd. <https://doi.org/10.1016/j.rser.2017.01.073>
- Yildirim, T., Ghayesh, M. H., Li, W., & Alici, G. (2017). A review on performance enhancement techniques for ambient vibration energy harvesters. In *Renewable and Sustainable Energy Reviews* (Vol. 71, pp. 435–449). Elsevier Ltd. <https://doi.org/10.1016/j.rser.2016.12.073>
- Zhu, D., Beeby, S., Tudor, J., & Harris, N. (2013). Increasing output power of electromagnetic vibration energy harvesters using improved Halbach arrays. *Sensors and Actuators, A: Physical*, 203, 11–19. <https://doi.org/10.1016/j.sna.2013.08.008>
- Zou, H. X., Zhao, L. C., Gao, Q. H., Zuo, L., Liu, F. R., Tan, T., Wei, K. X., & Zhang, W. M. (2019). Mechanical modulations for enhancing energy harvesting: Principles, methods and applications. In *Applied Energy* (Vol. 255). Elsevier Ltd. <https://doi.org/10.1016/j.apenergy.2019.113871>

APPENDIX: INPUT GAIN OF SIMULATION

	Frequency (Hz)																									
Amplitude (m)	0.1	0.2	0.4	0.6	0.8	1	1.2	1.4	1.6	1.8	2	2.2	2.4	2.6	2.8	3	3.2	3.4	3.6	3.8	4	4.2	4.4	4.6	4.8	5
0.001	5.36	3.71	5.35	5.36	3.74	3.48	3.68	5.34	5.37	3.78	5.90	3.65	5.35	5.40	3.81	1.32	3.62	5.32	5.37	3.85	1.81	3.62	5.38	5.33	3.96	4.77
0.002	5.36	3.71	5.35	5.36	3.74	3.48	3.68	5.34	5.37	3.78	5.90	3.65	5.35	5.40	3.81	1.32	3.62	5.32	5.37	3.85	1.81	3.62	5.38	5.33	3.96	5.96
0.004	5.36	3.71	5.35	5.36	3.74	3.48	3.68	5.34	5.37	3.78	5.90	3.65	5.35	5.40	3.81	1.32	3.62	5.32	5.37	3.85	1.81	3.62	5.38	5.33	3.96	5.96
0.006	5.36	3.71	5.35	5.36	3.74	4.28	3.68	5.34	5.37	3.78	5.28	3.65	5.35	5.40	3.81	4.43	3.62	5.32	5.37	3.85	2.26	3.62	5.38	5.33	3.96	4.80
0.008	5.36	3.71	5.35	5.36	3.74	3.48	3.68	5.34	5.37	3.78	5.90	3.65	5.35	5.40	3.81	1.32	3.62	5.32	5.37	3.85	1.81	3.62	5.38	5.33	3.96	5.11
0.01	5.36	3.71	5.35	5.36	3.74	1.05	3.68	5.34	5.37	3.78	5.44	3.65	5.35	5.40	3.81	4.05	3.62	5.32	5.37	3.85	2.20	3.62	5.38	5.33	3.96	5.35
0.012	5.36	3.71	5.35	5.36	3.74	4.28	3.68	5.34	5.37	3.78	5.28	3.65	5.35	5.40	3.81	4.43	3.62	5.32	5.37	3.85	2.26	3.62	5.38	5.33	3.96	4.80
0.014	5.36	3.71	5.35	5.36	3.74	4.17	3.68	5.34	5.37	3.78	1.20	3.65	5.35	5.40	3.81	2.79	3.62	5.32	5.37	3.85	2.27	3.62	5.38	5.33	3.96	5.97
0.016	5.36	3.71	5.35	5.36	3.74	3.48	3.68	5.34	5.37	3.78	5.90	3.65	5.35	5.40	3.81	1.32	3.62	5.32	5.37	3.85	1.81	3.62	5.38	5.33	3.96	5.96
0.018	5.36	3.71	5.35	5.36	3.74	0.11	3.68	5.34	5.37	3.78	2.55	3.65	5.35	5.40	3.81	1.14	3.62	5.32	5.37	3.85	1.94	3.62	5.38	5.33	3.96	6.02
0.02	5.36	3.71	5.35	5.36	3.74	1.05	3.68	5.34	5.37	3.78	5.44	3.65	5.35	5.40	3.81	4.05	3.62	5.32	5.37	3.85	2.20	3.62	5.38	5.33	3.96	5.35
0.022	5.36	3.71	5.35	5.36	3.74	0.73	3.68	5.34	5.37	3.78	3.30	3.65	5.35	5.40	3.81	4.11	3.62	5.32	5.37	3.85	1.82	3.62	5.38	5.33	3.96	4.59
0.024	5.36	3.71	5.35	5.36	3.74	4.28	3.68	5.34	5.37	3.78	5.28	3.65	5.35	5.40	3.81	4.43	3.62	5.32	5.37	3.85	2.26	3.62	5.38	5.33	3.96	4.80
0.026	5.36	3.71	5.35	5.36	3.74	0.69	3.68	5.34	5.37	3.78	1.29	3.65	5.35	5.40	3.81	0.85	3.62	5.32	5.37	3.85	1.71	3.62	5.38	5.33	3.96	4.76
0.028	5.36	3.71	5.35	5.36	3.74	4.17	3.68	5.34	5.37	3.78	1.20	3.65	5.35	5.40	3.81	2.79	3.62	5.32	5.37	3.85	2.27	3.62	5.38	5.33	3.96	5.97
0.03	5.36	3.71	5.35	5.36	3.74	0.92	3.68	5.34	5.37	3.78	3.50	3.65	5.35	5.40	3.81	5.40	3.62	3.65	5.37	3.85	1.63	3.62	5.38	5.33	3.96	5.03
0.032	5.36	3.71	5.35	5.36	3.74	3.48	3.68	5.34	5.37	3.78	5.90	3.65	5.35	5.40	3.81	1.32	3.62	5.32	5.37	3.85	1.81	3.62	5.38	5.33	3.96	5.96
0.034	5.36	3.71	5.35	5.36	3.74	2.52	3.68	5.34	5.37	3.78	0.91	3.65	5.35	5.40	3.81	1.50	3.62	5.32	5.37	3.85	2.00	3.62	5.38	5.33	3.96	5.78
0.036	5.36	3.71	5.35	5.36	3.74	0.11	3.68	5.34	5.37	3.78	2.55	3.65	5.35	5.40	3.81	1.14	3.62	5.32	5.37	3.85	1.94	3.62	5.38	5.33	3.96	6.02
0.038	5.36	3.71	5.35	5.36	3.74	1.47	3.68	5.34	5.37	3.78	1.72	3.65	5.35	5.40	3.81	0.89	3.62	5.32	5.37	3.85	1.55	3.62	5.38	5.33	3.96	5.72
0.04	5.36	3.71	5.35	5.36	3.74	1.05	3.68	5.34	5.37	3.78	5.44	3.65	5.35	5.40	3.81	4.05	3.62	5.32	5.37	3.85	2.20	3.62	5.38	5.33	3.96	5.35
Average	5.36	3.71	5.35	5.36	3.74	2.47	3.68	5.34	5.37	3.78	4.09	3.65	5.35	5.40	3.81	2.57	3.62	5.24	5.37	3.85	1.97	3.62	5.38	5.33	3.96	5.43